Charm and the Virtual Photon at HERA and a Global Tracking Trigger for ZEUS

Benjamin John West

University College London

August 2001

Thesis submitted in fulfillment of the requirements for
the degree of Doctor of Philosophy in Physics

Abstract

Previous measurements at ZEUS have demonstrated suppression of photon structure like effects due to both the virtuality of the photon, Q^2, and the presence of charm. In this thesis aspects of these two measurements have been combined in order to determine whether these two suppressions are independent.

The measurement was made with the ZEUS detector at HERA in the kinematic region $0 \lesssim Q^2 < 5 \cdot 10^3$ GeV^2 using dijet events containing a D^* meson. Events having two or more jets with large transverse energies were selected using the longitudinally invariant k_T algorithm in the laboratory frame. The dijet cross section was measured as a function of the fractional momentum of the photon participating in the dijet production, x_γ^{obs} , and of Q^2.

The ratio of low to high x_γ^{obs} cross sections was found not to change significantly with Q^2. This is in marked contrast to previous measurements which did not require a D^*, demonstrating for the first time that the observed suppressions of the low x_γ^{obs} cross section due to non-zero photon virtuality and due to charm are not independent. The ratio was also compared to the predictions of leading-order pQCD. Calculations which included either a resolved virtual photon in the DGLAP evolution scheme or used CCFM evolution gave a better description of the data than a DGLAP calculation with no photon structure.

During the 2000 – 2001 shutdown both the HERA accelerator and ZEUS detector were upgraded. In order to take advantage of these improvements a new “global tracking trigger”, combining information from the Central Tracking Detector and the newly installed MicroVertex Detector at the Second Level Trigger, has been developed. The algorithm is described and its performance evaluated. The event z vertex resolution is two orders of magnitude better than that for the present algorithm. This will enable future measurements of the cross section ratio to be made with much greater precision.

To my family and friends

"Writing a book is an undertaking far more horrific than I'd ever imagined. Not only must the writer come up with several tens of thousands of words, not all of them the same, but he or she must arrange them in an order that makes some sort of sense to the first time reader. It's no use starting your book 'Linford Christie stepped into the horse-box bemused by the wall of mushrooms which stood grinning at the back' if you have no intention of taking these ideas any further. To start a book with this sentence, but then take your eye off the ball for a moment and end up writing a twenty-thousand word guide to Polish war memorials, deserves the highest criticism. It's a fault that took me many months of practice to avoid.

Others have been less meticulous. I'm surely not the only one to have noticed that Will Hutton's otherwise admirably written economics bestseller *The State We're In* opens with the sentence 'This book has been carefully graded so that you can begin with one or two elementary dishes yet soon be able to set out a full Thai meal with all its unique flavours.' Nor is there any earthly explanation other than sheer authorial incompetence for a few stray lines in Stephen Hawking's *A Brief History of Time* which, at the end of a brilliant explanation of the symbiotic relationship between quantum theory and relativity, seductively hinting at a unified theory of gravity, suddenly continue:

> Bevin let out a gasp of astonishment and playful pleasure at the Professor's remarks. 'Ooh boy,' she yelped, like a cat. 'Tell it to me one more time, 'cos I'm on fire, particle man!' She remembered now their curiously interrupted lovemaking from the previous night and resolved to hammer the door shut this time.

The remaining ninety pages revert to a discussion of particle/wave duality within light emissions.

Consistency is therefore a prerequisite for even the most vaguely competent stab at a book."

Armando Iannucci, *Facts and Fancies*, 1997

Acknowledgments

Over the last three years I have been fortunate enough to work with many excellent people, without whom this thesis would not have been possible. For help with my analysis, I would like to thank Jon Butterworth for his advice and motivation throughout; Mark Hayes for teaching me the basics; Leonid Gladilin for his knowledge of all things heavy flavoured; Jo Cole for her advice on D^*s in DIS; Alex Tapper for his extensive knowledge of DIS and generosity in sharing it; Matt Lightwood for his hard work reproducing my analysis; and Richard Hall-Wilton for continuing where I left off. For all his hard work on the GTT, both before and after I joined the effort, I owe a great deal to Mark Sutton. The product of our collaboration is something I think we can both be proud of. I would also like to thank Stew Boogert for many random physics conversations which helped both my understanding and enthusiasm.

Fortunately, there has been much more to my life than just work during my PhD, and for that I owe many people thanks. In particular I would like to thank Alex Ferguson for being a good friend and housemate; Ann Whittle for the time we had together; Kate Evans for listening and being a good friend; Beth Purse for staying close even when far away; Stew Boogert for being a good cook, host and mate; Alex Tapper for many enjoyable hours in bars; Rod Walker for his citrus theory of life; Elaine McLeod for enjoyable conversations, both home and abroad; Ricardo Gonçalo for being a great neighbour and friend; Claire Gwenlan for the many chats; and Jon Butterworth for being more than just a supervisor.

Finally, I would like to thank my parents for their unconditional support and encouragement throughout my life.

Contents

List of Figures

List of Tables

Part I

Charm and the virtual photon at HERA

Chapter 1

HERA and the ZEUS detector

1.1 The HERA accelerator

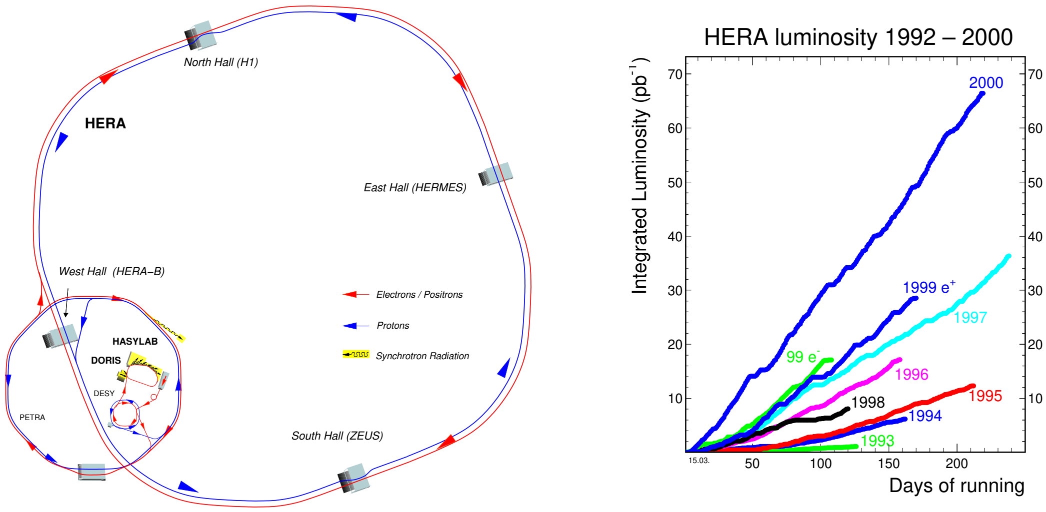

Figure 1.1: *The HERA accelerator chain (left) and delivered luminosity from 1992-2000 (right).*

The HERA (Hadron Elektron Ring Anlage) accelerator is the world's first, and only, $e^{\pm}p$ collider. HERA is located in Hamburg, Germany, and has been providing luminosity to the colliding beam experiments H1 and ZEUS since 1992. The HERA ring, together with the injection chain, is shown in Figure 1.1. The leptons and protons are accelerated in two separate machines which use conventional and superconducting magnets respectively.

In the proton injection system, H^- ions are accelerated to 50MeV using a linear accelerator. The electrons are then stripped off, to yield protons which are passed to the DESY III proton synchrotron where they are accelerated to 7.5 GeV in 11 bunches with the same 96 ns bunch spacing as the HERA ring. From here they are passed to the PETRA accelerator, where they are accelerated to 40 GeV and injected into the HERA proton machine. This process continues until HERA is filled with 210 bunches, which are then accelerated to the HERA operation proton energy[1] using conventional radio frequency cavities. The proton beam is focused and guided by superconducting quadrupole and dipole magnets.

Lepton injection commences with LINACS's I and II which accelerate lepton beams to 220 and 450 MeV respectively. These are then transferred to the DESY II synchrotron and accelerated to 7.5 GeV before being injected into the PETRA II storage ring in bunches with 96 ns spacing. The beam is then accelerated to 14 GeV and injected into the HERA lepton machine. After it is filled with 210 bunches the beam is accelerated to the operating energy of 27.52 GeV, using both conventional and superconducting cavities.

1.2 The ZEUS detector

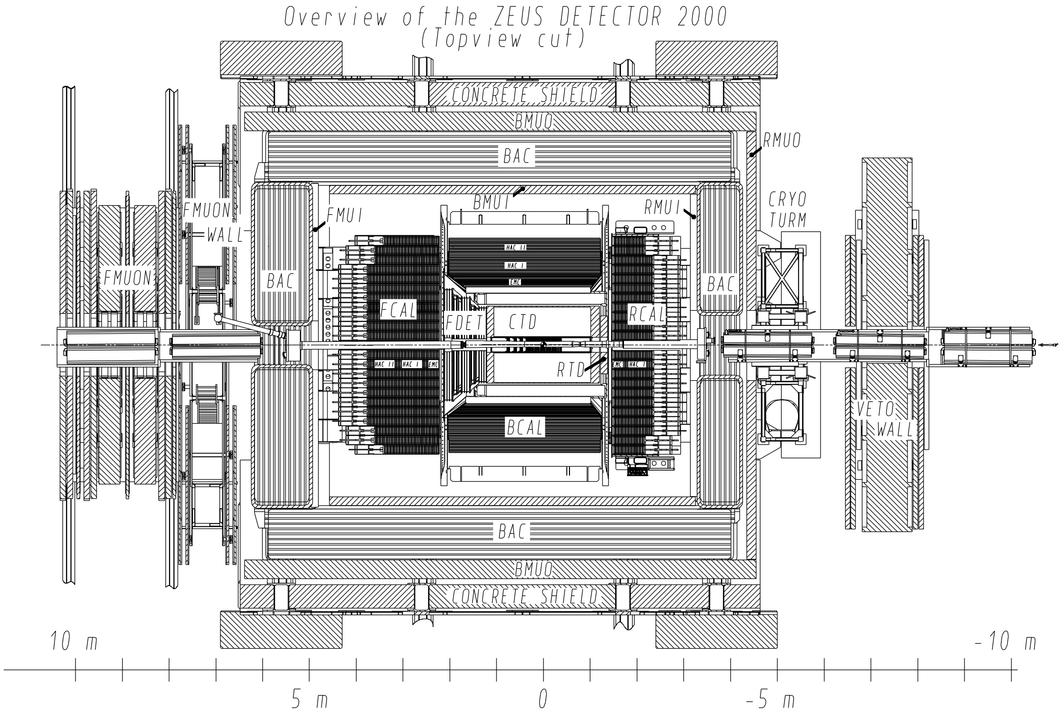

Figure 1.2: *Overview of the ZEUS detector.*

The ZEUS detector, shown in Figure 1.2, is a general purpose magnetic detector, with nearly hermetic calorimetric coverage. A detailed description of the ZEUS detector can be found elsewhere [1]. A brief outline of the components which are most relevant for this analysis is given below.

[1]820 GeV from 1992-1997 and 920 GeV from 1998-2000.

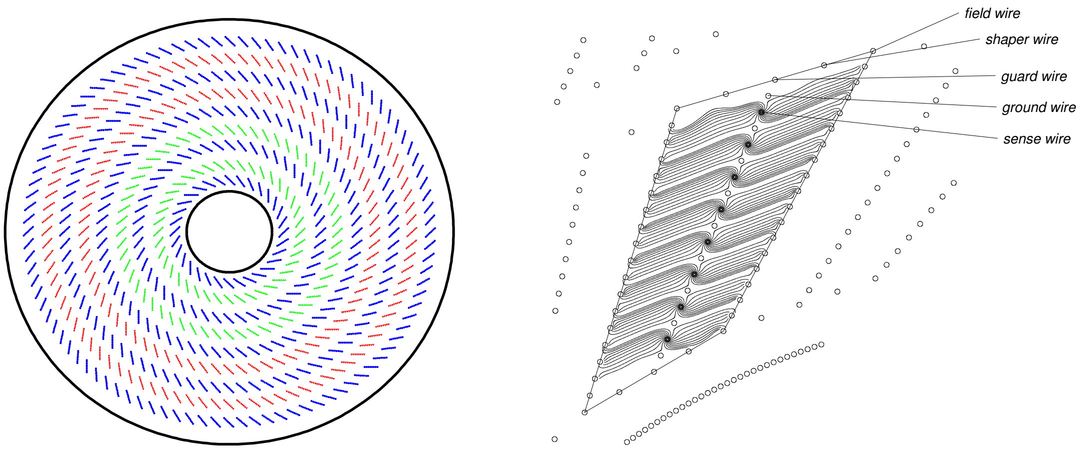

Figure 1.3: *x-y view of the CTD showing the wire layout (left) and a CTD drift cell (right).*

1.3 The Central Tracking Detector (CTD)

The CTD [2] is a cylindrical drift chamber, which operates in a magnetic field of 1.43T, provided by a thin superconducting coil. The CTD consists 72 cylindrical drift chamber layers, organised in 9 superlayers, covering the polar angle range 15°-164°. A superlayer contains between 32 and 96 drift cells, each comprising eight sense wires oriented in a plane at 45° to the radial line from the chamber axis. The drift field is at a Lorentz angle of 45° to the radial axis so that the drift electrons follow radially transverse paths which is important in left-right ambiguity breaking.

Wires in the odd numbered "axial" superlayers run parallel to the z axis[2], whereas wires in the even numbered "stereo" superlayers are at a small stereo angle ($\sim \pm 5°$), allowing both r-ϕ and z coordinates to be accurately measured. The nominal resolution for full length tracks in the CTD is 180 μm in $r - \phi$ and $\approx$ 2 mm in z. The first three axial layers are also instrumented with a z-by-timing system which estimates the position of a hit along a wire from the pulse arrival times at each end of the chamber. The resolution using this method is $\sim$4 cm and it is predominantly used for trigger purposes.

The transverse momentum resolution for full length tracks is $\sigma(p_T)/p_T = 0.0058p_T \oplus 0.0065 \oplus 0.0014/p_T$, with p_T in GeV [3].

[2]The ZEUS coordinate system is a right-handed Cartesian system, with the z axis pointing in the proton beam direction, referred to as "forward direction", and the x axis pointing left towards the centre of HERA. The coordinate origin is at the nominal interaction point.

1.4 ZEUS calorimetry

The high-resolution uranium–scintillator calorimeter (CAL) [4] consists of three parts: the forward (FCAL), the barrel (BCAL) and the rear (RCAL) calorimeters. Each part is subdivided transversely into towers and longitudinally into one electromagnetic section (EMC) and either one (in RCAL) or two (in BCAL and FCAL) hadronic sections (HAC). The smallest subdivision of the calorimeter is called a cell. Each HAC cell is approximately 20×20 cm and each EMC cell is approximately 5×20 cm (in BCAL and FCAL) or 10×20 cm (in RCAL). The readout is performed by two photomultipliers (coupled to the scintillator by wavelength shifters) per cell; the pair ensuring the measurement to be independent of the impact point of the particles. A typical FCAL module with EMC and HAC divisions can be seen in Figure 1.4.

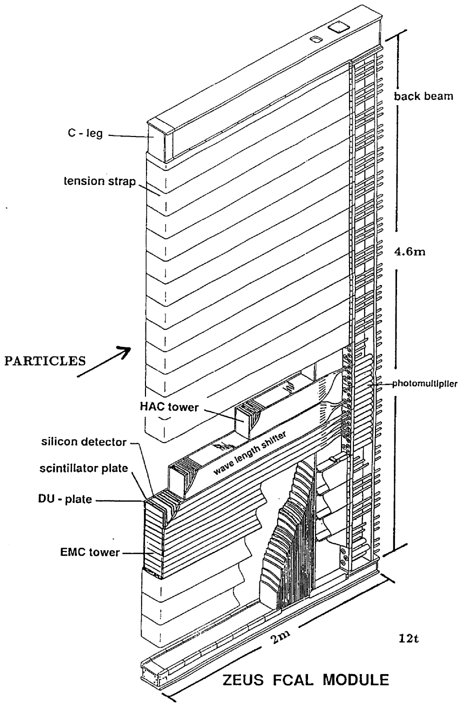

Figure 1.4: *Cut-away view of an FCAL module.*

The EMC is the inner section of the tower, with two hadronic sections (HAC1 and HAC2) outside this. The alternating layers of Depleted Uranium and scintillator can also be seen. The unequal response, due to hadronic showers producing fewer photons than electromagnetic showers for a particle of the same energy, is compensated by the uranium, which absorbs neutrons from the hadronic shower and emits photons which can then be detected by the photomultipliers. By choosing a suitable thickness of uranium, the same number of photons are produced for hadronic and electromagnetic showers of the same energy. This is important in the reconstruction of jets which are composed of both electromagnetic and hadronic components in an unknown proportion. The CAL energy resolutions, as measured under test beam conditions, are $\sigma(E)/E = 0.18\sqrt{E}$ for electrons and $\sigma(E)/E = 0.35\sqrt{E}$ for hadrons (E in GeV).

Associated with the CAL are several subcomponents, designed to improve the energy resolution or particle identification properties of the calorimeter, two of which are relevant to this analysis.

Presampler

The Presampler [5] is a thin segmented layer of scintillator on the inner face of the calorimeter. This can be used to estimate the amount of showering, and hence energy loss, that a particle has undergone while passing through the dead material before the CAL.

SRTD

The Small-angle Rear Tracking Detector (SRTD) [6], is designed to measure electrons scattered at small angles and improve the measurement of their position and energy. The SRTD is located on the face of the RCAL, around the beam pipe, covering the polar angle region $162° - 176°$. This region is particularly important because it is the region in which most DIS electrons are scattered. The SRTD consists of two layers of finely segmented silicon strips, resulting in a tracking resolution of about 3mm, compared to 1cm in the calorimeter. The SRTD also provides a measurement of the amount of showering before the CAL which can be used to correct the energy obtained from the calorimeter.

1.5 The luminosity monitor

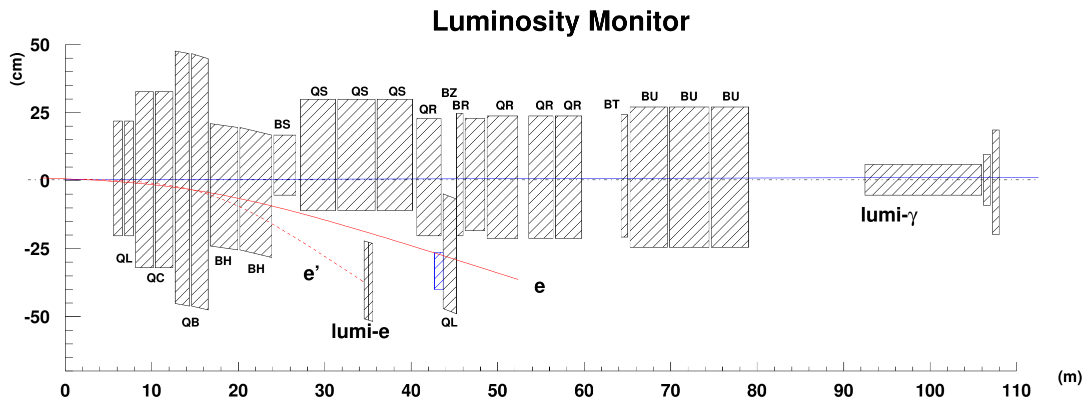

Figure 1.5: *The Luminosity Monitor.*

The luminosity is measured using the rate of Bethe-Heitler photons, $ep \to ep\gamma$, where the γ is emitted by the electron at a very low angle to the incident electron direction in negative z. The cross section for this process is very high and can be calculated to within 0.5%. The measurement of the small angle electron and

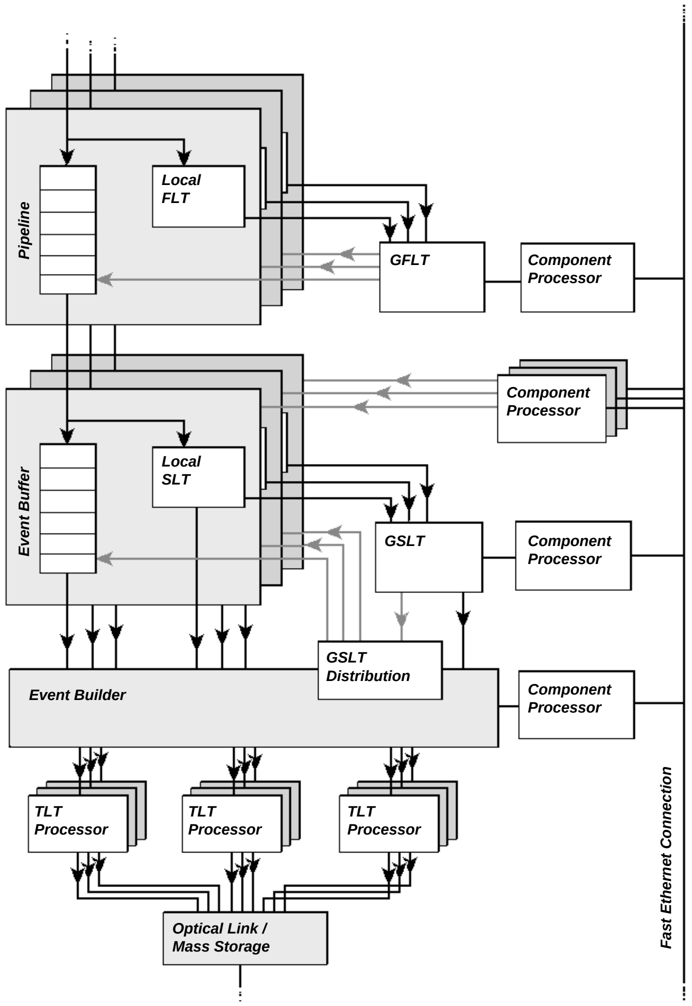

Figure 1.6: *The ZEUS data acquisition and trigger system.*

photon is performed by two separate detectors. The photon detector is situated close to the beampipe between 104 and 107 m from the interaction point, in the electron direction. The electron detector is situated 34 m from the interaction point. Both detectors are based on lead–scintillator sandwich calorimeters with an energy resolution of $\sigma(E)/E = 0.18\sqrt{E}$.

1.6 The ZEUS trigger system

The nominal bunch crossing rate of the HERA accelerator is $\sim$ 10 MHz which poses challenges for the Data AcQuisition (DAQ) and trigger systems. The interaction rate is dominated by interactions between the proton beam and residual gas, "beam gas", which contributes about 10-100kHz, whilst the rate written to tape for *ep* interactions is between a few and 10 Hz.

To reduce the rate to less than ~ 10 Hz whilst efficiently selecting ep events, ZEUS uses a three stage trigger system [7] shown in Figure 1.6.

The rate is initially reduced to ~ 1 kHz by the First Level Trigger (FLT) which is a hardware based trigger. Each component used at the FLT has its own FLT and stores the data in a pipeline awaiting a decision. The decision is made within $\sim 2\ \mu$s of the bunch crossing and passed onto the Global First Level Trigger (GFLT) which then makes a final decision in 4.4 μs, passing the decision back to the component readout.

Events which pass the FLT proceed onto the Second Level Trigger (SLT). The SLT is a software based trigger run on a network of transputers, designed to reduce the rate by approximately a factor of ten. Analogously to the FLT, each component can have its own SLT, which passes decisions onto the Global Second Level Trigger (GSLT).

Each component then passes the filtered events to an event builder which fills the data structure for the Third Level Trigger (TLT). The TLT runs a crude version of the full reconstruction software and is able to make decisions concerning global event properties, jet properties and event kinematics. The event rate is now reduced to a manageable ~ 1 Hz. The final stage is to transfer the events by an optical fibre link to storage for processing by the full ZEUS reconstruction software at a later date.

Chapter 2

QCD and *ep* Interactions

The interactions of quarks and gluons are described by Quantum Chromodynamics (QCD), a non-abelian gauge theory based on the SU(3) colour symmetry group. The quarks, each in three colours, interact by the exchange of electrically neutral vector bosons, gluons, which form a colour octet. The gluons are not colour neutral and thus they themselves interact strongly. A consequence of this property is asymptotic freedom, which states that the interaction strength of two coloured objects *decreases* the *shorter* the distance between them. The effective strong coupling constant α_s then depends on the scale at which the QCD process occurs. The leading-order solution of the renormalisation group equation gives

$$\alpha_s(Q^2) = \frac{4\pi}{\beta_0 \ln(Q^2/\Lambda^2)}, \tag{2.1}$$

where Q^2 denotes the scale at which α_s is probed and Λ is a QCD cutoff parameter. The parameter β_0 is related to the number of quark flavors in the theory, N_f, by

$$\beta_0 = 11 - \frac{2}{3}N_f. \tag{2.2}$$

Since the known number of flavors is six, $\beta_0 > 0$, the coupling constant becomes smaller the larger the scale Q^2. The property of asymptotic freedom has been proven rigorously and allows predictions for the properties of strong interactions to be made in the perturbative QCD (pQCD) regime, in which α_s is small. One such example is the production of jets[1] in e^+e^- annihilation at LEP in which $Q^2 \sim M_Z^2$. At lower scales α_s becomes large making perturbative calculations unreliable and accurate

[1]The produced quarks and gluons cannot be observed directly due to the phenomena known as "colour confinement". Instead a spray of hadrons, called a jet, emerges in the approximate direction of each parton.

predictions cannot be made. For example, the distribution of the "partons" bound in hadrons, cannot be calculated from first principles.

QCD has been tested in depth in the perturbative regime and describes the data very well [8]. However, because the observables are based on hadrons rather than the partons to which perturbative calculations apply the precision achieved in testing QCD is lower than in the case of electroweak interactions and a detailed experimental knowledge of the structure of hadrons is essential.

2.1 Proton structure

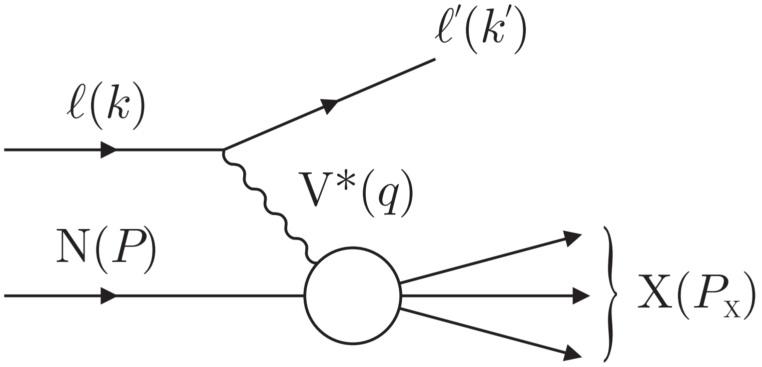

Figure 2.1: *Kinematics of a deep inelastic scattering event.*

The structure of the proton is studied in deep inelastic lepton-hadron scattering (DIS), shown in Figure 2.1. Two distinct classes of scattering exist, neutral current (NC), where the exchanged boson is a γ^* or a Z^0, and charged current (CC), where the exchanged boson is a $W^\pm$. If the incoming and outgoing lepton four-momenta are labeled by k^μ and k'^μ, the momentum of the target hadron by p^μ and the four-momentum transfer by $q^\mu = k^\mu - k'^\mu$, then the standard DIS variables are defined as follows:

$$Q^2 = -q^2, \tag{2.3}$$

$$M^2 = p^2, \tag{2.4}$$

$$\nu = P \cdot q = M(E' - E), \tag{2.5}$$

$$x = \frac{Q^2}{2\nu} = \frac{Q^2}{2M(E' - E)}, \tag{2.6}$$

$$y = \frac{q \cdot P}{k \cdot P} = 1 - E'/E, \tag{2.7}$$

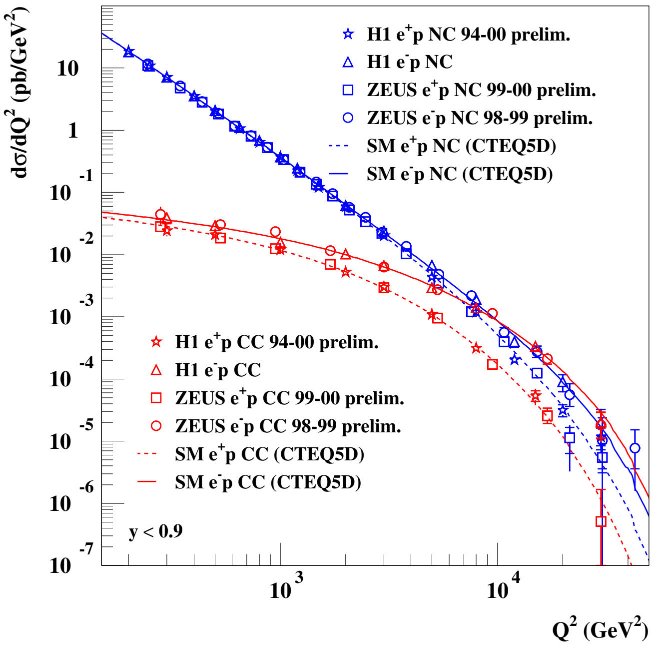

Figure 2.2: *The NC and CC cross sections as a function of Q^2 measured at HERA.*

where the energy variables refer to the hadron rest frame, M is the proton mass, Q^2 is the invariant mass of the exchanged boson, x is the Bjorken scaling variable, and y is the fractional energy transfer in the hadron rest frame. The invariant mass of the total system is given by:

$$s = (P+k)^2 \approx 2P\cdot k = \frac{Q^2}{xy} \tag{2.8}$$

so that at fixed s only two of the three invariants x, y and Q^2 are actually independent.

The NC and CC cross sections, shown in Figure 2.2, can be described in terms of “structure functions”, F_i, which parameterise the structure of the proton target as seen by the virtual boson. For $e^{\pm}p$ NC scattering the double-differential cross section is

$$\frac{d^2\sigma^{ep}}{dxdQ^2} = \frac{4\pi\alpha^2}{xQ^4}\Big[\frac{y^2}{2}2xF_1 + (1-y)F_2 \mp (y-\frac{y^2}{2})xF_3\Big]. \tag{2.9}$$

Using the relation $F_L = F_2 - 2xF_1$ this reduces to

$$\frac{d^2\sigma^{ep}}{dxdQ^2} = \frac{4\pi\alpha^2}{xQ^4}\Big[Y_+F_2 - y^2F_L \mp Y_- xF_3\Big] \tag{2.10}$$

where the helicity dependence of the electroweak interactions is contained within

$$Y_{\pm} = (1 \pm (1-y)^2) \tag{2.11}$$

F_2 is the generalised structure function of γ and Z^0 exchange, F_L is the longitudinal structure function, and F_3 is the parity violating term arising from Z^0 exchange. Since F_3 is small for $Q^2 << M_Z^2$ it is neglected in all further discussions here. A detailed derivation of all these terms is given, for example, in [9].

2.1.1 The naive quark parton model

The form of the cross sections given above is completely general, all the physics detail is contained in the structure functions. *A priori* these might be expected to be complicated functions of ν and Q^2, reflecting the complexity of the inelastic scattering process. However, in 1969, Bjorken predicted that in the deep inelastic region[2] the structure functions should "scale", i.e. become functions not of Q^2 and ν independently but only of their ratio Q^2/ν. This predicted scaling was confirmed by results from SLAC [10].

Feynman gave an intuitive explanation of Bjorken's arguments in his parton model [11], in which the proton is assumed to be composed of point-like objects, called partons. The *inelastic* scattering of the lepton off the proton is then described as the *elastic* scattering of the lepton off a parton *within* the proton. The ep cross section is then given by the incoherent sum of the electron-parton scattering processes.

If a parton of mass m, carrying a fraction, ξ, of the total proton momentum is struck, conservation of four-momentum implies [3]

$$
\begin{aligned}
0 \approx m^2 = (\xi p + q)^2 = \xi^2 p^2 - Q^2 + 2\xi p \cdot q \\
\Rightarrow \xi = \frac{Q^2}{2p \cdot q} = x.
\end{aligned}
$$

The Bjorken scaling variable, x, then has a simple interpretation as the fraction of the longitudinal proton momentum, ξ, carried by the parton in the hard scatter.

Within the parton model the structure functions are given by

$$
\begin{aligned}
F_2(x) &= \sum_i e_i^2 x f_i(x) &\quad (2.12)\\
F_1(x) &= \frac{1}{2}\sum_i e_i^2 f_i(x) &\quad (2.13)
\end{aligned}
$$

[2] Q^2, $\nu \to \infty$ but Q^2/ν finite.

[3] This is in the infinite momentum frame of the proton, where the partons have no transverse momentum and the masses can be neglected.

where e_i are the parton charges and $f_i(x)$ are the parton density functions which can be interpreted as the probability of finding a parton i with momentum fraction x in the proton. F_2 and F_1 are connected by the Callan-Gross relation

$$2xF_1(x) = F_2(x) \tag{2.14}$$

which is a direct consequence of the assumption that partons are massless, spin-1/2, non-interacting particles and implies that F_L is zero.

Through measurements at SLAC and in νN scattering [12], these partons were associated with the quarks of the Gell-Mann and Zweig and the model became the quark parton model (QPM).

2.1.2 The QCD improved quark parton model

If the proton consisted solely of charged quarks the sum of their momenta would be equal to that of the proton, i.e.

$$\sum_i \int_0^1 dx f_i(x) x = 1. \tag{2.15}$$

However, experimentally this value was found to be ≈ 0.5 [13]. This implies that there are also electrically neutral particles within the proton which carry $\sim 50\%$ of its momentum. These particles are identified with gluons, the gauge bosons of QCD. Direct evidence for the existence of these gluons, was provided in 1979 via the observation of 3-jet events in e^+e^- annihilation at DESY [14].

In this QCD improved QPM, the assumption that the transverse momentum of the partons is zero, in the infinite momentum frame, no longer holds. A quark can emit a gluon and acquire a large transverse momentum k_T with probability proportional to $\alpha_s\, dk_T^2/k_T^2$ at large k_T. This integral extends up to the kinematic limit, $k_T^2 \sim Q^2$, and gives rise to contributions proportional to $\alpha_s \log Q^2$ which break scaling. This was experimentally confirmed by the observation of a logarithmic dependence on Q^2 of $F_2(x, Q^2)$ and was one of the first major successes of perturbative QCD.

Figure 2.3 shows the latest measurement of the x and Q^2 dependence of F_2 from ZEUS, clearly showing these scaling violations [15]. At large values of x, where the valence quarks dominate, F_2 (and hence the quark density) can be seen to fall with increasing Q^2. At low x, where the number of "sea" quarks and gluons is larger, F_2 is clearly seen to increase with Q^2.

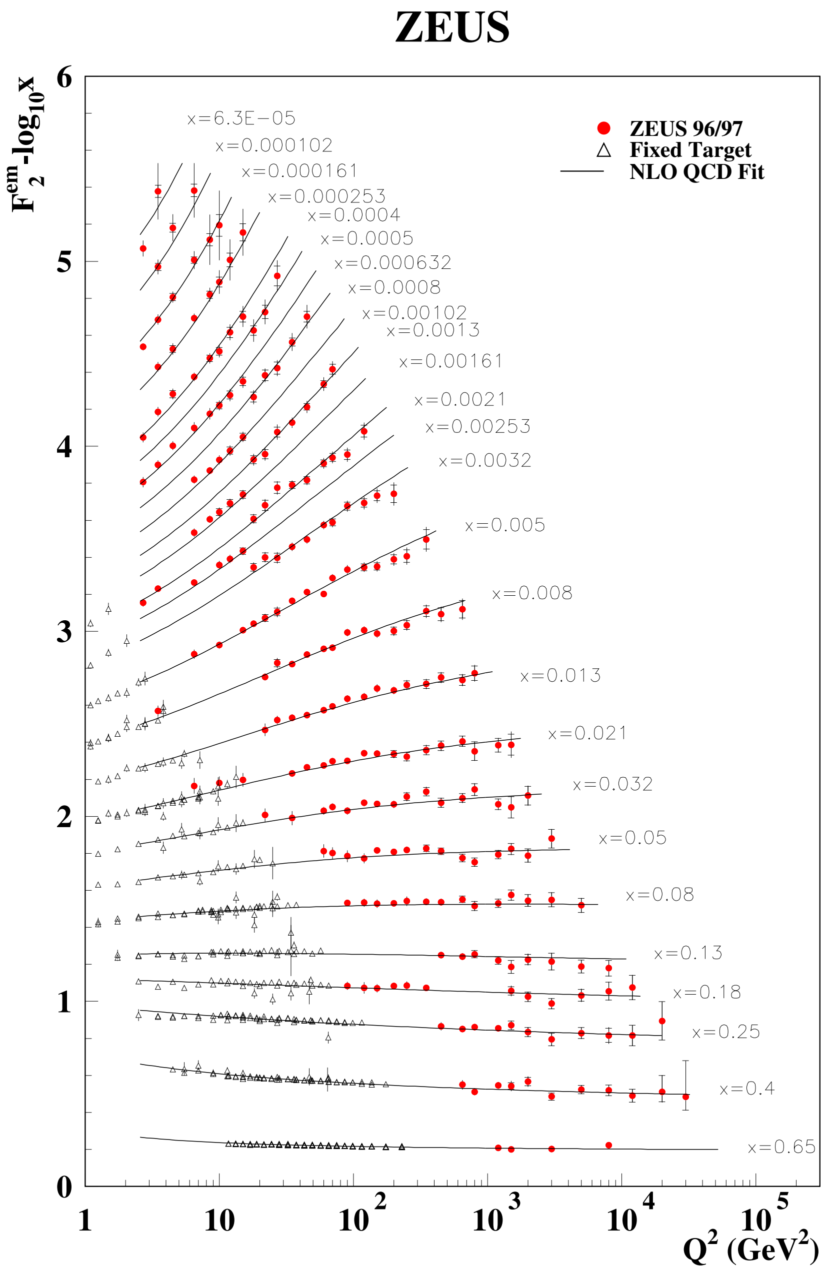

Figure 2.3: F_2^{em} *vs.* Q^2 *for fixed* x. *The fixed-target results from NMC, BCDMS, and E665 and the ZEUS NLO QCD fit are also shown.*

2.2 Evolution equations

The factorisation theorem of collinear (mass) singularities [16] states that, in a general hard collision (i.e. a scattering process involving a large transferred momentum $Q^2 \gg \Lambda^2$) of incoming hadrons, all long-distance (non-perturbative) effects can be factorised into universal (process-independent) parton densities thus leading to a perturbatively calculable dependence on the hard scattering scale Q^2, called parton evolution. This Q^2 dependence arises because a quark seen at a scale Q_0^2 as carrying a fraction x_0 of the proton momentum can be resolved into more quarks and gluons, having $x < x_0$, when the scale Q^2 is increased.

One set of parton evolution equations derived on the basis of the collinear factorisation theorem are the Dokshitzer-Gribov-Lipatov-Altarelli-Parisi (DGLAP) evolution equations [17]. The DGLAP equations describe the way the quark q and gluon g momentum distributions in a hadron evolve with the scale of the interaction Q^2.

$$\frac{dq_i(x,Q^2)}{d\log Q^2} = \frac{\alpha_s}{2\pi}\int_x^1 \frac{dy}{y}\left[q_i\left(y,Q^2\right)P_{qq}\left(\frac{x}{y}\right) + g(y,Q^2)P_{qg}\left(\frac{x}{y}\right)\right] \tag{2.16}$$

$$\frac{dg(x,Q^2)}{d\log Q^2} = \frac{\alpha_s}{2\pi}\int_x^1 \frac{dy}{y}\left[\sum_i q_i\left(y,Q^2\right)P_{gq}\left(\frac{x}{y}\right) + g(y,Q^2)P_{gg}\left(\frac{x}{y}\right)\right], \tag{2.17}$$

where $q_i(x,Q^2)$ is the quark density function, for each quark flavour i and $g(x,Q^2)$ is the gluon density function. The "splitting functions" $P_{jk}\left(\frac{x}{y}\right)$ represent the probability of a parton k of momentum fraction y emitting a parton j of momentum fraction x. This probability will depend on the number of splittings allowed in the approximation. Given a specific factorisation and renormalisation scheme, the splitting functions $P_{jk}\left(\frac{x}{y}\right)$ are obtained in QCD by perturbative expansion in α_s,

$$P_{jk}\left(\frac{x}{y}\right) = P_{jk}^{(0)}\left(\frac{x}{y}\right) + \frac{\alpha_s}{2\pi}P_{jk}^{(1)}\left(\frac{x}{y}\right) + \ldots. \tag{2.18}$$

The truncation after the first two terms in the expansion defines the next-to-leading order (NLO) DGLAP evolution. This approach assumes that the dominant contribution to the evolution comes from subsequent parton emissions which are strongly ordered in transverse momenta k_T, the largest corresponding to the parton interacting with the probe.

At small x, higher order contributions to the splitting functions of the form

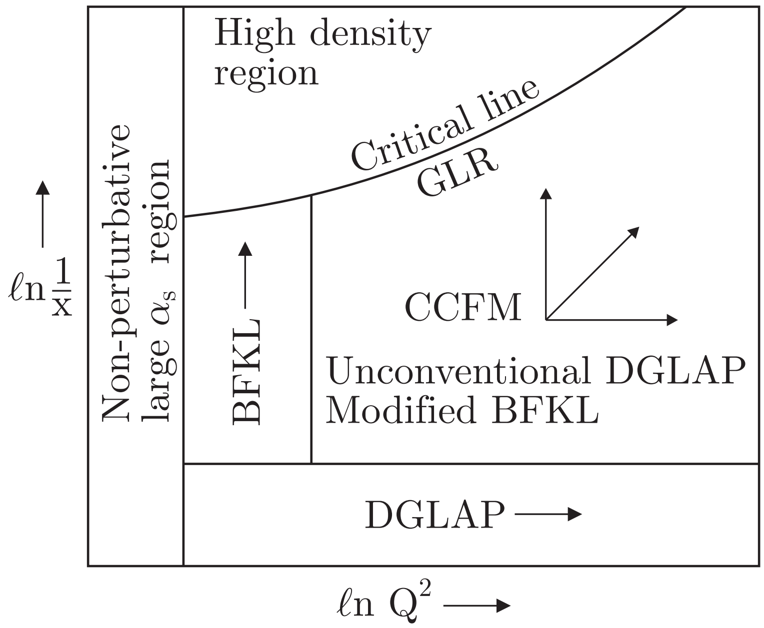

Figure 2.4: *Schematic representation of the applicability of various evolution equations across the (x, Q^2) plane.*

$$P_{ij}^{(n)} \sim \frac{1}{x} \ln^{n-1} x$$

will be enhanced, spoiling the convergence of (2.18). Thus the conventional DGLAP equations may be inadequate at low x and must either be modified or an alternative set of evolution equations used. Figure 2.4 shows the expected regions of applicability of various alternatives across the (x, Q^2) plane. The BFKL and CCFM evolution equations, which are based on a generalisation of the collinear factorisation theorem called k_T factorisation [18] will now be discussed.

2.2.1 BFKL evolution

The Balitsky-Fadin-Kuraev-Lipatov (BFKL) [19] evolution equation allows the resummation of terms with a leading $(\alpha_s \ln x)^n$ in the expansion of Equation (2.18), independent of $\ln\ Q^2$. This involves considering the evolution of a gluon distribution which is not integrated over k_T, since breaking the association to leading $\ln\ Q^2$ implies that the gluon ladder need not be ordered in k_T. The unintegrated gluon density is related to the more familiar gluon distribution by

$$xg(x, Q^2) = \int_0^{Q^2} \frac{dk_T^2}{k_T^2} \mathcal{G}(x, k_T^2). \tag{2.19}$$

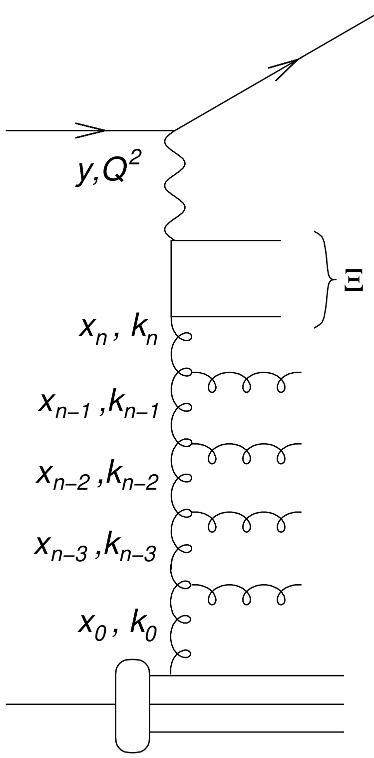

Figure 2.5: *Schematic representation of the gluon ladder and quark box Ξ.*

The BFKL equation then describes the $\ln(1/x)$ evolution of the unintegrated gluon density:

$$\frac{d\mathcal{G}(x, k_T^2)}{d\ ln(1/x)} = \int dk_T'^2 K(k_T^2, k_T'^2)\mathcal{G}(x, k_T'^2). \tag{2.20}$$

This evolution corresponds roughly to cascades with emissions strongly ordered in x with no restriction on k_T.

In order for the BFKL equation to make predictions, e.g. of F_2, the gluon ladder must be convoluted with the quark box (Figure 2.5) according to the k_T factorisation theorem:

$$F_2(x, Q^2) = \int_x^1 \frac{dy}{y} \int \frac{dk_T^2}{k_T^2} \mathcal{G}(y, k_T^2)\sigma^{box}(\frac{x}{y}, k_T^2, Q^2). \tag{2.21}$$

2.2.2 CCFM evolution

Whereas the conventional DGLAP equations deal with Q^2 evolution and may be inadequate at low x, the BFKL equation deals with $1/x$ evolution and may be inadequate at high Q^2. The Ciafaloni-Catani-Fiorani-Marchesini (CCFM) [20] evolution equations attempt to be applicable across the whole kinematic plane by summing more general classes of diagrams. They are based on the idea of coherent gluon radiation, which leads to angular ordering of gluon emissions in the gluon ladder such that $\theta_i > \theta_{i-1}$ where θ_i is the ith gluon makes to the original direction. Outside this angular region there is destructive interference such that multi-gluon contributions vanish to leading-order. Angular ordering implies ordering in k_T/E of the gluon ladder. Because of angular ordering, the unintegrated gluon distribution in CCFM depends on the maximum allowed angle, in addition to the momentum fraction x and the transverse momentum of the propagator gluon. This extra scale can be taken to be the scale Q of the probe, leading to a scale dependent gluon density $\mathcal{A}(x, k_T^2, Q^2)$.

At small x, where $\mathcal{A}$ becomes independent of Q^2 and ordering in k_T/E does not imply ordering in k_T, the integral equation for $\mathcal{A}(x, k_T^2, Q^2)$ can be approximated by the BFKL equation. However, at moderate x, k_T ordering is implied and the DGLAP equation for the integrated gluon distribution $g(x, Q^2)$is recovered. Cross sections can then be calculated according to the k_T factorisation theorem by convoluting the unintegrated gluon density with the off-shell boson gluon fusion matrix element, $\hat{\sigma}$,

$$\sigma = \int dk_T^2 dx_g \mathcal{A}(x_g, k_T^2, \bar{q}) \hat{\sigma}(\gamma^* g^* \to q\bar{q}). \tag{2.22}$$

2.3 Photon structure

The DIS cross section, given in Equation (2.9), is dominated by the exchange of very low virtuality photons. The lifetime of these photons varies as $\sim E_\gamma/Q^2$ which at very low virtualities can be long compared to the characteristic time of the hard subprocess. The electron beam can then be considered a source of approximately massless, collinear, photons and an ep collider effectively becomes a γp collider. The total cross section, σ_{tot}^{ep}, can then be factorised into contributions from the total γp cross section $\sigma_{tot}^{\gamma p}$, and some flux factor $f_{e\to\gamma}(y)$ which is the probability of finding a photon with energy $E_\gamma = yE_e$ inside the electron. In the limit $Q^2 \to 0$, the photons can only be transversely polarised, and to a good approximation

$$\frac{d^2\sigma^{ep}}{dydQ^2} \sim f_{e\to\gamma_T}(y, Q^2)\sigma_{tot}^{\gamma p}(y, Q^2), \tag{2.23}$$

where the photon flux is $f_{e\to\gamma}(y, Q^2)$, is given by

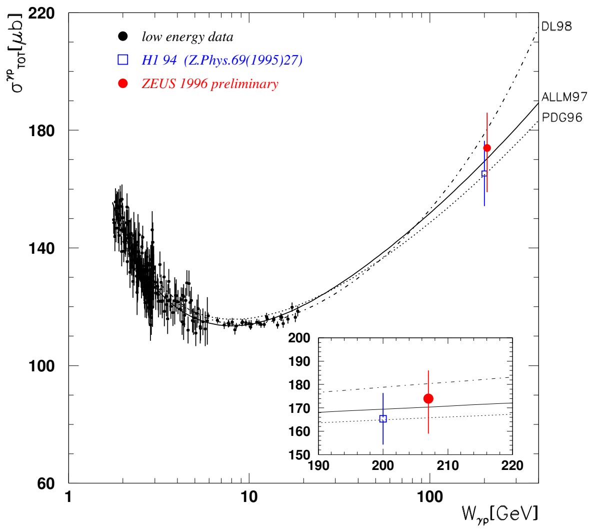

Figure 2.6: *The total photon-proton cross section.*

$$f_{e\to\gamma}(y,Q^2) = \frac{\alpha}{2\pi}\frac{1}{Q^2}\left[\frac{1+(1-y)^2}{y} - 2\frac{1-y}{y}\frac{Q^2_{min}}{Q^2}\right] \tag{2.24}$$

where $Q^2_{min} = m_e^2 y^2/(1-y)$ is the kinematic lower bound. This is known as the equivalent photon approximation (EPA). Neglecting the Q^2 dependence of the γp interaction and integrating over photon virtualities from the lower kinematic limit to some maximum, Q^2_{max}, yields

$$f^{WWA}_{e\to\gamma}(y) = \frac{\alpha}{2\pi}\left[\frac{1+(1-y)^2}{y}\ln\frac{Q^2_{max}}{Q^2_{min}} - 2\frac{1-y}{y}\left(1-\frac{Q^2_{min}}{Q^2_{max}}\right)\right], \tag{2.25}$$

which is the Weizsäcker-Williams approximation (WWA) [21].

Figure 2.6 shows $\sigma^{\gamma p}_{tot}$ measured at HERA together with the results from low energy experiments [21]. The shape strongly resembles that of meson-nucleon scattering and can be described using the same models. Here, both photon and proton behave as objects with spatial extent. These types of events are termed "soft" photoproduction. At larger momentum transfers, high transverse momentum jets of hadrons are produced, and the meson-nucleon model of scattering is no longer able to explain the observed final state. It can however be explained in terms of parton-parton scattering, where the partons which collide to produce jets of hadrons are considered to be point-like. These types of events are termed "hard" photoproduction and will now be discussed in more detail.

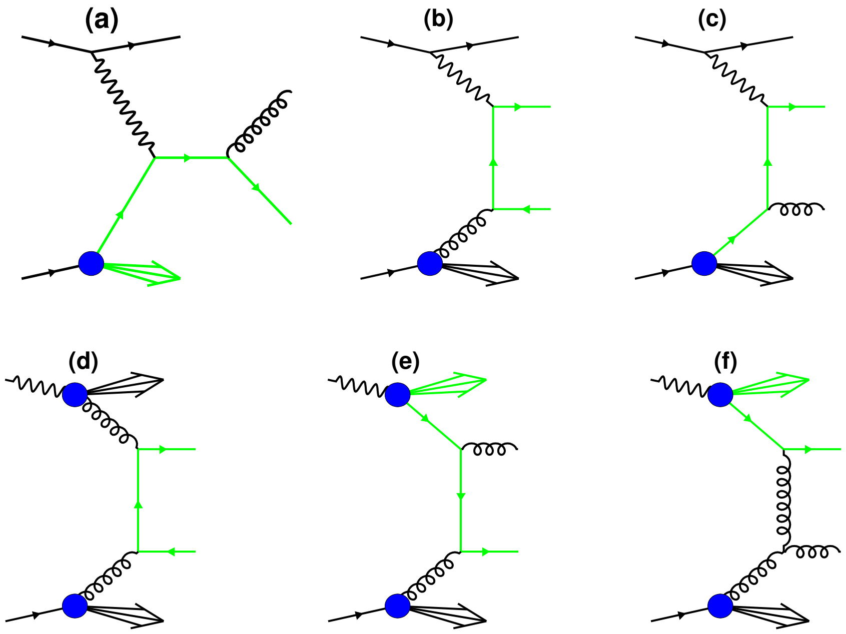

Figure 2.7: *Examples of leading-order processes resulting in two jets; (a) QCD Compton, (b) boson gluon fusion, (c) flavour excitation from the proton, (d) gluon gluon fusion, (e) and (f) flavour excitation from the photon.*

2.3.1 Hard photoproduction

At leading-order, hard photoproduction processes, such as those in Figure 2.7, can be split into two classes; "direct", where the photon takes part directly in the hard scatter (Figures 2.7(a)-(c)), and "resolved", where a parton from the photon takes part in the hard scatter (Figures 2.7(d)-(f)) and the scatter can be viewed as having resolved the structure of the photon.

These two classes of events can be separated based on the knowledge of the fraction of the photon's momentum participating in the hard scatter, x_γ. For the LO QCD diagrams shown in Figure 2.7, energy and momentum conservation yield

$$x_\gamma^{LO} = \frac{\sum_{partons} E_T^{partons} e^{-\eta^{partons}}}{2yE_e}, \tag{2.26}$$

where yE_e is the initial photon energy. For direct events, this is one and for resolved events it is less than one. By summing over jets instead of partons x_γ^{LO} can be translated into an experimentally measurable quantity, x_γ^{obs}, and Equation (2.26) becomes:

$$x_\gamma^{\mathrm{obs}} = \frac{\sum_{jets} E_T^{jet} e^{-\eta^{jet}}}{2yE_e}, \tag{2.27}$$

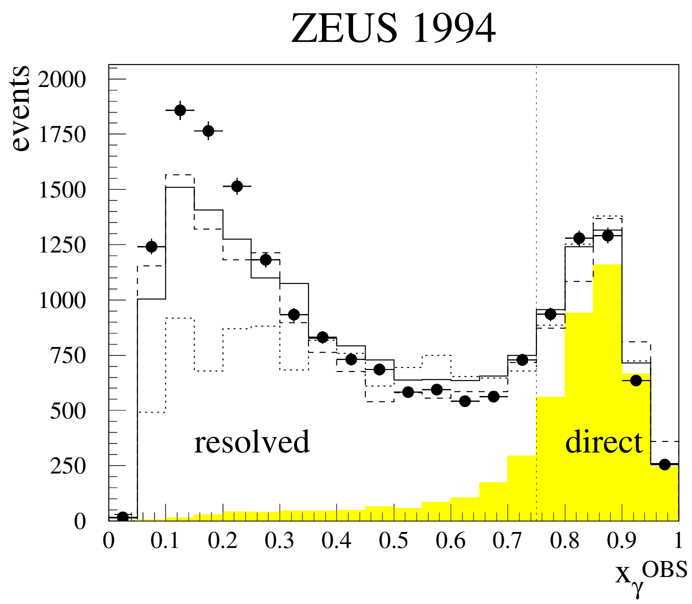

Figure 2.8: *The $x_\gamma^{\rm obs}$ distribution in dijet events for data (black dots) compared with HERWIG with and without MPI (solid line and dotted line), and PYTHIA with MPI (dashed line) Monte Carlo generators.*

where the sum runs over the two highest transverse energy jets and $x_\gamma^{\rm obs}$ is the fraction of the photon's momentum entering the dijet system.

The ability to separate direct and resolved events using $x_\gamma^{\rm obs}$ was demonstrated in [22]. Figure 2.8 shows the the measured $x_\gamma^{\rm obs}$ distribution together with the predictions of two LO Monte Carlo's. Direct events (filled histogram) are strongly peaked at $x_\gamma^{obs} > 0.75$ and the resolved at $x_\gamma^{obs} < 0.75$.

Beyond leading-order the separation between direct and resolved is ambiguous; the processes in Figures 2.7(d) and (e), classed as the resolved production of two jets at LO could be considered as the direct production of three jets at NLO. The terms direct and resolved are then only defined at leading-order, beyond this they depend on the factorisation scale and can thus have no physical meaning. The definition of $x_\gamma^{\rm obs}$, however, is valid at all orders and it remains a powerful tool to identify "photon structure like" effects.

2.3.2 Photon structure functions

The structure of the photon is measured directly in deep inelastic $e\gamma$ scattering [23], shown in Figure 2.9, which is formally analogous to deep inelastic ep scattering. The cross section for a probing photon, virtuality, $Q^2 \equiv -q^2$, scattering off a real target

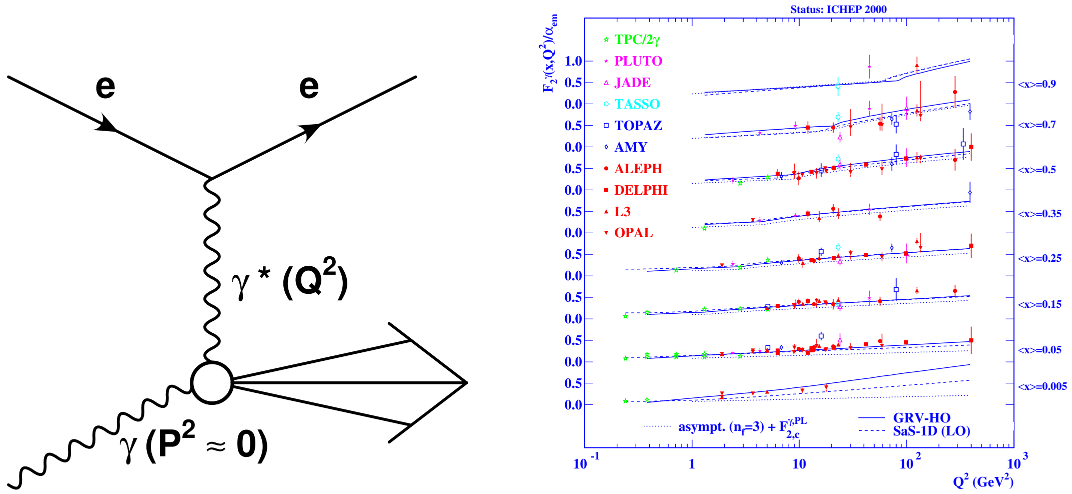

Figure 2.9: *Feynman diagram for $e\gamma$ diagram with a virtual photon, γ^*, probing an on-shell photon, γ (left). Summary of current results on F_2^γ (right).*

photon with virtuality[4] $P^2 \approx 0$ producing a final state eX is given by,

$$\frac{d^2\sigma_{e\gamma\to eX}}{dxdy} = \frac{2\pi\alpha^2 s}{Q^4}\left[\left(1+(1-y)^2\right)F_2^\gamma(x,Q^2) - y^2 F_L^\gamma(x,Q^2)\right] \tag{2.28}$$

As in ep scattering the structure function F_2^γ can be written in terms of the parton densities

$$F_2^\gamma(x,Q^2) = 2x\sum_i e_i^2 q_i^\gamma(x,Q^2), \tag{2.29}$$

where the sum runs over all quark flavours, i, of charge e_i and the factor of two accounts for quarks and anti-quarks. These parton densities obey a set of inhomogeneous evolution equations [24]:

$$\frac{dq_i(x,Q^2)}{d\log Q^2} = a(x) + \frac{\alpha_s(Q^2)}{2\pi}\int_x^1 \frac{dy}{y}\left[P_{qq}\left(\frac{x}{y}\right)q_i(y,Q^2) + P_{qg}\left(\frac{x}{y}\right)g(y,Q^2)\right] \tag{2.30}$$

$$\frac{dg(x,Q^2)}{d\log Q^2} = \frac{\alpha_s(Q^2)}{2\pi}\int_x^1 \frac{dy}{y}\left[P_{gq}\left(\frac{x}{y}\right)2\sum_i^f q_i(y,Q^2) + P_{gg}\left(\frac{x}{y}\right)g(y,Q^2)\right] \tag{2.31}$$

[4]This is the nomenclature used in two-photon interactions at LEP. Unfortunately, at HERA, Q^2 denotes the virtuality of the probed photon and the scale of the probing interaction is $\sim (E_T^{jet})^2$. Thus, to go from LEP to HERA nomenclature, $Q^2 \to (E_T^{jet})^2$ and $P^2 \to Q^2$.

where

$$a(x) = 3e_i^2 \frac{\alpha}{2\pi} \left[x^2 + (1-x)^2\right]. \tag{2.32}$$

These are the standard DGLAP evolution equations, e.g. for the proton, except for the so-called anomalous term, $a(x)$, which comes from branchings $\gamma \to q\bar{q}$, and is unique to the photon evolution equations. The solution can be written as the sum of two terms [25],

$$f_a^{\gamma}(x, Q^2) = f_a^{\gamma,NP}(x, Q^2; Q_0^2) + f_a^{\gamma,PT}(x, Q^2; Q_0^2) \tag{2.33}$$

where $a = q_i, g$, $f_{q_i}(x, Q^2) \equiv q_i(x, Q^2)$ and $f_g(x, Q^2) \equiv g(x, Q^2)$. The first term is a solution to the homogeneous equation with a non-perturbative input at $Q = Q_0$, and the second is a solution to the full inhomogeneous equation with the boundary condition $f_a^{\gamma,PT}(x, Q_0^2; Q_0^2) \equiv 0$. One possible physics interpretation is to let $f_a^{\gamma,NP}$ correspond to $\gamma \to V$ fluctuations, where $V = \rho^0, \omega, \phi, J/\psi, \ldots$ is a set of vector mesons, ("vector meson dominance"), and let $f_a^{\gamma,PT}$ correspond to perturbative $\gamma \to q\bar{q}$ fluctuations, $q = u, d, s, c$ and b ("anomalous"). The discrete spectrum of vector mesons can be combined with the continuous (in virtuality k^2) spectrum of $q\bar{q}$ fluctuations to give

$$f_a^{\gamma}(x, Q^2) = \sum_V \frac{4\pi\alpha_{em}}{f_V^2} f_a^{\gamma,V}(x, Q^2; Q_0^2) + \frac{\alpha_{em}}{2\pi} \sum_q 2e_q^2 \int_{Q_0^2}^{Q^2} \frac{dk^2}{k^2} f_a^{\gamma,q\bar{q}}(x, Q^2; k^2) \tag{2.34}$$

where each component, $f_a^{\gamma,V}$ and $f_a^{\gamma,q\bar{q}}$ obeys a unit momentum sum rule.

There are currently a large number of photon parton density parameterisations and usually involve some fits to data. With the large errors on F_2^{γ}, additional assumptions need to be made. These assumptions differ in different models and involve the treatment of heavy quarks, the choice of the scale Q_0^2 and the methods of deciding the form of the input densities.

2.4 Virtual photon structure

The evolution equations (in Q^2) of the PDFs of the virtual photon can be exactly calculated in perturbative QCD for the restricted P^2 range $Q_0^2 \ll P^2 \ll Q^2$.

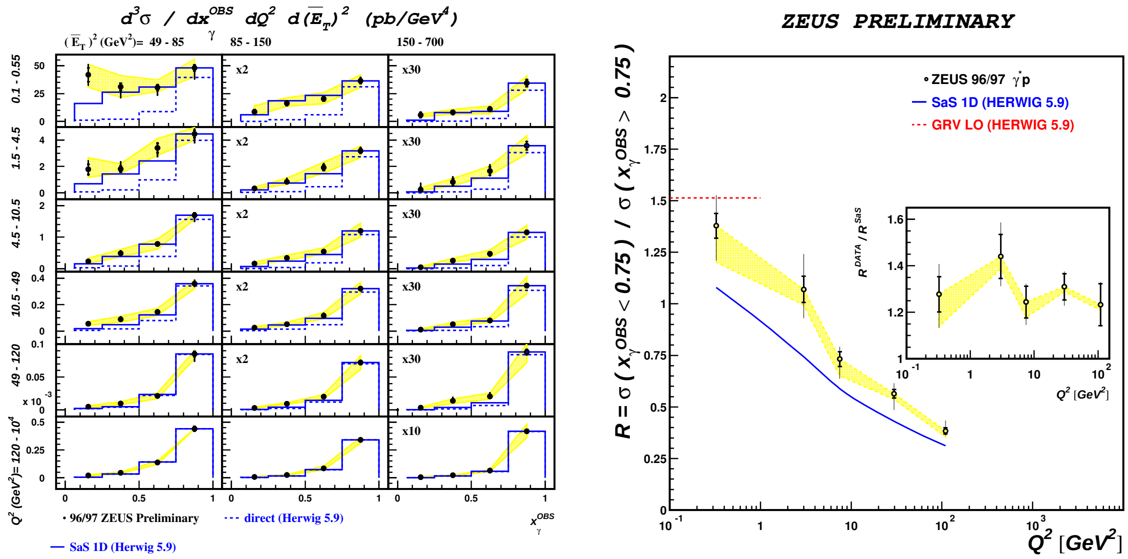

Figure 2.10: *Triple differential cross section $d^3\sigma/dx_\gamma^{obs}dQ^2d\overline{E}_T^2$ as a function of $x_\gamma^{\rm obs}$ for different regions in Q^2 and $\overline{E}_T^2$(left). The ratio of cross sections $R = \sigma(x_\gamma^{\rm obs} < 0.75)/\sigma(x_\gamma^{\rm obs} > 0.75)$ as a function of Q^2 (right).*

Theoretically challenging, however, is the region $\Lambda^2_{\rm QCD} \lesssim P^2 \lesssim Q_0^2$ where evolution equations cannot be derived from perturbative QCD.

In [26] PDFs that are valid for all $0 \leq P^2 \leq Q^2$ were proposed and a generalised form of Equation (2.34) given:

$$\begin{aligned} f_a^{\gamma^*}(x, Q^2, P^2) &= \sum_V \frac{4\pi\alpha_{em}}{f_V^2}\left(\frac{m_V^2}{m_V^2 + P^2}\right)^2 f_a^{\gamma,V}(x, Q^2; Q_0^2) \\ &+ \frac{\alpha_{em}}{2\pi}\sum_q 2e_q^2 \int_{Q_0^2}^{Q^2} \frac{dk^2}{k^2}\left(\frac{k^2}{k^2+P^2}\right)^2 f_a^{\gamma,q\bar{q}}(x, Q^2; k^2). \end{aligned} \qquad (2.35)$$

This extension of real-photon PDFs to those of the virtual photon can be applied to any set of parton distributions, provided that the VMD and anomalous parts are available separately.

2.4.1 Experimental review

Measurements of the virtual photon structure in two-photon interactions require the detection of both scattered leptons at non-zero scattering angles. This was first done by the PLUTO collaboration in 1984 [27] and, more recently, by L3 [28] and OPAL [29]. However, all these analyses suffer from low statistics. The extensive Q^2

range, together with the large centre-of-mass energies, available at HERA enable more detailed studies of the Q^2 evolution of photon structure [30–32].

Two recent results from ZEUS are shown in Figure 2.10. The measured triple differential dijet cross sections $d^3\sigma/dx_\gamma^{obs}dQ^2d\overline{E}_T^2$ are shown as a function of $x_\gamma^{\rm obs}$ in different bins of Q^2 and $\overline{E}_T^2$. For each $\overline{E}_T^2$ bin, the cross section in the low $x_\gamma^{\rm obs}$ region falls faster with increasing Q^2 than the cross section in the high $x_\gamma^{\rm obs}$ region. For the bins with $Q^2 > \overline{E}_T^2$ the data are well described by the HERWIG predictions including only LO direct processes. In the bins with $Q^2 < \overline{E}_T^2$ LO direct processes alone are not enough to describe the data.

The faster fall of the low $x_\gamma^{\rm obs}$ region can be seen more clearly in the ratio of cross sections $R = \sigma(x_\gamma^{\rm obs} < 0.75)/\sigma(x_\gamma^{\rm obs} > 0.75)$. The ratio of the data falls with increasing Q^2. The HERWIG prediction, using the suppressed virtual photon structure function SaS1D [25], also falls with increasing Q^2 and describes the shape but not the normalisation of the ratio (requiring a normalisation factor of 1.3).

2.5 Heavy flavour production

The conventional QCD parton model is formulated in the zero mass parton limit. There are two basic methods of treating charm in the evolution equations based on the factorisation equation [33]

$$\sigma_{N\to X}(S,Q^2) = \sum_i q_i(x,\mu^2) \otimes \hat{\sigma}_{i\to X}(s,Q^2,\mu^2) \tag{2.36}$$

where i is the sum over all flavours which can actively participate in the interaction at the energy scale Q^2. $\hat{\sigma}$ is the cross section for the hard scatter which is convoluted with the parton distribution functions $q_i(x,\mu^2)$ where μ is the factorisation scale. Charm can then either be included in the sum as an active flavour above some threshold (variable flavour number (VFN)) or excluded from the initial state and treated separately (fixed flavour number (FFN)). In principal, the two alternatives can be regarded as two different but equivalent schemes for organising the perturbation series in pQCD. In practice, since the perturbation series is terminated after one or two terms, the effectiveness of the two approaches can be quite different in different kinematic regions. For a full review of the theoretical and experimental status of heavy flavour production see, for example, [34] and references therein.

Massive FFN3 scheme

In this scheme, the number of active quark flavours is fixed, independent of Q^2. Only light quarks (u, d, s) are included in the initial state proton and photon and charm quarks are only produced dynamically in the hard process. The presence of the two large scales[5], μ^2 and m_c^2, can spoil the convergence of the perturbative series because the neglected terms of orders higher than α_s^2 contain $\log(\mu^2/m_c^2)$ factors that can become large. Therefore the results of massive FFN3 calculations are expected to be most accurate at $\mu^2 \simeq m_c^2$ and to become less reliable when $\mu^2 \gg m_c^2$.

Massless VFN scheme

In this scheme, charm is treated as an additional active flavour with zero mass above some threshold, $\mu^2 \sim m_c^2$. In this way, the large logarithms in μ^2/m_c^2 present at high μ are automatically resummed. This means that besides charm produced in the hard process flavour excitation processes are also included. Therefore the results of massless VFN calculations are expected to be most accurate at $\mu^2 \gg m_c^2$ and to become less reliable when $\mu^2 \simeq m_c^2$.

2.5.1 Experimental review

Deep inelastic scattering

Early studies of charm production in DIS [35] suggested that the production of charmed mesons in ep collisions is dominated by the boson gluon fusion (BGF) mechanism, already shown in Figure 2.7(c). Calculations for this process exist to NLO and the cross section depends directly on the gluon density in the proton. If the gluon density from the inclusive measurement of F_2 are used in the calculation, the results can be compared to the measured charm cross section, giving a powerful cross check of pQCD which states that the same, universal, gluon distribution should contribute to both the inclusive structure function F_2, and the exclusive charm structure function $F_2^{c\bar{c}}$. In addition, the presence of two large scales, namely, the virtuality of the exchanged boson (Q^2) and the square of the charm quark mass (m_c^2), provides a testing ground for resummation techniques. Figure 2.11 show the differential D^* cross sections measured at ZEUS compared to a massive FFN3 NLO calculation [36] which uses the gluon density extracted from fits to F_2 as input. The description of the Q^2, x and W distributions is very good, confirming the

[5]In DIS μ is the photon virtuality, Q, in photoproduction it is p_T.

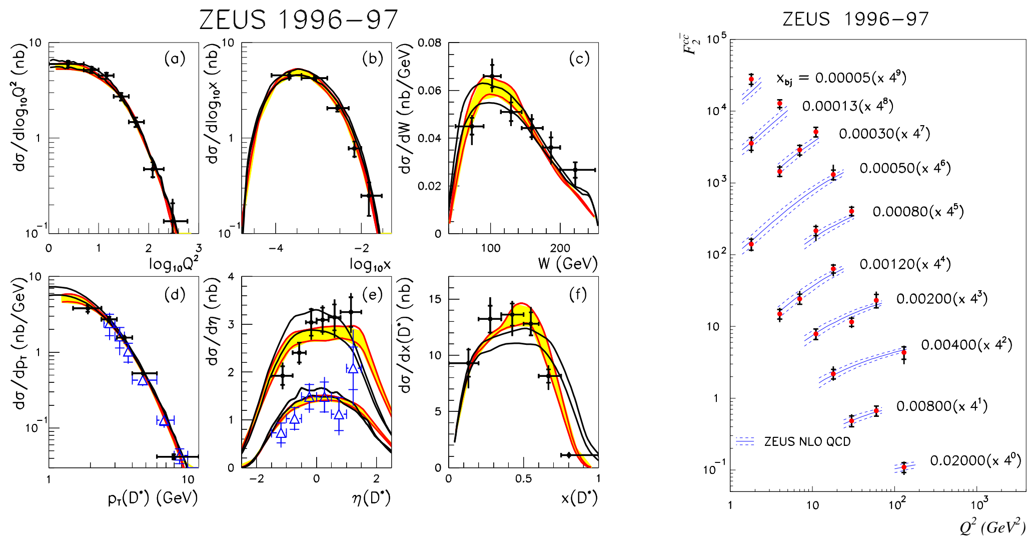

Figure 2.11: *Differential cross sections for D^* production in DIS. The open (shaded) band shows the result of an NLO QCD calculation using Peterson (RAPGAP extracted) fragmentation (left). $F_2^{c\bar{c}}$ as a function of x and Q^2 (right).*

universality of the gluon distribution. However, in order to describe the $p_T(D^*)$ and $\eta(D^*)$ distributions it was necessary to use a charm fragmentation extracted from the LO Monte Carlo RAPGAP. With this fragmentation included the description is good enough to be used to extrapolate the measurement into the full D^* phase space and extract $F_2^{c\bar{c}}$. The measured $F_2^{c\bar{c}}$ is compared to the value derived from the gluon distribution extracted from NLO fits to F_2 in Figure 2.11.

Photoproduction

NLO calculations for the photoproduction of heavy quarks such as charm also exist, where the heavy quark mass or the high transverse momentum of the produced partons is used as the hard scale. Significant differences between calculation schemes can be expected since massless VFN calculations will include charm excitation processes and thus predict, for a given factorisation scale, a larger resolved component in comparison with a massive FFN3 calculation. Therefore, it is interesting to compare the predictions of these models to data and to investigate the sensitivity of the experimental results to the partonic content of the photon and specifically to the charm excitation contribution.

Figure 2.12 shows the differential cross section $d\sigma/d\eta^{D^*}$ for various ranges of p_T measured at ZEUS compared to both massive and massless calculations [37]. As expected as $p_T \to m_c$ the description of the data by the massless calculation degrades. However, the NLO predictions generally lie below the data, particularly

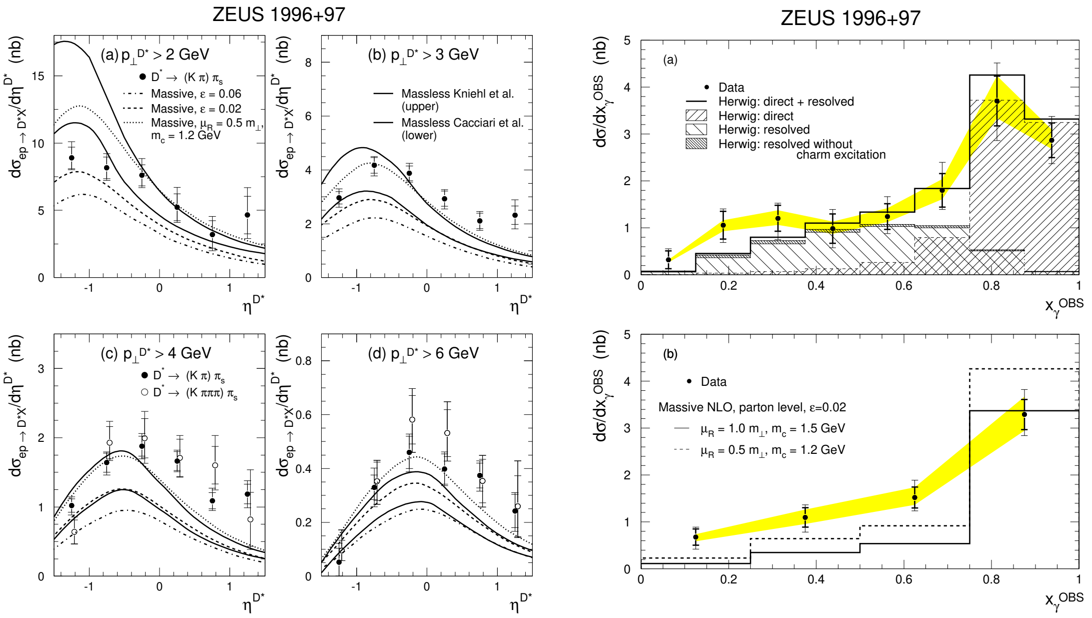

Figure 2.12: *The differential cross section $d\sigma/d\eta^{D^*}$ for photoproduction compared to several NLO calculations (left). The differential cross section $d\sigma/dx_\gamma^{\rm obs}$ for dijets with an associated D^* (right) compared to LO (upper) and NLO (lower) predictions.*

in the forward region, in all the plots. Given the discrepancy between data and NLO predictions in the inclusive D^* measurements it is important to study the kinematics of charm production in more detail. This was done in the same paper by measuring the dijet cross section as a function of $x_\gamma^{\rm obs}$, also shown in Figure 2.12. At LO the data require a resolved contribution of 45%, this compares to 75% for the $x_\gamma^{\rm obs}$ cross section of Figure 2.8 which did not require the presence of a D^*. The charm excitation contribution to the LO resolved process was 93% in the Monte Carlo. The prediction of a massive NLO calculation, lies significantly below the data for $x_\gamma^{obs} < 0.75$, however a massless calculation could be expected to give a better description.

Chapter 3

Kinematic reconstruction

The event and jet kinematics must be reconstructed from measured quantities. The methods used for the reconstruction of the event variables in this thesis are now described.

3.1 Reconstruction of y and Q^2

There are many ways of reconstructing the variables y and Q^2 [38], two of which are used in this thesis; the "electron" and "Jacquet-Blondel" methods.

3.1.1 Electron method

The electron method is theoretically simple and relies only on the knowledge of the energy of the scattered lepton, E_e' and the angle of the scatter, θ_e. For a given initial lepton energy, E_e, the variables, y and Q^2 can be calculated from the scattered lepton's energy E_e' and polar angle θ_e as follows:

$$y_e = 1 - \frac{E_e'}{2E_e}\left(1 - cos\theta_e\right), \tag{3.1}$$

$$Q_e^2 = 2E_eE_e'\left(1 + cos\theta_e\right). \tag{3.2}$$

This assumes that there were no additional emissions from the lepton, i.e. that it entered the hard scatter with the beam energy E_e and it left with the measured energy E_e' and as a result is sensitive to both initial- and final-state electroweak radiative corrections (ISR and FSR).

3.1.2 Jacquet-Blondel method

The Jacquet-Blondel method [39] calculates the variables y and Q^2 from the hadronic final state and can thus be used when the scattered lepton is not measured. The hadronic final state is defined as all particles except the scattered lepton and summing over these gives:

$$y_{\mathrm{JB}} = \frac{\sum_i (E_i - p_{z_i})}{2E_e}, \tag{3.3}$$

$$Q^2_{\mathrm{JB}} = \frac{(\sum_i p_{x_i})^2 + (\sum_i p_{y_i})^2}{1 - y_{\mathrm{JB}}}. \tag{3.4}$$

Experimentally this sum is not over hadrons but calorimeter cells. If the scattered lepton is found in the calorimeter, then the cluster of cells associated with it are eliminated from the calculation. If the scattered lepton is misidentified its energy deposit will enter into the above summations. This results in high values of y_{JB}, allowing events with an unidentified electron to be rejected.

Since this method measures the energy transferred *to* the hadronic system, it is unaffected by FSR, however it will still be sensitive to ISR through E_e.

Resolutions

The resolutions on y and Q^2 using the two methods described above are shown in Figure 3.1. The Q^2 resolution is significantly worse using the Jacquet Blondel method. This is a result of energy lost due to dead material and acceptance. As a result, Q^2_{JB} is only used in high-Q^2 events when there is no scattered electron, i.e. charged current DIS. Thus, when an electron is present in an event the electron method has been used to reconstruct Q^2. When there is no identified lepton, Q^2 is restricted to be below 1 GeV^2 by means of an anti-tag requirement (see Section 4.3).

The y resolution is again better using the electron method, and there is a systematic bias in the measurement of y_{JB} due to energy loss in dead material before the CAL. However, in order to be consistent at different Q^2 regions, y_{JB} is used for the estimate of y whether or not an electron is found.

3.2 Jet reconstruction

There are two types of jet algorithm in common use; the "cone" and "cluster" algorithms. In the analysis presented in this thesis both types of algorithm are

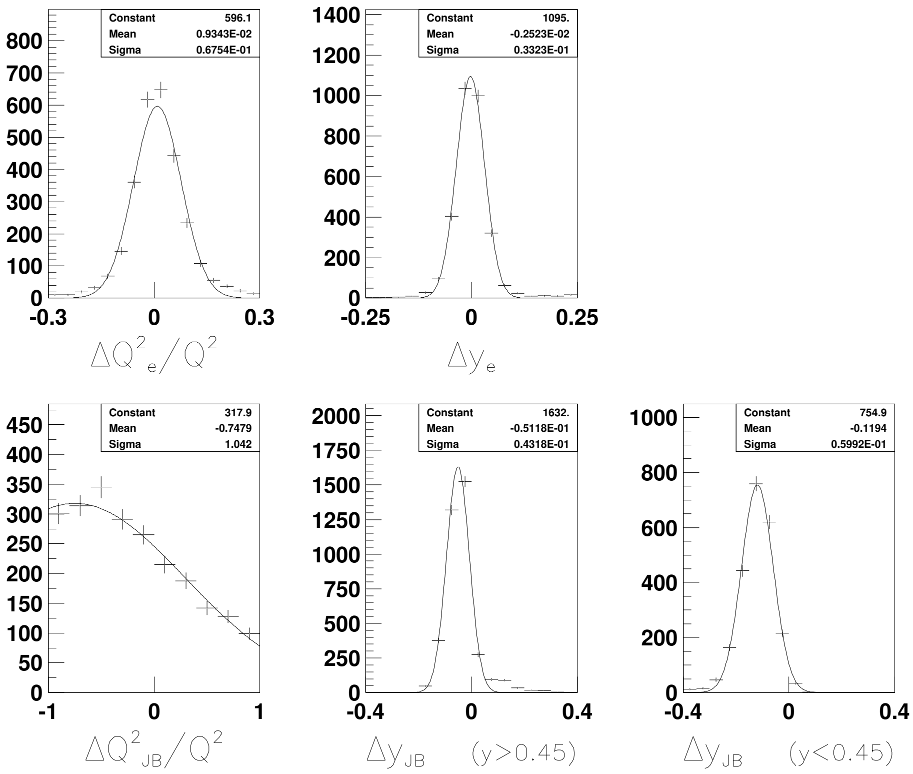

Figure 3.1: *y and Q^2 resolutions using the electron and Jacquet Blondel methods.*

used. The EUCELL cone algorithm is used in the online trigger selection, described in Section 4.2, and the KTCLUS [40] algorithm is used in the offline selection, described in Section 4.3, and the cross section definition of Section 4.1.

Detailed discussions of each of these can be found elsewhere [41], so only a brief description is included here.

3.2.1 Cone algorithm

The Snowmass Convention [42] for cone algorithms defines the transverse energy and the coordinates of a cone jet as;

$$E_T^{jet} = \sum_i E_{t,i}$$

$$\eta^{jet} = \frac{1}{E_T^{jet}} \sum_i E_{t,i}\eta_i \tag{3.5}$$

$$\phi^{jet} = \frac{1}{E_T^{jet}} \sum_i E_{t,i}\phi_i$$

where the sum runs over all hadron or calorimeter cells within the cone defined by a given prescribed radius, R, in $\eta - \phi$ space.

In EUCELL, the hadrons/cells are clustered using a grid in $\eta - \phi$ space. The size of the cells that make up the grid are determined such that $\Delta\eta^{gridcell} \approx \Delta\phi^{gridcell} \approx R/2$. By then sliding a 3 $\times$ 3 cell window over the grid, a potential pre-cluster is then formed. To be called a pre-cluster, it must be above some prescribed transverse energy. A cone of radius R is then placed around the pre-cluster and the centre of the pre-clusters are then recalculated and the process repeated until some stable situation (or some maximum number of iterations) is reached. The first jet is defined as the cone with the highest transverse energy. Successive jets are then determined from the remaining objects by the same procedure until there exist no more cones above a certain energy threshold.

3.2.2 Clustering algorithm

The use of the cone algorithms leads to ambiguities. The treatment of overlapping jets is not defined within the Snowmass convention, nor is the question of seed finding for the initial jets. This leads to theoretical ambiguity with respect to jet merging in the final state and the process is not infra-red safe at NNLO without modification [43].

These problems are avoided by the use of the k_T algorithm, as the merging criterion is completely defined for any given final state.

For a cluster algorithm some distance measure which determines *which* particles will be merged must be specified, together with a recombination scheme which defines how they will be merged. In this thesis the algorithm is run in the laboratory frame using the inclusive recombination scheme of Ellis and Soper [44] in a mode which is invariant under longitudinal boosts, the recombination scheme being similar to that of the Snowmass Convention (the so-called "*pt*" mode). The algorithm scheme depends on a parameter R which is analagous to a cone radius.

To decide which particles should be merged, for each particle i the quantity,

$$d_i = E_{T,i}^2$$

is formed and for each pair of particles, ij, the quantity

$$d_{ij} = \min(E_{T,i}^2, E_{T,j}^2)\left[(\eta_i - \eta_j)^2 + (\phi_i - \phi_j)^2\right]/R^2.$$

is formed. The d_i is the limiting case of small angles of the "distance" between particle i and a large mass remnant traveling along the z direction.

If the smallest of all the d values is a d_{ij}, then particles i and j are merged into a single object, k. If however, the smallest value is a d_i then this particle is considered "complete" and is removed from further clustering. This process is then repeated until all the objects have been removed, producing an E_T ordered list of objects.

The scheme for merging the objects is similar to the Snowmass Convention, and is,

$$E_{T,k} \equiv E_{T,i} + E_{T,j} \tag{3.6}$$

$$\eta_k \equiv \frac{E_{T,i}\eta_i + E_{T,j}\eta_j}{E_{T,k}} \tag{3.7}$$

$$\phi_k \equiv \frac{E_{T,i}\phi_i + E_{T,j}\phi_j}{E_{T,k}}. \tag{3.8}$$

Therefore the scheme assigns objects to jets in a well-prescribed manner, and as each quantity $E_T, \Delta\eta, \Delta\phi$ in the distance parameter are each invariant under longitudinal boosts, so the property of boost invariance of the jet finding itself is retained.

Resolutions

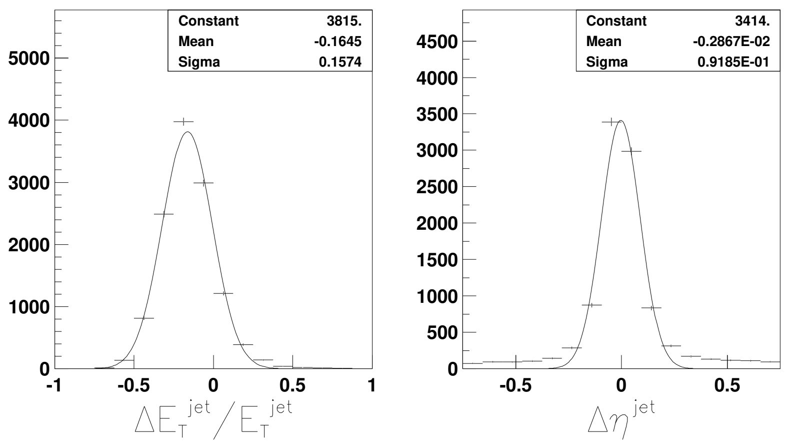

Figure 3.2: *Jet E_T and η resolutions for CAL cell jets using the KTCLUS algorithm.*

The effect of energy loss in dead material before the CAL can clearly be seen in the E_T^{jet} resolution with jets losing, on average, 16% of its energy.

3.3 $x_\gamma^{\rm obs}$ reconstruction

$x_\gamma^{\rm obs}$ was defined in Equation (2.27) in terms of E_T^{jet}, η^{jet} and y. Once again $y_{\rm JB}$ is used to estimate y. This has the advantage that, since both E_T^{jet} and $y_{\rm JB}$ are

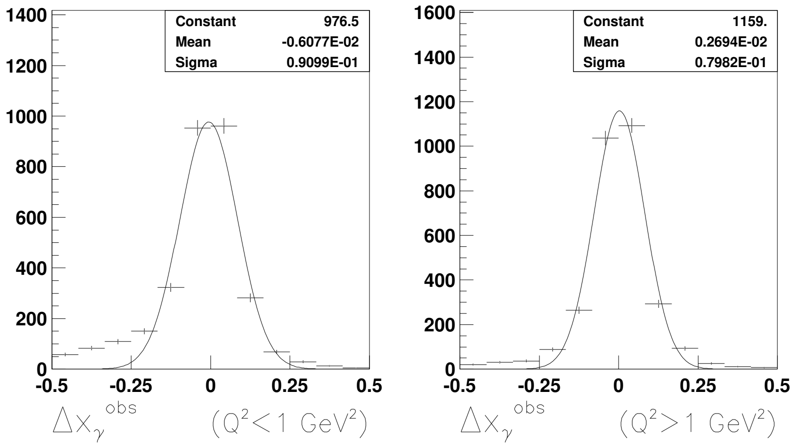

Figure 3.3: x_γ^{obs} *resolution in photoproduction and DIS.*

underestimated due to energy loss in dead material, x_γ^{obs} itself is much less sensitive to energy loss. This can be seen in Figure 3.3, which shows the x_γ^{obs} resolution for photoproduction and DIS events, where the mean is ≈ 0 in both cases. x_γ^{obs} will also be insensitive to ISR since the E_e factors in equations (2.27) and (3.3) cancel out.

Chapter 4

Event selection

Two previous ZEUS analyses have demonstrated a suppression of the low $x_\gamma^{\rm obs}$ cross section; the dijet analysis presented in Section 2.4.1 found a suppression of the low $x_\gamma^{\rm obs}$ cross section with increasing Q^2; and the charm in dijet photoproduction analysis, presented in Section 2.5.1, found a reduced low $x_\gamma^{\rm obs}$ cross section when charm was required. The analysis which will now be presented combines these two analyses in order to determine whether these two suppressions, with Q^2 and the presence of charm, are independent. Data was used from the years 1996 to 2000 giving an integrated luminosity of 103.7 $\rm pb^{-1}$.

4.1 Definition of the cross sections

Events with at least one candidate D^* meson, together with at least two high E_T jets in the process $ep \rightarrow D^* + jet + jet + X$ were considered. Using these events, the cross sections at low and high $x_\gamma^{\rm obs}$ were measured as a function of Q^2:

$$\frac{d\sigma_{ep\rightarrow D^*X}(x_\gamma^{\rm obs} < 0.75)}{dQ^2} \quad , \quad \frac{d\sigma_{ep\rightarrow D^*X}(x_\gamma^{\rm obs} \geq 0.75)}{dQ^2} \quad ; \quad 0 < Q^2 < 5000 \text{ GeV}^2 \tag{4.1}$$

This was done in the kinematic region defined by the following:

$$\begin{aligned} 0.2 \ &< \ y \ < \ 0.65; \\ E_T^{jet1,jet2} \ &> \ 7.5, \ 6.5 \text{ GeV}; \\ |\eta^{jet}| \ &< \ 2.4; \\ p_T(D^*) \ &> \ 3 \text{ GeV}; \\ |\eta(D^*)| \ &< \ 1.5. \end{aligned} \tag{4.2}$$

4.2 Online event selection

The three level trigger system employed by ZEUS has already been described in general terms in Section 1.6. The particular trigger logic used in the analysis presented here is now described.

4.2.1 First Level Trigger (FLT)

To pass the slot used at the FLT, slot 42, one of four thresholds at the Calorimeter FLT (CFLT), five vetoes and a track quality demand must be satisfied.

- The four CFLT thresholds are:
  - Total calorimeter energy > 15 GeV,
  - Total ElectroMagnetic Calorimeter (EMC) Energy > 10 GeV.

  These "total" energies exclude the three inner rings around the FCAL and the inner ring around the RCAL beampipe, corresponding to a region in pseudorapidity of approximately $-3.66 < \eta < 2.2$.

  - RCAL EMC energy > 2 GeV.

  This also excludes the inner ring around the RCAL beam-pipe.

  - BCAL EMC energy > 3.4 GeV.
- The veto criteria were:
  - The timings observed in the two C5 counters should match with physics timing, but not with that of the beam gas.
  - Two vetoes requiring that no coincidence of the inner and outer veto wall is detected.
  - The timing in the SRTD should match with physics events and not with beam-gas events.
  - Events should have `TrKclass>2`. These are events with a relatively high ratio of vertex to total number of tracks. The exact value of the ratio is dependent on the number of vertex and non-vertex tracks, but is approximately $> 25 - 30\%$.
- The tracking demand requires the event to have at least one track found by the CTD-FLT coming from the nominal interaction region, $-50\text{cm} < z_{vtx} < 80\text{cm}$.

4.2.2 Second Level Trigger (SLT)

To pass the slot used at the SLT, HPP01, the following must be satisfied:

- -60 cm < z_{vtx} < 60 cm;
- there must be at least 1 vertex track;
- $E - P_z > 8.0$ GeV, where E is the energy sum of calorimeter cells and P_z the vector sum of longitudinal momentum of all cells;
- $E_T(\text{box}) > 8.0$ GeV, where $E_T(\text{box})$ is the sum of transverse energy, E_T in all calorimeter cells excluding the first ring around the FCAL beampipe (outside a value of about $\eta = 3$)
- ($E - P_z > 12.0$ GeV) or ($p_z/E < 0.95$).

4.2.3 Third Level Trigger (TLT)

At the TLT the final online event selection is made, making use of a cone jet algorithm and a cut down version of the offline tracking. To pass the branch used at the TLT, HPP14, the following criteria must be satisfied:

- -60 cm $< z_{vtx} <$ 60 cm;
- number of bad tracks is less than 6 where a bad track does not satisfy the following:
  - the number of degrees of freedom should be > 20,
  - $p_T \geq 0.2$ GeV,
  - -3.13 < η < 1.75,
  - the number of hits used in CTD axial superlayers > 5
  - the number of hits used in CTD stereo superlayers > 5
  - the distance of closest approach in z to the vertex must be $\leq$ 75 cm.
- 5.0 GeV $< E - P_z <$ 75.0 GeV;
- $E_T(10°\text{cone}) > 5.0$GeV, where $E_T(10°\text{cone})$, is the sum of all the E_T in the calorimeter cells outside a 10° cone ($\eta < 2.44$) around the FCAL beampipe;

- $p_z/E < 1.0$;

- a simplified version of the EUCELL jet cone algorithm is run at the TLT and there must be at least two jets with the following:

$$\eta(jet) < 2.5;$$

$$E_T(jet) > 4 \text{ GeV};$$

This transverse energy requirement was raised to $E_T^{TLT} > 4.5$ GeV for the e^+ running periods in 1999 and 2000.

4.2.4 Efficiency of the trigger chain

The efficiency of the above three stage trigger chain has been extensively studied in previous dijet analyses [45, 46]. Only a brief summary of these studies is presented here.

FLT

The FLT slot was studied [45] by choosing an independent trigger which subsequently fed into the SLT and TLT used in this analysis. A LUMI branch of the FLT was chosen which required the observation of a scattered positron in the LUMI detector with some low energy calorimeter thresholds. The fraction of events passing the LUMI branch which also pass the calorimeter triggers was found to agree reasonably well between data and Monte Carlo.

SLT

The SLT slot was studied [45] using the LUMI SLT, which has events from the FLT which then pass the TLT used in this analysis. The LUMI SLT has the same requirements as the LUMI FLT with the additional criterion that the energy in the LUMI is more than 5 GeV. Reasonable agreement between data and Monte Carlo was again seen.

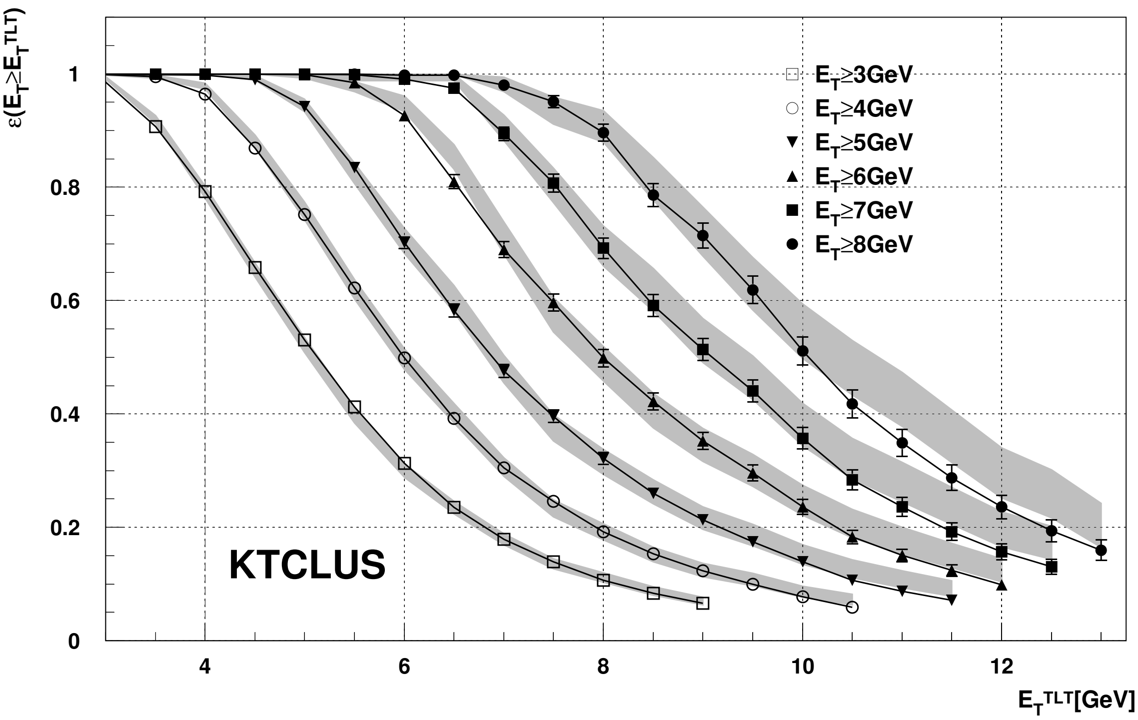

Figure 4.1: *TLT Efficiency for data (points) and Monte Carlo (bands).*

TLT

The TLT was studied [46] using the D^* TLT, which has events from the FLT and SLT used in this analysis. The D^* TLT uses the TLT tracking to reconstruct D^* mesons using the mass difference method used in this analysis. The overall efficiency of the trigger was found to be good and to increase with E_T, such that for $E_T > 6$ GeV, the efficiency is almost 100%. The Monte Carlo models the efficiency reasonably well.

Shown in Figure 4.1 is the TLT trigger efficiency for various online and offline jet selection criteria. With a TLT requirement of $E_T^{TLT} > 4$ GeV the efficiency for offline jets found using the KTCLUS algorithm on CAL cells with $E_T^{CAL} > 4$ GeV is almost 95%. When the TLT requirement is raised to $E_T^{TLT} > 4.5$ GeV, as happened for the e^+ running periods in 1999 and 2000, this efficiency is reduced to just over 85%. The variation in the efficiency is well described by the Monte Carlo.

4.3 Offline event selection

4.3.1 Corrections

Before offline selection criteria were applied corrections for the CTD B-field, calorimeter noise and scale were implemented.

CTD B field

High statistics studies of various mass peaks (J/ψ, D etc.) suggest, very strongly, that the magnetic field used by the offline tracking (VCTRAK) is too low by about 0.3%. To account for this the p_T of all tracks, which is proportional to B, was scaled by a factor of 1.003.

Calorimeter noise

Within the calorimeter, a number of cells are described as being "noisy". The effect is corrected for using standard routines for each year [47]. The corrections fall into distinct categories; the removal of noisy cells, according to lists provided each year, a cut on the relative cell imbalance, and the removal of isolated EMC and HAC cells with energies below 80 and 140 MeV respectively. The noise associated with the imbalance and isolation cuts arises predominantly due to sparks in the PMT's, whereas the noisy cells are mainly from electronic malfunctions.

Calorimeter scale

Studies have shown differences in the energy scale of the calorimeter between data and Monte Carlo [48]. In order to account for this the energies of cells in the BCAL were scaled by a single factor of 5% and cells in the RCAL were scaled by cell-by-cell factors [49]. These cell-by-cell factors were obtained using kinematic peak events and averaged 2.2%. No scale factor was applied to FCAL cells.

Electron energy

If there is SRTD information present in the event then this is used to correct the electron energy for losses before it entered the CAL. If there is no SRTD information present in the event, but there are deposits in the presampler tiles, then the presampler is used to correct the energy.

4.3.2 Kinematic selection

Events passing all the trigger requirements were separated offline into photoproduction and DIS subsamples.

Photoproduction (PHP)

PHP events were selected by requiring that no identified electron [50] was found in the CAL with energy $E_e^{'} > 5$ GeV or $y_e < 0.7$. Above 5 GeV the electron finder approaches 100% efficiency. The y_e cut provides an additional check since electrons with $E_e^{'} < 5$ GeV will be peaked at high y. The resulting sample had $Q^2 < 1.0$ GeV^2 with an estimated median of 10^{-3} GeV^2.

Deep Inelastic Scattering (DIS)

DIS events were selected by requiring that the outgoing positron (electron) was measured in a well understood region of the CAL. Specifically, electrons must enter the calorimeter outside the H shaped region around the rear beampipe shown in Figure 4.2. Inside this box cut the electron shower may not be fully contained in the CAL and there are regions of dead material which are poorly simulated in the Monte Carlo.

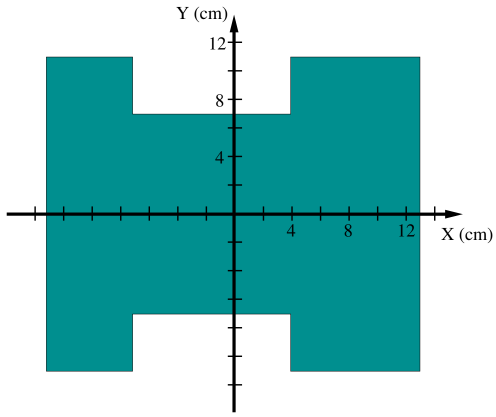

Figure 4.2: *Box cut applied to the scattered electron.*

The energy of the scattered positron (electron) was further required to satisfy $E_e^{'} > 10.0$ GeV. The cells assigned to the scattered positron (electron) were then removed from the event so that they didn't contaminate to the $y_{\rm JB}$ sum or jet search. Using the scattered electron this subsample was then subdivided into four Q^2 regions: $1.0 < Q^2 < 4.5$, $4.5 < Q^2 < 10.5$, $10.5 < Q^2 < 49.0$ and $49.0 < Q^2 < 5000.0$ GeV^2.

Jet selection

For both samples additional cuts of $|z_{vtx}| < 50$ cm and $0.15 < y_{\rm JB} < 0.55$ were applied. Owing to the energy lost in the inactive material in front of the CAL and to particles lost in the rear beampipe, $y_{\rm JB}$ systematically underestimates the true y by approximately 10-20%, an effect which is adequately reproduced in the Monte

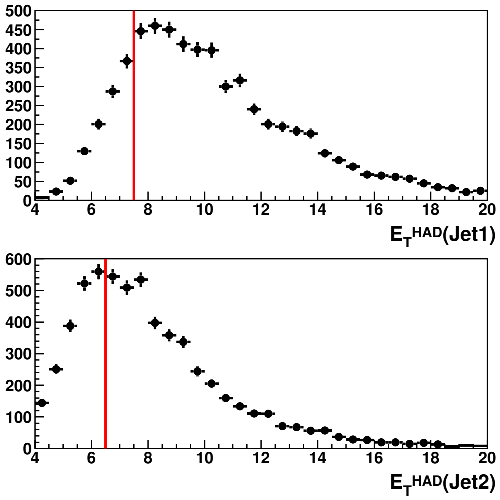

Figure 4.3: *Hadron level E_T^{jet} in GeV for events passing all detector level cuts.*

Carlo simulation of the detector. The combination of y_{JB} and $E_e^{'}$ cuts ensure that the two samples correspond to the same true y range $(0.2 < y < 0.65)$.

The longitudinally invariant k_T algorithm in the inclusive mode was then applied to the CAL cells to search for events with two jets in the final state. The two jets with the highest transverse energy in the pseudorapidity range $|\eta^{jet}| < 2.4$ were required to have transverse energies satisfying $E_T^{jet} > 4.0$ GeV. Figure 4.3 shows the true E_T^{jet} distributions for events passing these cuts. The difference is a result of energy lost in the inactive material in front of the CAL. These cuts then approximate the true kinematic region $E_{T,1}^{jet} > 7.5$ GeV and $E_{T,2}^{jet} > 6.5$ GeV, where the cross sections of Section 4.1 are measured.

4.3.3 D^* reconstruction

D^* mesons were reconstructed in the decay channel $D^{*\pm} \rightarrow D^0\pi_s^{\pm} \rightarrow (K^{\mp}\pi^{\pm})\pi_s^{\pm}$ using the mass difference method [51]. All tracks which were measured by the CTD, had hits in at least three superlayers, and were assigned to the primary event vertex were selected. Since it is not possible to distinguish between tracks from pions and kaons, all pairs of tracks were analysed and alternately assigned to be either of type "kaon", that is assigned the mass of a kaon, or of type "pion". All the combinations of tracks with opposite charge and $p_T(K,\pi) > 0.45$ GeV were combined to form D^0 candidates which were kept if their mass was in the range $1.8 < m(D^0) < 1.92$ GeV. These D^0 candidates were then combined with a track of type "pion", called the "slow pion", π_s due to its low energy, which had the opposite charge to the track of type "kaon" and, $p_T(\pi_s) > 0.15$ GeV. This combination of three tracks then formed a D^* candidate which was accepted if $p_T(D^*) > 3$ GeV and $|\eta(D^*)| < 1.5$. The cut

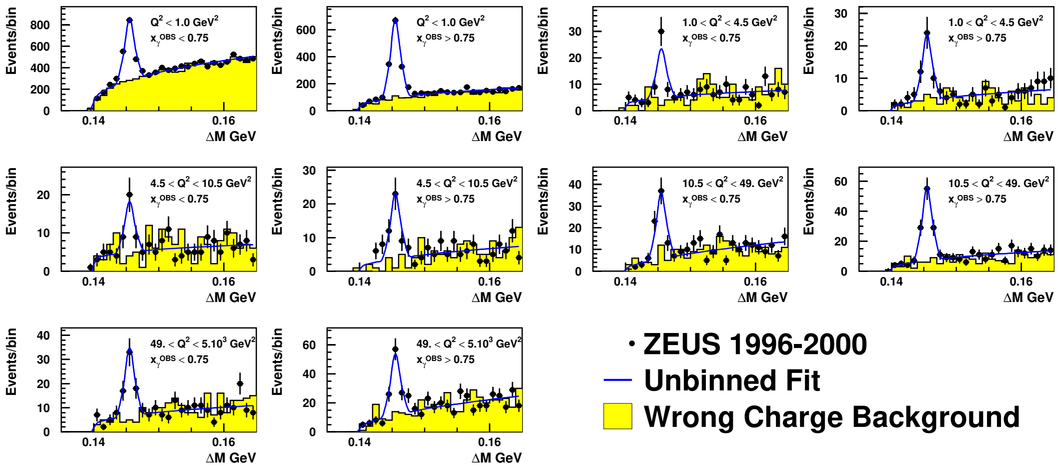

Figure 4.4: *Signals for the 1996-2000 data, the line shows the result of an unbinned fit to the signal and the histogram the wrong charge background estimate.*

on the pseudorapidity of the D^* requires that it and, as a result, the tracks used to form it, lay within a well understood region of the CTD. The p_T cut reduces the combinatorial background, which is much higher at lower p_T, while retaining an acceptable event sample.

4.4 Background Estimation

A clean signal would produce a Gaussian distribution for the mass difference, $\Delta M = m(D^*) - m(D^0)$. However, since a combinatorial background also passes the cuts the shape is that of a Gaussian plus some background distribution. This background can clearly be seen Figure 4.4 which shows the ΔM distribution for the D^* candidates in the restricted Q^2 and x_γ^{OBS} regions of this analysis. Also shown in the figure are two methods of estimating this background:

- *wrong charge background:* The selection for the wrong charge background is identical to that described in Section 4.3.3 except that the two tracks forming the D^0 candidate are required to have the same charge. This combination cannot come from a D^* since it has a total charge of ± 3. It will, however, have exactly the same kinematic properties as the combinatorial background in the right charge case. Thus, when properly scaled, it can be subtracted from the right charge distributions to give background free estimate.

- *functional fit:* This attempts to describe the signal distribution using a Gaussian for the D^* contribution, together with a threshold function for the background.

As can be seen from Figure 4.4 the statistics for both right and wrong charge combinations are very low in the low-Q^2 DIS distributions. The wrong charge background is thus subject to large statistical fluctuations and cannot provide a reliable estimate in this region. The number of candidates was determined using an unbinned fit to the ΔM distribution with the function:

$$F(\Delta M) = \frac{P1}{\sqrt{2\pi} \cdot \sigma_{\Delta M}} \cdot exp\Big(\frac{(\Delta M - <\Delta M>)^2}{2 \cdot \sigma_{\Delta M}}\Big) + P2 \cdot (\Delta M - m_\pi)^{P3} \tag{4.3}$$

where $\sigma_{\Delta M}$ and $<\Delta M>$ are the width and position of the Gaussian determined from a 5 parameter fit to all the signals in Figure 4.4 combined, m_π is the mass of the pion and P1-P3 are free parameters. The fitted value of $<\Delta M>$ was 145.51 ± 0.03(stat.), which should be compared with the present PDG value of 145.397 ± 0.030. The fitted value of $\sigma(\Delta M)$ was 0.76 ± 0.03 MeV, consistent with that anticipated from the resolution of the CTD.

After all cuts the estimated number of events with a $D^{*\pm}$ was 2200 ± 61 for the PHP sample and 421 ± 25 for the DIS sample.

Chapter 5

Event description and correction

5.1 Monte Carlo simulation

In order to take account of the effects of finite detector resolutions, efficiency and acceptance Monte Carlo techniques were used to correct the data back to the "hadron level", independent of detector effects.

The underlying physics process was simulated using the Monte Carlo event generators PYTHIA 6.1 [52] and HERWIG 6.1 [53], described in detail Sections A.2 and A.1 respectively. Both these programs use LO matrix elements and pQCD to simulate the hard subprocess together with models of non-perturbative phenomena, such as parton density functions and hadronisation, to simulate the event before interaction with the detector. This stage in the simulation is defined as the hadron level.

To simulate the detector response, events from the event generators are processed by the MOZART program which is based upon the GEANT 3.13 [54] package. This simulates the detector response for each component based upon its geometry and material composition and incorporates the current level of understanding of the detector from both physics studies and test beam results. The data acquisition chain and trigger response of the ZEUS detector are simulated by the ZGANA and ZEPHYR packages which generate the trigger response for the simulated component signals and perform the full offline reconstruction taking into consideration all calibration constants and detector state information.

5.1.1 Monte Carlo samples

Two samples of events were generated; a PYTHIA sample, which was used for the correction to hadron level; and a HERWIG sample which was used as a cross-check for the correction. Both samples were generated with the SaS1D and MRSA [55] sets for the photon and proton parton distribution functions respectively. Leading-order resolved (LO-RES) and direct (LO-DIR) processes were generated separately and events with at least one $D^{*\pm} \to D^0\pi_s^{\pm} \to (K^{\mp}\pi^{\pm})\pi_s^{\pm}$, with $p_T(D^*) > 2.5$ GeV and $|\eta(D^*)| < 3.0$ were selected. These events were then processed through the detector simulation as described above.

In order to take account of the different beam and detector configurations in the period 1996-2000, four separate MC subsamples, detailed in Table 5.1, were generated and weighted according to the luminosity of each corresponding data period.

Sample	Lepton beam	Hadron beam	Mozart version
1	27.52 GeV e^+	820 GeV p	1996
2	27.52 GeV e^+	820 GeV p	1997
3	27.52 GeV e^-	920 GeV p	1998
4	27.52 GeV e^+	920 GeV p	1999

Table 5.1: *Generated MC subsamples.*

The normalisations of the LO-DIR and LO-RES processes are not known *a priori* and must be extracted from the data for each Q^2 region. The fraction of resolved events, α, was extracted using a single parameter χ^2 fit of the combined Monte Carlo sample to the uncorrected $x_\gamma^{\rm obs}$ distribution from the data. The Monte Carlo samples were combined according to

$$N_i = \alpha \cdot N_i^R + (1-\alpha) \cdot N_i^D$$

where N_i is the number of MC events in bin i, and N_i^R and N_i^D are the number of events from the resolved and direct samples respectively, each being individually normalised to contain the same number of events as the data. Because of the low statistics in the DIS sample the $x_\gamma^{\rm obs}$ distribution could only be split into two bins. The resulting normalisations from these fits are shown in Table 5.2.

5.2 Comparison of data and Monte Carlo

In order to use the Monte Carlo sample to correct for detector effects, it must describe the data reasonably well throughout a large region of its parameter space. In

	PYTHIA		HERWIG	
(GeV^2)	LO-DIR	LO-RES	LO-DIR	LO-RES
$0.0 < Q^2 < 1.0$	1.33	0.84	2.57	1.71
$1.0 < Q^2 < 4.5$	1.25	0.80	2.32	2.40
$4.5 < Q^2 < 10.5$	0.98	0.56	2.06	1.37
$10.5 < Q^2 < 49.0$	1.21	1.22	2.26	1.32
$49.0 < Q^2 < 5000.$	2.30	3.10	1.26	6.76

Table 5.2: *LO-DIR and LO-RES normalisations for PYTHIA and HERWIG.*

particular, the kinematic variables used to define the data sample must be reasonably well modeled, in order that no systematic bias is introduced into the extraction of the cross section. Having reweighted the various subsamples the predictions of the PYTHIA sample used for the correction are now compared to the background subtracted data distributions.

Figure 5.1 shows the $x_\gamma^{\rm obs}$ distributions for PHP and DIS events. As can be seen the description is reasonable in all eight bins, even though the direct/resolved reweight factors were extracted from fits to two bin $x_\gamma^{\rm obs}$ distributions.

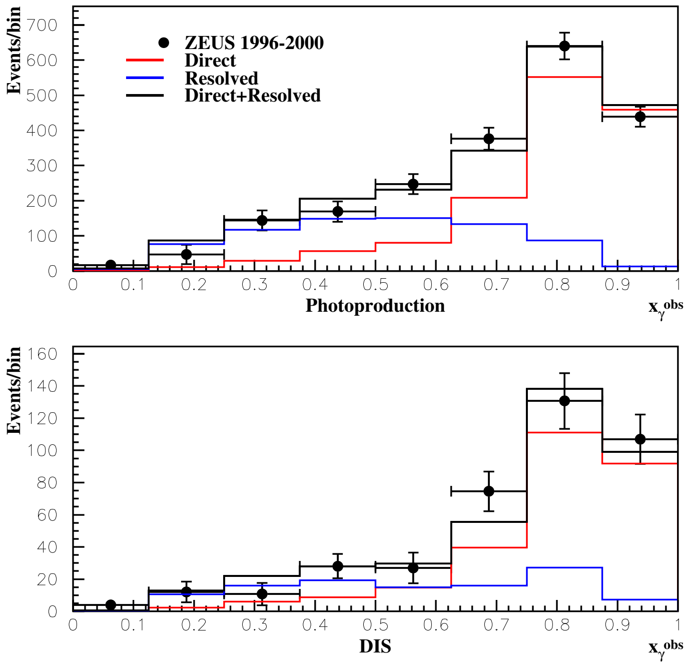

Figure 5.1: *Comparison of data (points) and PYTHIA Monte Carlo (histogram) $x_\gamma^{\rm obs}$ distributions in PHP and DIS events.*

In Figure 5.2 the important quantities in the analysis are compared to the reweighted PYTHIA sample. All the distributions are well described by the Monte Carlo.

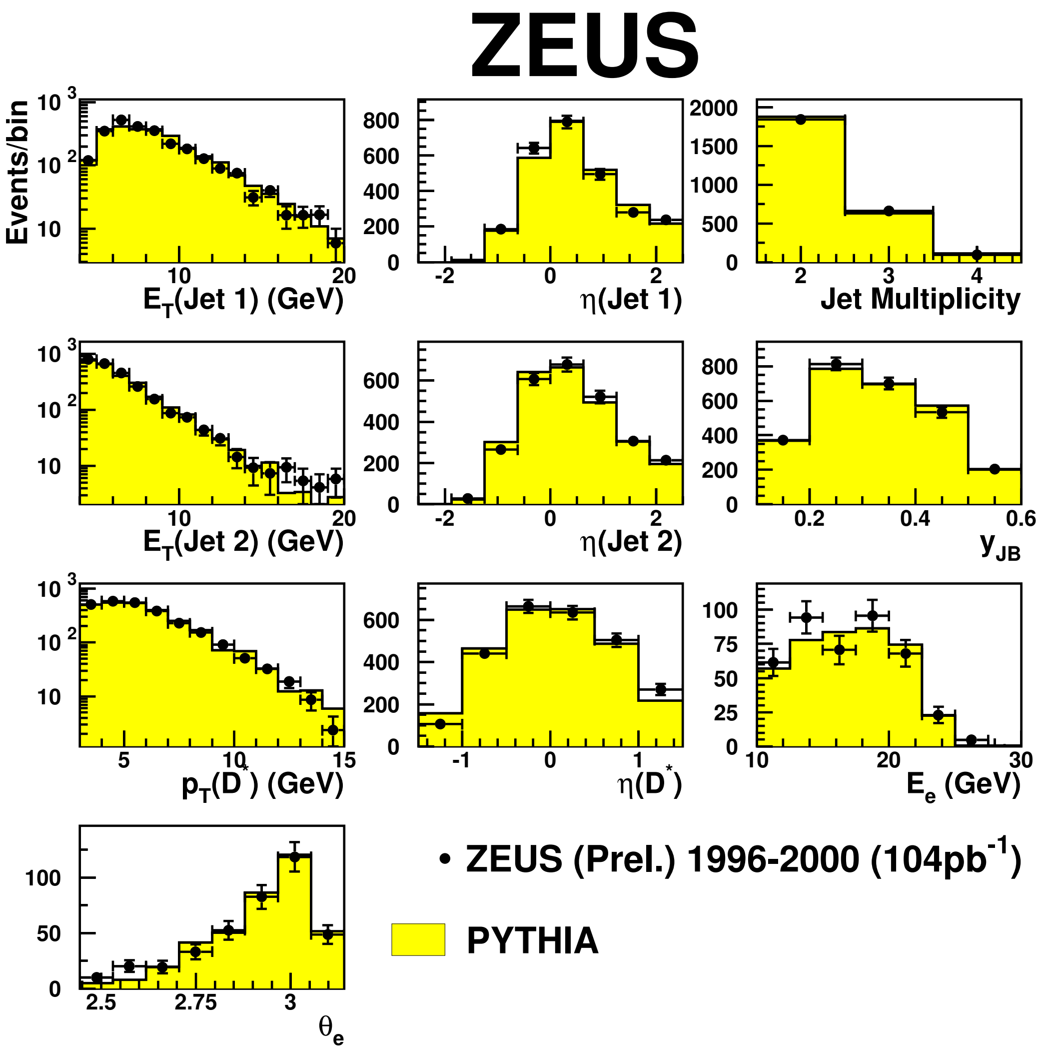

Figure 5.2: *Comparison of data (points) and Monte Carlo (histogram) for event, jet and D^* properties of the events entering the cross section measurement.*

The transverse energy of the second highest E_T jet falls logarithmically whereas the highest E_T jet exhibits a turn over at about 7 GeV after which it also falls logarithmically. This is well modeled by the Monte Carlo. The pseudorapidity of the two highest E_T jets are also well modeled.

Both event properties y_{JB} and N_{jet} are well described by the Monte Carlo.

The transverse momentum of the D^* exhibits a turn over between 4 and 5 GeV. This occurs because the D^* is often associated with a jet, thus the E_T requirement on the jet feeds through into the $p_T(D^*)$ distribution. This effect is reasonably well described by the Monte Carlo. The pseudorapidity of the D^* in data exhibits a small excess over the Monte Carlo prediction in the forward region but overall is again well described by the Monte Carlo.

The agreement between data and Monte Carlo is less good for the electron energy, however this appears more likely to be due to statistical fluctuations in the data than poor description by the Monte Carlo. The electron polar angle shows a small disagreement in one bin but again the overall description is reasonable.

Having demonstrated that the Monte Carlo gives an acceptable description of the data it can now be used to correct the data for detector effects.

5.3 Acceptance correction

The uncorrected data were unfolded back to the hadron level using a bin-by-bin correction procedure. In each x_γ^{obs} and Q^2 bin the purity, p, efficiency, ϵ, and correction factor, C, were calculated. For a given bin, the efficiency and purity are given by

$$\epsilon = \frac{u}{t}, \tag{5.1}$$

and

$$p = \frac{u}{m}, \tag{5.2}$$

where t is the number of events generated in the bin, m is the number of events measured in the bin, and u is the number of events both generated and measured in the bin. Therefore, the efficiency can be thought of as the fraction of generated events in a given bin which were also measured in that bin and the purity as the fraction of events measured in a given bin which were also generated in that bin.

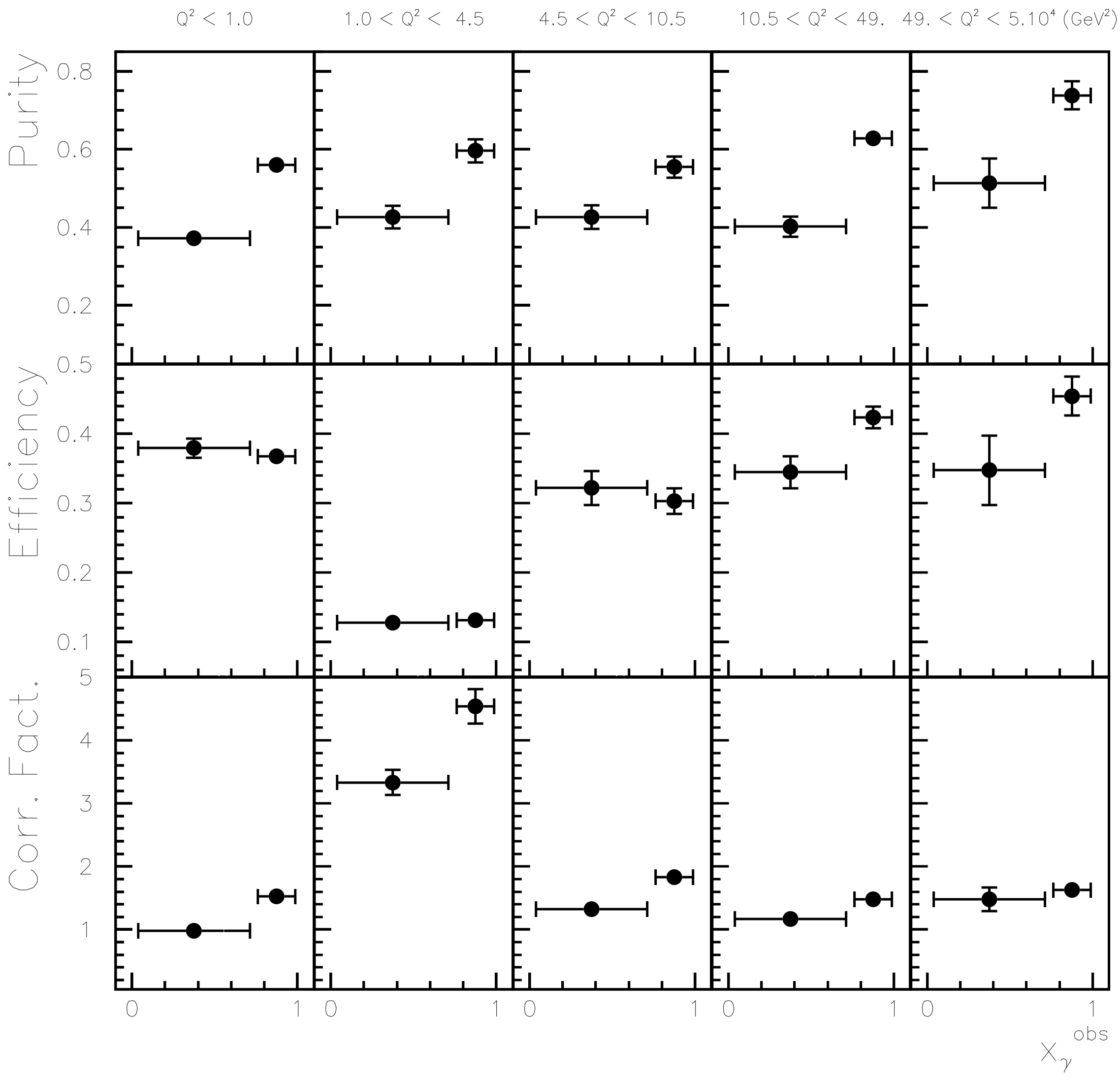

Figure 5.3: *Purity, efficiency and correction factor shown for the unfolding procedure as a function of* x_γ^{obs} *for each* Q^2 *region.*

The correction factor is related to the purity and efficiency by:

$$C = \frac{p}{\epsilon} = \frac{t}{m}. \tag{5.3}$$

The purity, efficiency and correction factor for each of the x_γ^{obs} and Q^2 bins in this analysis are shown in Figure 5.3. The errors used for these expressions are given in Equations (B.1-B.2), and derived in Appendix B.

The purity rises with x_γ^{obs} . Events at high x_γ^{obs} are predominantly from direct processes which are purer due to the jets being harder and consequently more likely to pass the E_T^{jet} cuts. The efficiency is much lower in the $1.0 < Q^2 < 4.5$ GeV^2

bins. This is a result of the reduced detector acceptance close to the rear beampipe where the impact point of the electron is for low-Q^2 events.

The differential cross section, σ, is then calculated from the number of events passing the selection cuts after background subtraction, N, for a given integrated luminosity, $\int \mathcal{L}dt$, such that;

$$\sigma(i) = \frac{N \cdot C}{\int dt\mathcal{L} \cdot \text{bin width} \cdot \text{BR}} \tag{5.4}$$

where BR is the branching ratio for the process $D^* \to K\pi\pi_S$, $(2.609\pm0.098)\%$ [56], and $\int \mathcal{L}dt$ is the integrated luminosity $103.7\,\text{pb}^{-1}$.

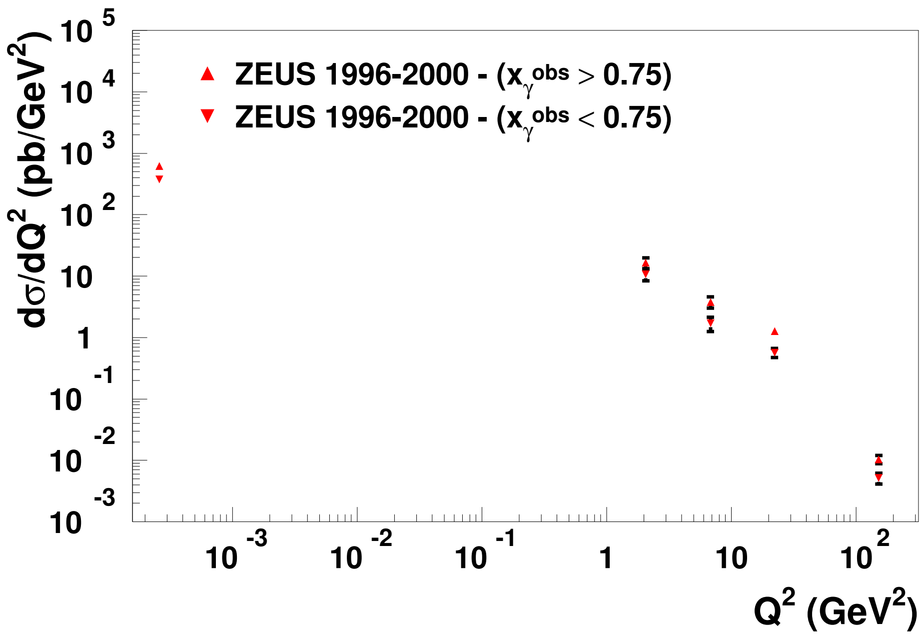

Figure 5.4: *Low and high x_γ^{obs} cross sections for events with a D^* as a function of Q^2. Errors are statistical only.*

The corrected cross sections are shown in Figure 5.4. It is clear that the low x_γ^{obs} cross section lies below the high x_γ^{obs} across the whole Q^2 range. However, it does not appear to fall at as great a relative rate as has been observed in analyses which did not require the presence of a D^*. In order to study the sensitivity of these cross sections to the suppression of photon structure like effects with Q^2 it is useful to form the ratio of low to high x_γ^{obs} cross sections, shown in Figure 5.5.

This has several advantages; the high-x_γ^{obs} cross section is subject to the same kinematic factors as the low-x_γ^{obs} and as such dividing by it should cancel out these

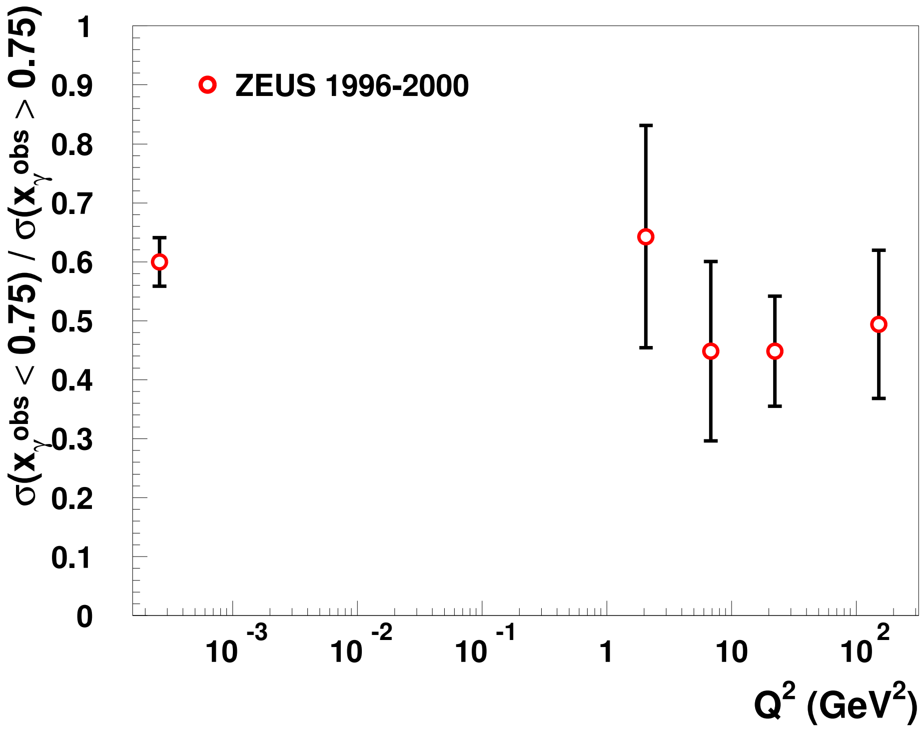

Figure 5.5: *Ratio of low to high* $x_\gamma^{\rm obs}$ *cross sections for events with a* D^* *as a function of* Q^2. *Errors are statistical only.*

factors enabling us to study $x_\gamma^{\rm obs}$ dependent effects in isolation; many sources of systematic uncertainty will affect the low- and high-$x_\gamma^{\rm obs}$ cross sections in the same way and will cancel out in the ratio.

5.4 Study of systematic uncertainties on the ratio

In order to estimate the sensitivity of the measured cross section ratio to potential sources of systematic uncertainty, several checks have been performed. These have been split into three separate groups for convenience.

5.4.1 Uncertainties arising from calorimeter quantities

The effect on the cross section ratio of varying the calorimeter cuts can be seen in Figure 5.6. The points are the systematic change in the ratio divided by the nominal value for the ratio for each bin, increasing in Q^2 from left to right. The shaded band represents the statistical error for each bin. The cuts on the jet E_T and η, $y_{\rm JB}$ and electron energy E'_e have all been varied by $\pm1\sigma$ from the nominal values, where the resolution σ has been estimated from the Monte Carlo. In addition the

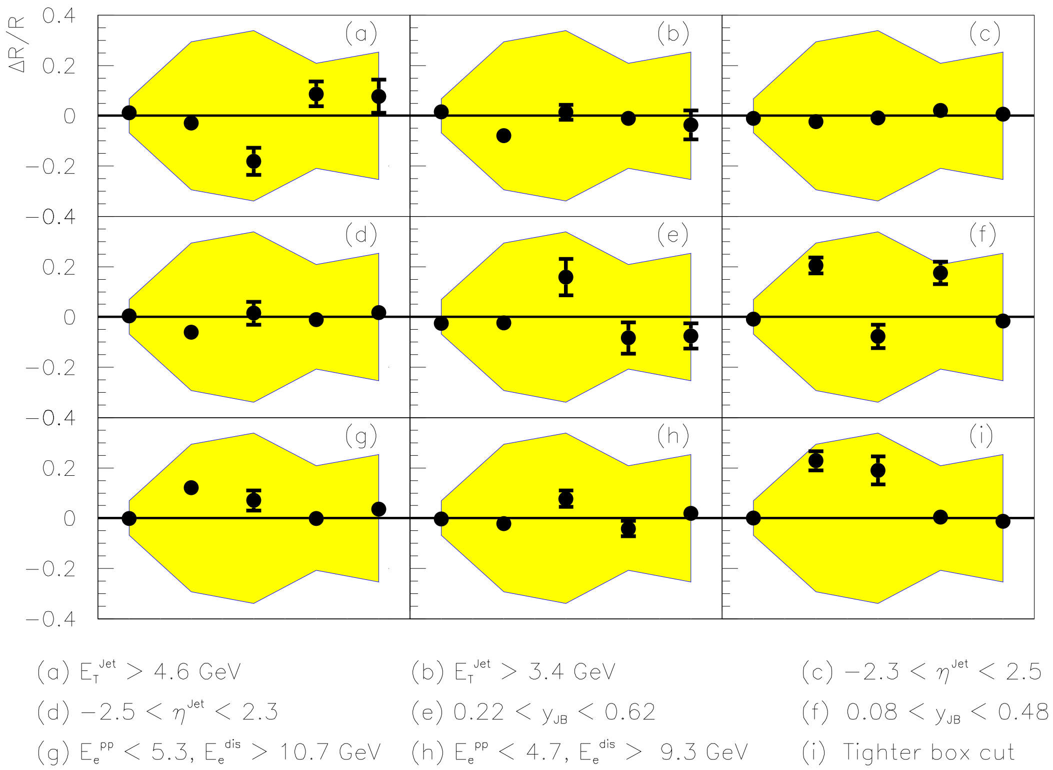

Figure 5.6: *Systematic uncertainties due to the kinematic cuts as a function of $x_\gamma^{\rm obs}$. The shaded band shows the statistical error on the central ratio value.*

box cut, described in Section 4.3 was widened by 1 cm, the position resolution of the calorimeter.

All the systematic variations are well within the statistical error. The dominant variations are due to the jet E_T and $y_{\rm JB}$ cuts. The variation due to the tighter box cut is also significant for the two lowest Q^2 DIS bins, when the electron is close to the rear beampipe.

5.4.2 Uncertainties arising from tracking quantities

The effect on the cross section ratio of varying the tracking cuts can be seen in Figure 5.7. The cuts on the p_T of the D^*'s candidate tracks have all been varied by ± 10 MeV. This is roughly twice the CTD resolution [3] at the K and π cut values and the actual resolution at the π_s cut. The systematic variation is small for all these changes. In order to estimate the stability of the unbinned fits the D^0 mass window was widened by 20 MeV, allowing a greater fraction of background events to enter into the fit. The mean and width of the Gaussian function in Equation (4.3) were also varied by $\pm 1\sigma$ of the values given in Section 4.4 to estimate the effect of

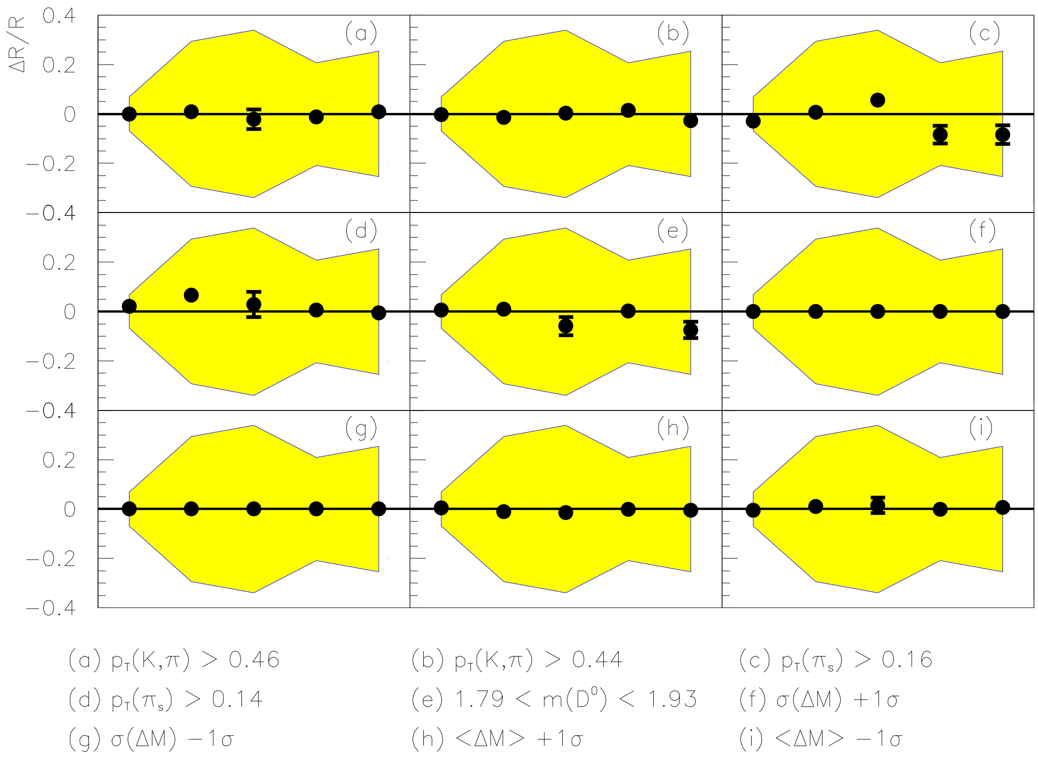

Figure 5.7: *Systematic uncertainties due to the D^* as a function of $x_\gamma^{\rm obs}$. The shaded band shows the statistical error on the central ratio value.*

using the same values for all the signal distributions. The systematic variation is, again, small for all these changes.

5.4.3 Uncertainties arising from the Monte Carlo description

The effect on the cross section ratio of varying the Monte Carlo can be seen in Figure 5.8. The dependence on the Monte Carlo used is estimated by using the HERWIG sample to correct for detector effects. The systematic variation is large but still within the statistical uncertainty.

In order to estimate the uncertainty introduced by reweighting the direct and resolved samples the reweight factors, given in Table 5.2, were varied by $\pm 1\sigma$, where σ is the error on fit parameters returned by Minuit. This has the effect expected of systematically reducing the cross section ratio when the direct has an increased weight and raising it when it has a decreased weight. The large change in the DIS bins occurs because the errors on the fit parameters for these bins are fairly large, up to 30%, reflecting the low statistics in these bins.

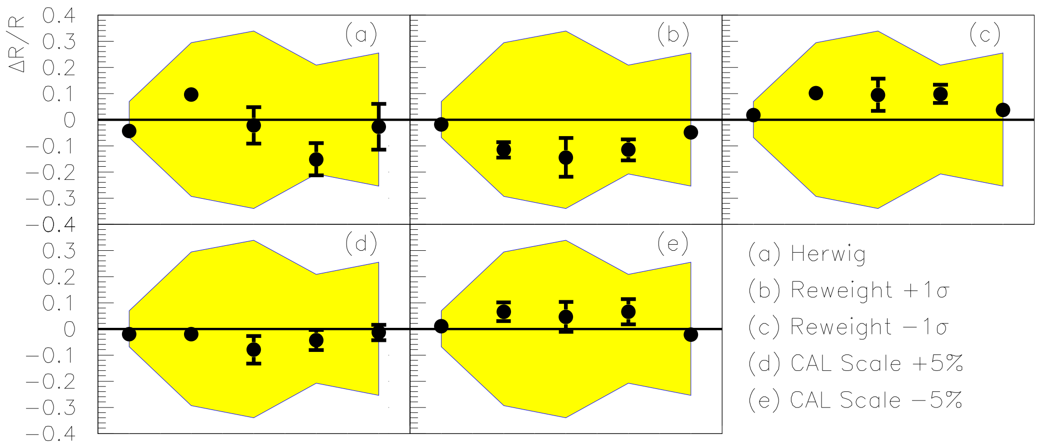

Figure 5.8: *Systematic Uncertainties due to the Monte Carlo as a function of* x_γ^{obs} *. The shaded band shows the statistical error on the central ratio value.*

There is an uncertainty in the knowledge of the CAL energy scale between data and Monte Carlo [57] which is at most ±5%. To take account of this the calorimeter quantities, y_{JB} and E_T^{jet} were scaled by ±5% in Monte Carlo only. The variation is less than 10% for all analysis bins.

5.4.4 Initial state radiation

Initial state radiation (ISR) of a photon from the incoming lepton before it interacts with the proton will affect measurements of Q^2 and y. Typically such a photon travels collinear with the lepton beam and effectively reduces the initial lepton beam energy to be less than 27.5 GeV. Neither the PYTHIA nor the HERWIG Monte Carlo includes the effects of ISR. However, the effect of ISR has been estimated in a similar analysis [58] using the DJANGOH program which combines a DIS Monte Carlo generator with a simulation of radiative effects.

The mean ISR photon energy was determined to be 1.8 GeV which translates into an effective reduction in lepton beam energy from 27.5 to 25.7 GeV. The effect on Q^2 and y is given by:

$$\frac{\Delta Q_e^2}{Q_e^2} = \frac{E_\gamma^{ISR}}{E_e},$$

and

$$\Delta y_e = \frac{E_\gamma^{ISR}}{E_\gamma^{ISR} - E_e} \cdot (1 - y_e),$$

Where E_e is the lepton beam energy and E_γ^{ISR} the energy of the ISR photon. Inserting 1.8 GeV for E_γ^{ISR} and 0.2 for y to obtain the maximal effect, the fractional change in Q^2 is approximately 6.5%, and the absolute change in y is approximately 5.5%. These values are almost equal to the width of the resolution on these variables, as simulated by a Monte Carlo without ISR.

Since x_γ^{obs} is unaffected by ISR, and the Q^2 bins are significantly larger than the resolution, the data are not corrected for this effect and it is not included in the systematic uncertainty.

Chapter 6

Results and Discussion

6.1 Comparison to LO pQCD predictions

The cross section ratio $R = \sigma(x_\gamma^{\mathrm{OBS}} < 0.75)/\sigma(x_\gamma^{\mathrm{OBS}} \geq 0.75)$ as a function of Q^2 is shown in Figure 6.1. The data points are positioned at the median Q^2 value of each bin, as determined from the Monte Carlo used for the correction. The inner error bars are the statistical errors, and the outer error bars are the statistical and systematic errors added in quadrature. Within the errors, the cross section ratio is consistent with being constant as a function of Q^2.

The ratio is compared to several LO pQCD predictions in Figure 6.1. The upper plot shows two predictions from the HERWIG Monte Carlo using the SaS1D PDF. This structure function is provided by the same authors who proposed the suppression scheme described in Section 2.4 and is shown with and without this Q^2 suppression included. The prediction without suppression serves as a check that any suppression with Q^2 has a physical origin rather than being due to some kinematic bias. The prediction is constant as a function of Q^2, confirming that no such bias exists. The prediction including suppression shows the expected fall with increasing Q^2. Unfortunately the statistical errors are large enough such that neither prediction is clearly preferred.

In the lower plot of Figure 6.1, the same data are compared to two predictions which implement no specific partonic structure for the photon, generating all low x_γ^{obs} events from parton showers in two different schemes. The AROMA model, which implements the DGLAP evolution scheme, lies below the data. The CASCADE model, which implements a version of the CCFM evolution scheme, is much closer to the data.

Thus, in order to describe the ratio using LO pQCD it appears to be necessary either to introduce a virtual photon structure to DGLAP evolution or to use CCFM

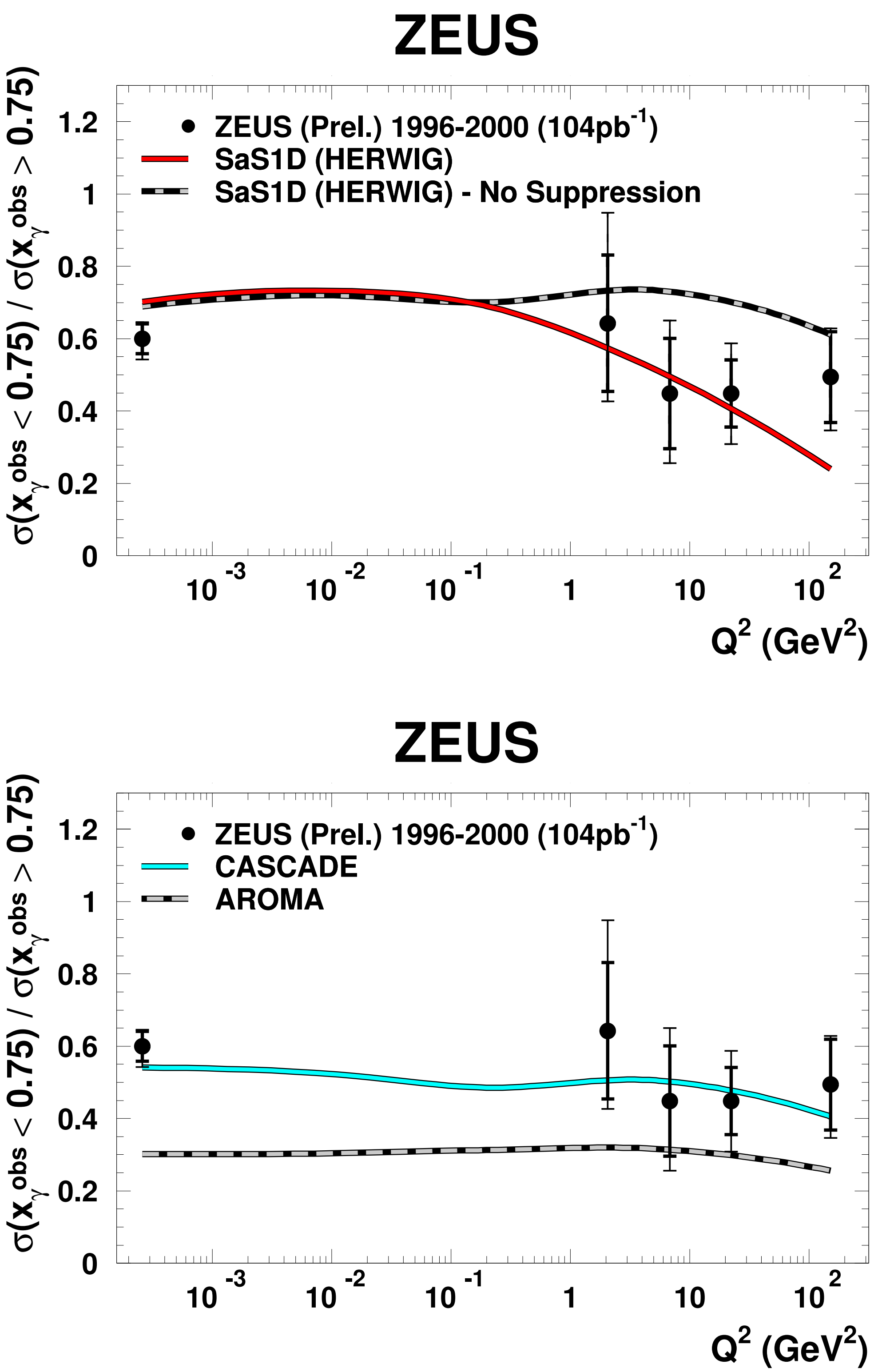

Figure 6.1: *Ratio of low to high $x_\gamma^{\rm obs}$ cross sections for events with a D^* compared to the LO pQCD predictions of HERWIG using the SaS1D PDF (upper), and AROMA and CASCADE (lower).*

evolution. The difference between these two approaches is not, however, as great as it might at first appear, since:

- While the SaS1D structure function and suppression scheme does contain both VMD and anomalous components, the VMD part makes almost no contribution in the kinematic region of this measurement.
- The k_T factorisation in CASCADE already includes the anomalous component [59].

The difference between these models is then purely a question of factorisation. In the SaS1D/DGLAP approach, the anomalous photon is factorised into the soft photon structure function. Whereas, in the CASCADE/CCFM approach, the anomalous photon is factorised into the evolution of the hard process. In both cases it is dealt with perturbatively. However, the predicted dependence of the ratio with Q^2 does differ significantly between these two approaches. The estimated $1\,\text{fb}^{-1}$ which HERA is expected to deliver by 2005 would greatly increase the power of this measurement to distinguish between these two approaches.

6.2 Implications for $F_2^{c\bar{c}}$

The results presented here suggest that, in the restricted kinematic region of this analysis, an anomalous photon contribution is necessary to describe the production of D^*s in DIS (at least at LO). In Section 2.5, the D^* cross section in DIS was compared to the prediction of a massive NLO calculation of the BGF process. This did not describe the shape of the D^* distributions, particularly in the forward region. This is the same region in which massive NLO calculations failed to describe the photoproduction cross section. These same massless calculations described the high x_γ^{obs} cross section but underestimated the low x_γ^{obs} cross section. Taken together, these results also seem to suggest that some additional, low x_γ^{obs} , contribution may be necessary in DIS.

In the measurement of $F_2^{c\bar{c}}$ described in Section 2.5, the extrapolation to the full D^* phase space assumed that only BGF processes contribute to D^* production in DIS. The D^* discrepancy was interpreted as being due to the Peterson fragmentation used in the NLO calculation, which assumes that $\eta(D^*) \equiv \eta(c)$. In order to simulate hadronisation effects, the NLO prediction was reweighted using a correction factor derived from the LO Monte Carlo RAPGAP [60]. However, using a correction factor from a LO MC including parton showers in an NLO calculation could result in the double counting of gluon radiation. A better solution would be a Monte Carlo that predicts both the correct absolute cross sections in y and Q^2, as for NLO DGLAP, and the shape of the D^* distributions, as for LO DGLAP with parton showers.

One potential candidate is the CCFM Monte Carlo CASCADE, which has been shown, in this thesis, to give a reasonable description of the production of D^*s with two or more jets in DIS. This has been used by the H1 collaboration in their most recent $F_2^{c\bar{c}}$ measurement [61] where it was found to be in better agreement with the data than the predictions of NLO DGLAP.

6.3 Comparison to ratio without a D^* tag

The fact that the ratio does not change significantly with Q^2 in this range is in marked contrast to the previous results that did not require a $D^{*\pm}$ tag, discussed in Section 2.4.1. This suggests that the suppressions of the low $x_\gamma^{\rm obs}$ cross section due to charm and due to photon virtuality are not independent. In order to quantify this, the ratio should be compared to this "all flavours" measurement. Unfortunately, a direct comparison cannot be made due to differences in the kinematic regions of the two analyses[1].

In Section 2.4.1, it was shown that the SaS1D virtual photon PDF described the shape but not the normalisation of the all flavours ratio, requiring a normalisation factor of 1.3. The obvious physical interpretation of this normalisation is that there is an increased resolved component, independent of Q^2. If this was the case the ratio could be described by simply reweighting the resolved contribution, however, this will also change the shape of the ratio. This is clear when you consider the ratio in terms of its direct and resolved components:

$$R = \frac{\sigma^{DIR}(x_\gamma^{\rm obs} < 0.75) + \sigma^{RES}(x_\gamma^{\rm obs} < 0.75)}{\sigma^{DIR}(x_\gamma^{\rm obs} > 0.75) + \sigma^{RES}(x_\gamma^{\rm obs} > 0.75)}. \tag{6.1}$$

At high Q^2, where the resolved contribution is negligible, the ratio would be unchanged, whereas at low Q^2,where the resolved contribution is significant, the ratio would be scaled up, spoiling the description of the shape. The interpretation must then be some low $x_\gamma^{\rm obs}$ contribution that is identical for direct and resolved events and independent of Q^2. In order to estimate the normalisation required in the kinematic region of this analysis, the all flavours ratio was measured for

[1]The all flavours measurements were made in a more restricted y and η^{jet} region.

$Q^2 < 1.0$ GeV^2 using the 1996 data. The required normalisation was found to be ≈ 1.7.

Since it is the difference in shape of this ratio and the one presented here that is of interest, the prediction of the SaS1D structure function can be used to estimate the all flavours ratio in the kinematic region of this analysis.

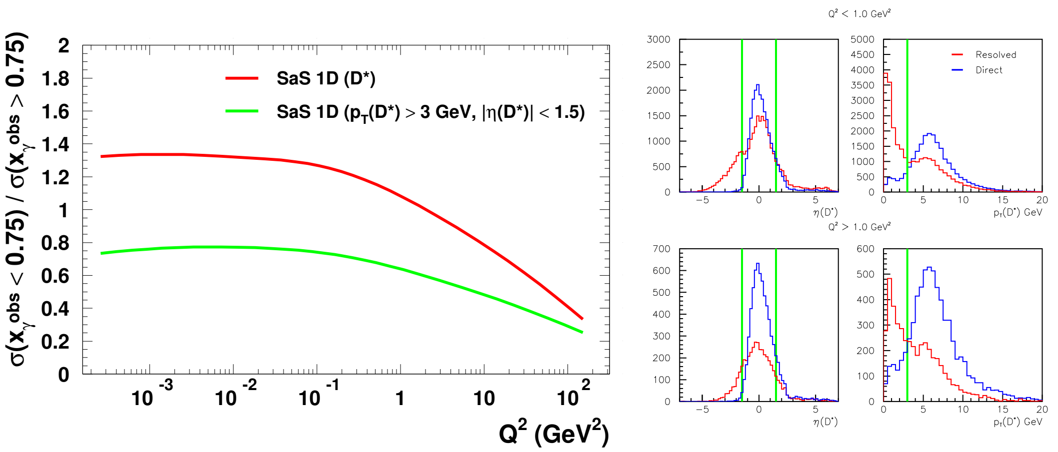

Figure 6.2: *Predicted ratio of low to high $x_\gamma^{\rm obs}$ for events containing a D^*, with and without D^* cuts (left) for HERWIG/SaS 1D. Monte Carlo hadron level $p_T(D^*)$ and $\eta(D^*)$ distributions predicted by HERWIG/SaS 1D for events passing all other hadron level cuts (right).*

Before comparing to the all flavours ratio predicted by SaS1D, any bias due to the D^* kinematic cuts must first be evaluated. Figure 6.2 shows the ratio predicted by SaS1D for all events with a D^*, and for events with a D^* which passes the kinematic cuts of this analysis. The D^* kinematic cuts are clearly seen to cause a Q^2 dependent suppression, in addition to any suppression due to the presence of charm.

The physical origin of this bias can be seen in the right hand side plot of Figure 6.2, which shows the $p_T(D^*)$ and $\eta(D^*)$ distributions for direct and resolved MC samples. In both the PHP and DIS regions the direct $\eta(D^*)$ distribution is almost entirely within the cut region $|\eta(D^*)| < 1.5$. The $p_T(D^*)$ distribution is peaked at around 6-7 GeV, well above the cut $p_T(D^*) > 3.0$ GeV, and consistent with the D^* being in a jet with $E_T^{jet} > 6.5$ GeV. The resolved $p_T(D^*)$ distribution appears, however, to be the sum of two distributions, one peaked in the same place as the LO direct distribution and the other at very low values of $p_T(D^*)$. At higher Q^2, this low $p_T(D^*)$ peak is smeared to higher values.

This difference between direct and resolved distributions can be understood by considering the LO processes which contribute to dijet production, shown in

Figure 2.7[2]. The dominant direct process is BGF, Figure 2.7(b), which results in two charm jets in the final state. The dominant resolved process is charm excitation from the photon, Figures 2.7(e) and (f), which results in one charm and one gluon jet, the other charm quark remaining in the photon remnant. Since the photon remnant carries on in a similar direction to the incident photon, this charm quark will, in general, fail the D^* cuts (being at low p_T and η). At higher values of Q^2, where the incident photon is not collinear to the electron beam, it becomes more likely that the D^* will pass the kinematic cuts. The effect of extrapolating the ratio to the full D^* kinematic range has been estimated using the HERWIG MC.

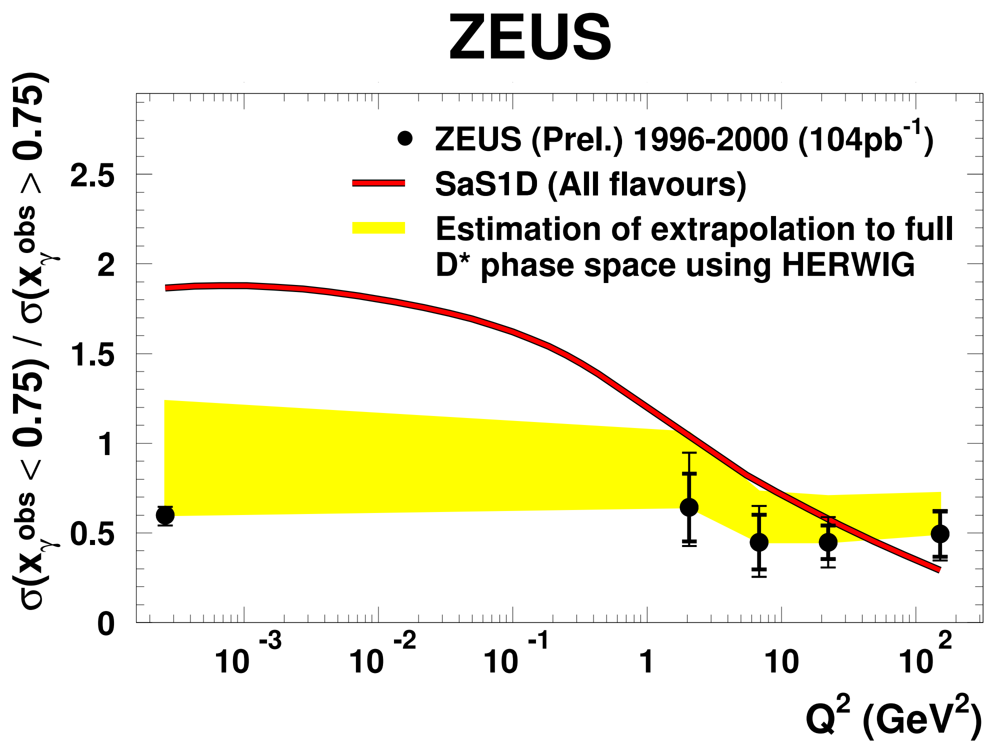

Figure 6.3: *Ratio of low to high x_γ^{OBS} for events with a D^* compared to the predictions of the SaS1D photon structure function for the ratio without a D^* tag. The upper edge of the band represents the expected ratio for the full D^* phase space.*

The effect of this extrapolation and the comparison to the all flavours prediction is shown in Figure 6.3. This confirms quantitatively the qualitative conclusion drawn above. The ratio of the low x_γ^{OBS} cross section to the high x_γ^{OBS} contribution falls off much slower in the presence of charm than it does when charm is not required. This demonstrates for the first time that the observed suppressions of the low x_γ^{OBS} cross section due to non-zero photon virtuality and due to charm are not independent.

[2]Page 40.

6.4 Jet production in DIS and the γ^*p frame

In jet production, the transverse energy of the jets, relative to the direction of the incoming partons, reflects the hardness of the interaction. In photoproduction, since the photon is collinear to the electron beam, only a longitudinal boost is necessary to go from the LAB frame to the parton-parton frame. Since both E_T and differences in η are invariant under longitudinal boosts, jets found in the LAB frame are the same as those found in the parton-parton frame (neglecting some constant factor in η). In DIS, the electron is scattered through a significant angle, introducing a transverse boost and E_T measured in the LAB frame is no longer the same as it is in the parton-parton frame. Since the scattered electron is well reconstructed, it is possible to boost into γ^*p frame, in which the photon and proton are again collinear.

Clearly this difference in E_T between frames has the potential to conceal the true physics if measurements are made in the LAB frame, as was done in this thesis. Unfortunately, since there is no measured scattered electron in photoproduction, this boost can only be done for the DIS ratio points. In addition, the kinematic cuts on the jets and the D^* would have to be modified. In general the LAB frame cuts are motivated by the detector acceptance, $|\eta(D^*)| < 1.5$ corresponds to the region in which the three decay products can be accurately reconstructed and the minimum $p_T(D^*)$ is correlated to minimum momentum with which the π_s can be reliably reconstructed. In the γ^*p frame these acceptances will be smeared due to the boost and, in general, tighter cuts will have to be chosen to ensure the measurement is made in a well understood region of the detector. This could result in an unacceptable loss of statistics.

One possibility would be to perform the transverse boost only. This could allow the photoproduction point to be retained, since it has no transverse component. In addition,since the smearing of the detector acceptance is predominantly due to the longitudinal boost, cuts similar to the current detector motivated cuts could be used, minimising the loss of statistics.

Having explained the reasons for performing this analysis in the LAB frame and highlighted some of the dangers, it is of interest to see how the predicted ratio changes between the two frames. Figure 6.4 shows the ratio predicted by HERWIG using the SaS1D PDF in both frames. The mean change in η between frames is ~ 1.8 and the η cuts have been offset by this value so that the two predictions correspond to approximately the same kinematic range. No attempt has been made to quantify the changes in E_T, which appears to be slightly harder in the γ^*p frame. The ratio is lower in the γ^*p frame, as would be expected if the jets were on average harder,

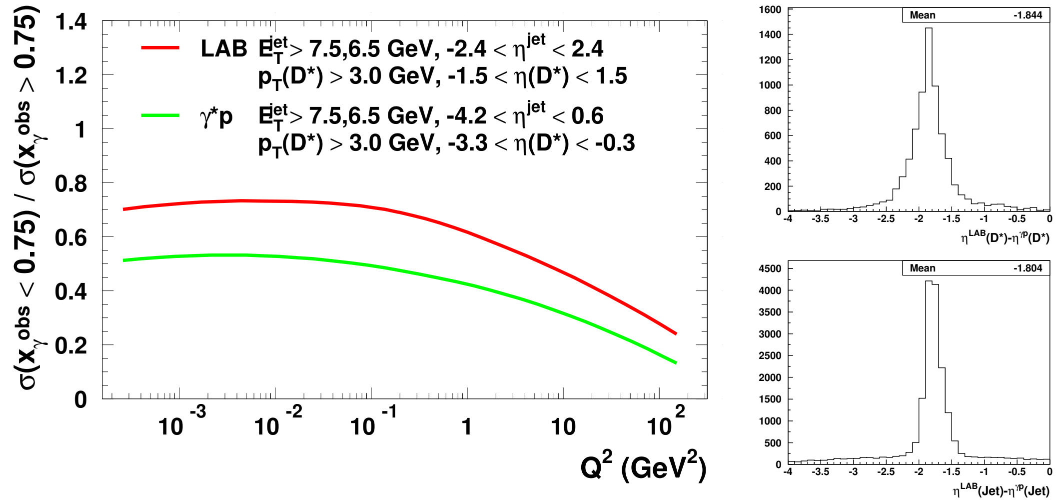

Figure 6.4: *Ratio of low to high* x_γ^{obs} *for events containing a* D^* *in the LAB and* γ^*p *frames (left). Change in* $\eta(D^*)$ *and* η^{jet} *when boosting to the* γ^*p *frame (right).*

however the shape is unchanged and it can be expected that the same physics conclusions would be drawn if the analysis was repeated in the γ^*p frame. This would be consistent with the all flavours measurement using the 1996-1997 data, which was initially performed in the LAB frame in [58] with the same conclusions as the current measurements in the γ^*p frame, discussed in Section 2.4.1.

After all this discussion, it should be emphasised that throughout this thesis like has been compared with like, i.e. both the measurement and predictions were performed in the LAB frame. It is only the interpretation of E_T as the hard scale which is dependent on the frame in which the measurement and predictions are made.

Part II

A global tracking trigger for ZEUS

Chapter 7

The upgrades to HERA and the ZEUS detector

7.1 Introduction

The HERA *ep* storage ring began delivering luminosity in June 1992, delivering an integrated luminosity of $33\,\mathrm{nb}^{-1}$ in that year. The delivered luminosity has steadily increased with $67\,\mathrm{pb}^{-1}$ delivered in 2000, giving a total integrated luminosity of $120\,\mathrm{pb}^{-1}$. The experiments H1 and ZEUS have made good use of this luminosity and [8, 62] provide reviews of the physics studied at HERA to date. Important results so far have included:

- the measurement of F_2, the proton structure function, over six orders of magnitude in both x and Q^2;
- the observation of large rapidity gap events, typical of diffractive scattering;
- the measurement of the strong coupling constant from studies of the hadronic final state in DIS;
- the best limits on contact interactions, leptoquarks and R parity violating SUSY;
- the first measurement of the photoproduction of hard jets and the observation of both real and virtual photon structure effects using x_γ^{obs}.

Two key areas, electroweak and heavy flavours physics, are, however, yet to be studied in detail, motivating the running of HERA till 2005 and the upgrades to both HERA and ZEUS described in this chapter. Both areas will benefit significantly from these upgrades, in particular heavy quarks will be produced at a much greater rate and, as a result of the improved tracking, be measurable using new tagging methods and over a larger region of phase space. A sample of heavy flavour measurements of interest are mentioned here:

- *Charm in photoproduction:* The photoproduction of charm jets provides measurements of the gluon density of the proton (through direct photoproduction) and the parton content of the photon (through resolved photoproduction) [37]. Detailed studies of the resolved contribution to D^* photoproduction, through angular distributions [63], are at present limited by statistics.
- *Charm in DIS ($F_2^{c\bar{c}}$):* The measurement of charm in DIS allows an independent determination of the gluon density of the proton [36]. The extended angular coverage of the MVD will allow D^*'s of much lower p_T to be tagged, reducing the uncertainty in the extrapolation of $F_2^{c\bar{c}}$.
- *Charm in the transition from photoproduction to DIS:* The measurement presented in this thesis would gain from both new tagging methods and the increased luminosity, allowing more definite conclusions to be drawn about the applicability of DGLAP and CCFM evolution in the production of heavy quarks.
- *Beauty in photoproduction:* Measurements of the total beauty cross section at both HERA and TEVATRON are significantly above the predictions of NLO [64, 65]. Cleaner methods of tagging beauty and improved statistics will hopefully allow this difference to be studied in detail.

A full review of physics after the upgrade can be found in [66].

7.2 HERA

The HERA accelerator upgrade is described in detail elsewhere [67], only a brief summary is given here. The upgrade began in September 2000 with the goal of increasing the luminosity four- to five-fold, providing a total luminosity of $1\,\mathrm{fb}^{-1}$ by 2005. In order to achieve this the interaction region has been completely redesigned to achieve an earlier separation of the two beams, close to the interaction point (IP). This has been achieved using combined-function superconducting magnets installed inside the experimental detectors. As a result the final focus of the proton beam has been moved from 26 m to 11 m from the IP allowing it to be focused more strongly.

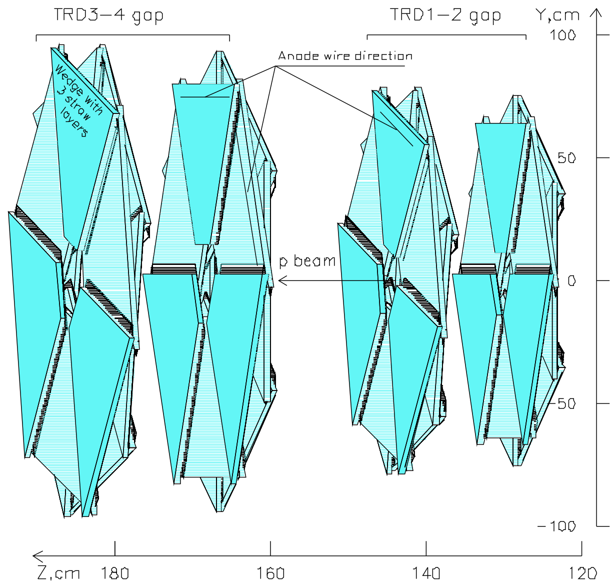

Figure 7.1: *An exploded view of the Straw Tube Tracker.*

7.3 Straw Tube Tracker (STT)

The STT [68] is designed to significantly improve the track finding efficiency in the forward direction by providing a robust starting point for the pattern recognition. At present the pattern recognition is limited by the high occupancy in the forward region which often results in more than one track passing through a Forward Tracking Detector (FTD) cell. The large number of straws in the STT, 11040 in total, will result in a much lower occupancy allowing STT tracks to aid the FTD pattern recognition.

The STT physically replaces the previous Transition Radiation Detector (TRD). In order to keep costs and disruption at a minimum the STT was designed to use the outer mechanical structure, gas system and read-out electronics of the TRD. The removal of the TRD left two gaps of 20.8 cm length along the beam direction. In order to read out the 11000 STT channels through the TRD's existing 2000 channels a high degree of multiplexing was necessary with six straws being readout by each channel. This has been achieved by introducing a 200 ns delay between straw signals.

The STT consists of straw drift tube layers grouped into wedge shaped sectors. The sectors are grouped into four superlayers, with two superlayers in each gap, shown in Figure 7.1, covering the polar angle range $5° – 25°$. A superlayer contains two planes, each plane being composed of six sectors covering the full azimuthal angle. A sector contains 194 or 266 straws arranged into three layers, as shown in Figure 7.2.

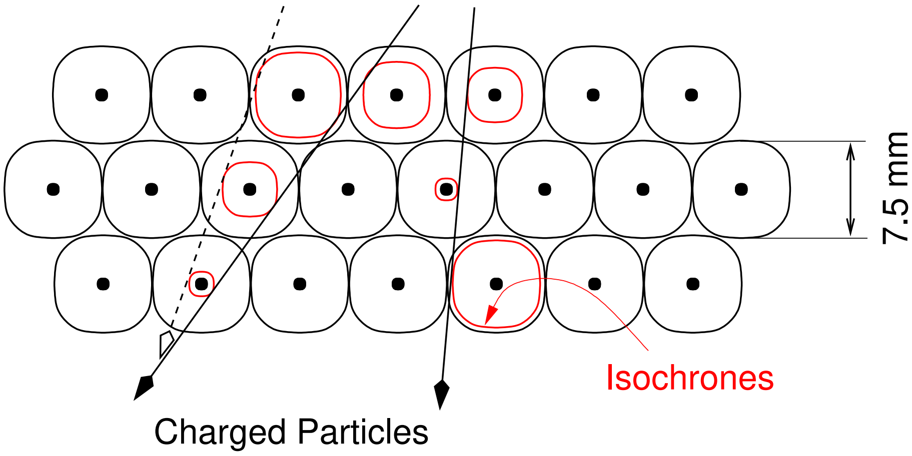

Figure 7.2: *A cross section of an STT layer.*

The straw wall is made of two layers of 50 μm Kapton foil coated with 0.2 μm of Al, 4 μm of Carbon and 3 – 4 μm of polyurethane as a welding layer and cut into ≈1 cm wide strips. These strips are then wound to form the 7.74 mm diameter straws. The straws are then assembled in a three layer array by gluing the densely packed straws. The position of an individual straw in the array is accurate to within 200 μm. The anode wires are held in place by means of end-plugs which centre the wire to an accuracy better than 50 μm. As a result the resolution on the distance of closest approach to a wire is $\approx 180 - 220$ μm.

7.4 MicroVertex Detector (MVD)

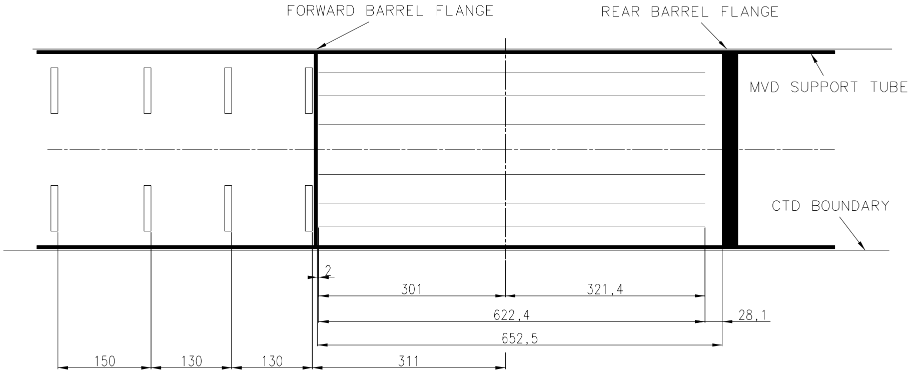

Figure 7.3: *A cross sectional view of the MVD.*

The MVD [69] is shown in Figure 7.3. The MVD is composed of two sections; the barrel section, covering the polar angle range 30° to 150°, shown in Figure 7.4; and the forward section, which extends the polar angle coverage down to 7°, shown in Figure 7.9.

7.4.1 Barrel section

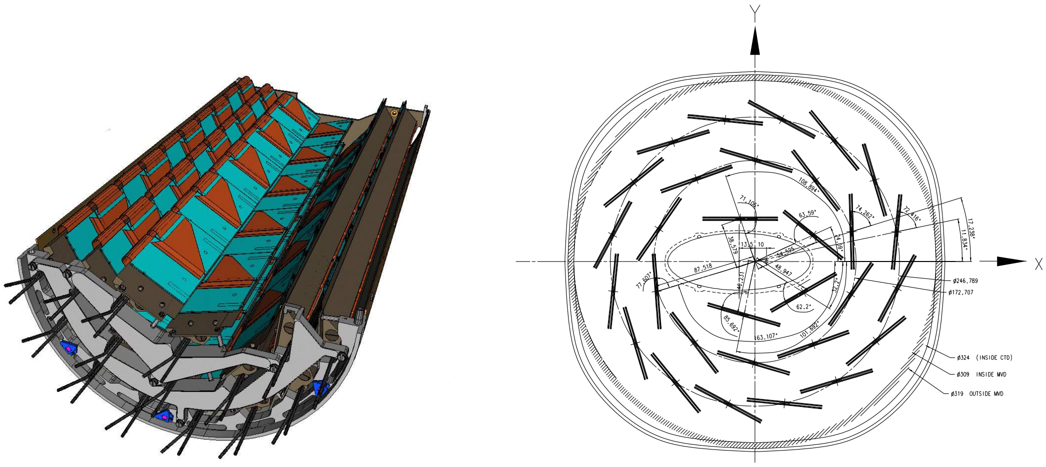

Figure 7.4: *3D and 2D views of the barrel section of the MVD.*

The barrel section is composed of 600 sensors, arranged in 3 concentric layers. The inner layer is composed of 4 “ladders” at radii between 4 and 5.5 cm, following the elliptical shape of the beampipe and providing an azimuthal angular coverage of 75%. The middle (outer) layer is composed of 10 (16) ladders at a radius of 9 (12.5) cm providing full azimuthal angular coverage.

Ladders

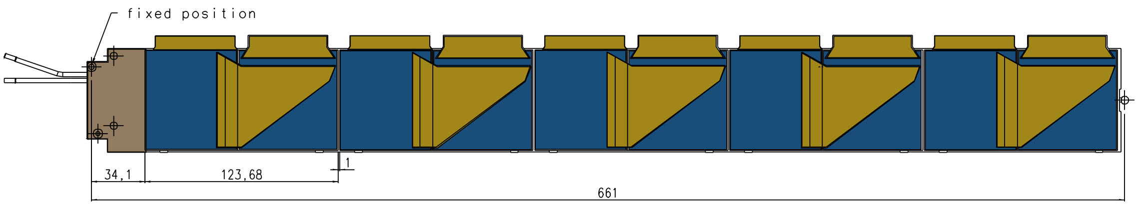

Figure 7.5: *Top view of a ladder.*

A top view of a ladder is shown in Figure 7.5. The sensitive region of a ladder is formed by five “modules” fixed side by side, with a 1 mm gap in between. These modules are connected to the carbon fibre support frame using Kapton spacers. This frame also supports the cabling and cooling to the front end electronics. In order to conserve the high resolution properties of the silicon sensors it is important that the ladder does not bend significantly with all components mounted. This deformation has been measured [70] and the ladders found to be flat within ± 35 μm.

Modules and half modules

A module is made up of two “half modules” mounted on top of each other and separated by Kapton spacers as shown in Figure 7.6. The Kapton spacers have

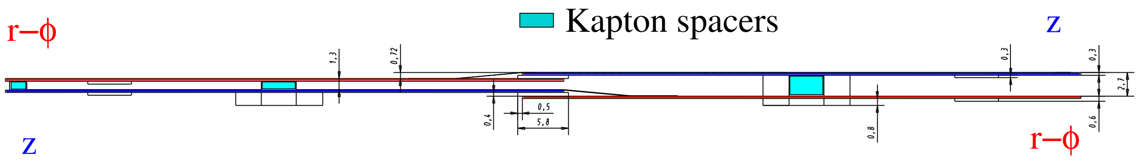

Figure 7.6: *Side view of a module.*

a cross section of a few square mm and different thicknesses guaranteeing parallel mounting of the two half modules.

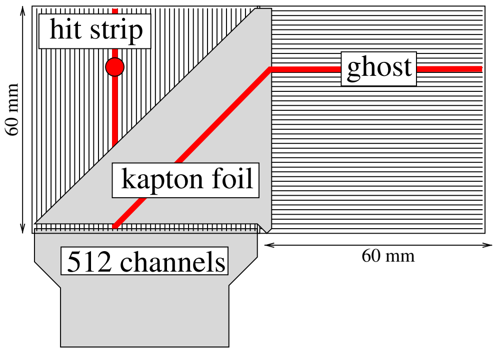

Figure 7.7: *Schematic diagram of a half module.*

Each half module is composed of two “sensors”, one with strips parallel to the beamline (providing r-ϕ information) and one with strips perpendicular to the beamline (providing z information). The two sensors are connected together via a Zirlex bar (5.8 x 65.44 mm, 0.4 mm thick) glued at the edge in between the the two sensors. The Zirlex assures good isolation of the HV side of one sensor from the ground plane of the other one. The active areas overlap by 2mm to minimise dead areas. The 1024 strips in a half module are connected to the front end electronics via 512 read out channels. This multiplexing is achieved by electrically connecting the strips of the two wafers, as shown in Figure 7.7. The electrical connection between the two sensors is made via a copper trace etched on 50 μm thick Kapton foil. Thus every hit strip will have an accompanying ghost on the other wafer in the half module.

Sensors

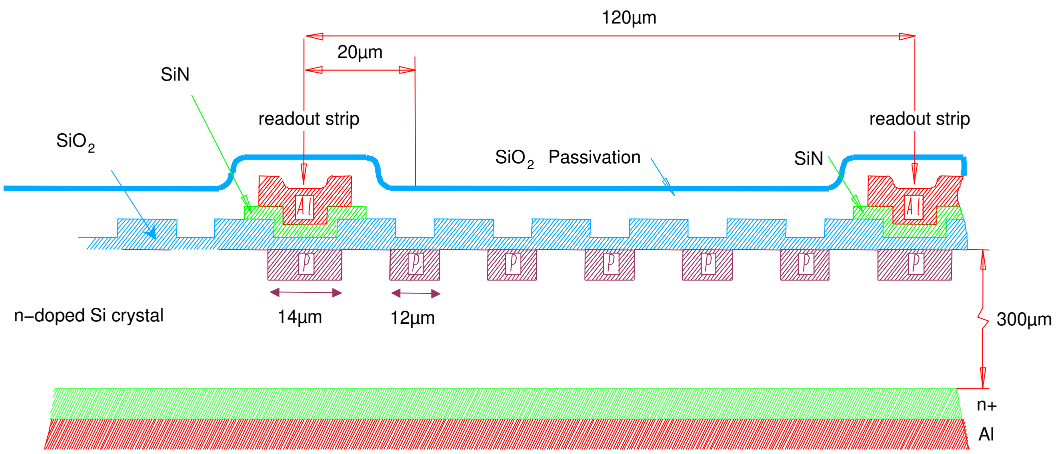

Figure 7.8: *Partial cross section of a sensor with two readout strips.*

The details, characteristics and performance of the sensors under test beam conditions are described elsewhere [71]. The sensors are single sided silicon strip detectors, made of 320 μm thick, high resistivity n-type silicon. The back plane is n^+ doped and aluminised. The front side is covered by 3082 p^+ doped strips with a 20 μm pitch. All the p^+ strips are biased using poly silicon resistors which alternately connect even and odd strips to either side of two bias lines which are perpendicular to the strips and located close to the sensor edges. Every sixth strip is 14 μm wide and read out by an AC coupled aluminium strip on top of the p^+ strips. The first and last strips are directly connected to the bias lines completing the bias ring around the active area, leaving 512 strips which are read out. Because of capacitive coupling between neighbouring strips, charge collected at intermediate strips induces charges on the readout strips. This limits the number of readout channels while achieving a spatial resolution of 10 μm for minimum ionising particles traversing the detector at angles of up to 30°.

7.4.2 Forward section

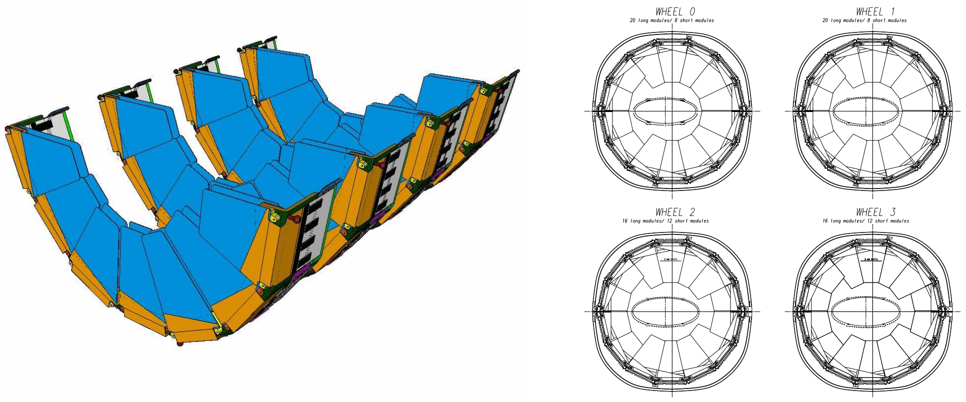

Figure 7.9: *3D and 2D views of the forward section of the MVD.*

The forward section of the MVD, shown in Figure 7.9, is composed of 4 planes perpendicular to the beam axis. Each plane has two sensor layers, mounted back to back on a support structure, separated by 8 mm in z. Each layer has fourteen sensors; adjacent sensors are displaced by 3 mm in z and overlap in azimuth by 4 mm. The sensors covering the forward region are very similar to the barrel sensors, apart from their shape. Each sensor has 480 readout strips, with a 120 μm readout pitch, which run parallel to one tilted side.

Chapter 8

The GTT algorithm

The upgrades to HERA and ZEUS described in the previous chapter, together with the improvements in performance and reduction in cost of PCs, provided an ideal opportunity to develop a new tracking trigger for ZEUS. In this chapter, the existing tracking trigger is first described, a more detailed motivation for a new trigger is then given, and finally the new algorithm is described.

8.1 Existing CTD-SLT

The CTD-SLT is a software trigger running on a transputer network, processing events parallel in space and time. The CTD-SLT uses only the z-by-timing and FADC (r-ϕ) data from the CTD. Using the stereo superlayer data to determine track z information, while more accurate, is too time consuming for the present system. The CTD-SLT algorithm is divided into four steps, the segment finding, the vector hit finding, the track finding and the event vertex determination. Each step is implemented in OCCAM code and run in parallel on separate transputers. A detailed description of the algorithm and performance can be found elsewhere [72], only a brief, simplified, outline is presented here:

8.1.1 Segment finding

For speed the segment finding uses integer only arithmetic. The segment finder operates on hits from one cell at a time using *unsigned* integer drift-time bins and wire numbers to find straight line track segments in the r-ϕ projection. Since only the unsigned drift time between the physical hit and the sense wire is known it is not possible to determine on which side of the sense wire plane the hit occurred. This

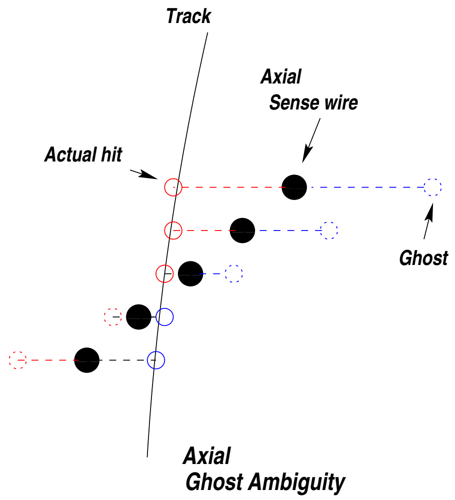

Figure 8.1: *Axial segment ghost ambiguity.*

is illustrated in Figure 8.1. The segment finder resolves this ambiguity by choosing the segment candidate whose direction points closest to the r-ϕ origin. This has a high efficiency for identifying the correct candidate for high p_T tracks, but for lower p_T tracks leads to a charge asymmetry due the ϕ asymmetry of the CTD geometry.

In order to assign the hits in a cell to a segment, the algorithm for each cell operates as follows.

- First the raw data for the CTD cell is unpacked and the global T0 value is subtracted.
- Next, seed pairs of hits predominantly on adjacent wires are found. If no seed pair is found the cell is abandoned.
- Using a linear extrapolation of the seed pair, the drift time on the next wire in increasing wire number is predicted. If a hit lying within the segment road width is found this is added to the segment candidate and this hit together with the adjacent hit from the seed pair is used as a fresh seed pair.
- This continues until either the cell boundary is reached or there are no more hits within the required road width. In this case, the procedure continues from the original seed pair in the direction of decreasing wire number, again until the cell boundary is reached or no more hits lie within the road width. If the number of hits in the completed segment is greater than two the segment is deemed complete and the hits are removed from the list of available hits for this cell and the segment finder begins searching for a fresh seed pair for additional segments in this cell.

As soon as the number of hits for the cell falls below three the cell is abandoned, since no more segments can be found. In addition the segment finder also stops looking for new segments in each cell as soon as three segments have been found. The segment finder finishes as soon as six segments, the upper limit per crate, are found or the entire hit data set has been used.

As noise hits are fully processed by the segment finder the time consumption is very sensitive to the data volume in the CTD. Similarly since the CTD occupancy in beam gas events can be very high, some compromise has to be made with respect to fully processing busy events to avoid wasting a large amount of time in non *ep* events.

8.1.2 Vector hit finding

The vector hit finding assigns hits in a cell with the same drift time in both the FADC and z-by-timing system to the segments. The segments are then transformed from the cell coordinate system to the ZEUS coordinate system.

8.1.3 Track finding

Track finding is performed on the data from two adjacent crates at a time, corresponding to a 45° mask in r-ϕ . Illustrated in Figure 8.4, the track finder algorithm proceeds in several stages.

- First, starting in the outermost superlayer, where the spatial separation of tracks is highest, a seed segment, not yet matched to a track is found.
- Using this seed segment, the expected z position for the next inner vector hit is calculated based on a linear interpolation to the nominal interaction point, if previously matched hits provided z-information.
- The expected azimuthal position of the next vector hit in, $\phi_{\text{ext}}(SL)$, is calculated using a linear extrapolation of the seed position, $\phi(SL+2)$ and direction, χ,

$$\phi_{\text{ext}}(SL) = \phi(SL+2) + \chi\omega(SL)$$

where SL is the number of the superlayer and

SL	1	3	5	7	9
ω(SL)	0.3	0.25	0.19	0.16	0.0

Superlayer 1 usually contributes the most z hits to a track, while its lever arm in (r,z) is shortest. Hence effects of possible mismatches are largest here. Thus if segments have already been found in superlayers 3, 5 and 7, a more stable quadratic approximation of the track trajectory is made

$$\phi_{\mathrm{ext}}(Sl=1)=\phi(Sl=3)-3\phi(Sl=5)+3\phi(Sl=7).$$

Since all segments should have the same curvature, if there is a segment in this superlayer with a ϕ position within 3.44° of the predicted position, and a curvature, κ, within 0.04 of the previous segment this segment is matched to the track. Up to 4 candidate segments can be matched in each superlayer. The one with the smallest value of $\Delta\kappa+10\Delta\phi$ is used.

- As depicted in superlayer 1 of Figure 8.4, a segment can be split across a cell boundary. If only one segment is matched to a track, then the additional segment can give rise to a "split" track where the track has been found twice. To reduce this possibility, a second segment can also be matched to this track if

$$\begin{aligned}\Delta\phi &< 1^\circ\\ \Delta\chi &< 15^\circ\end{aligned}$$

- The segment last matched is then used as a fresh seed and the matching proceeds again into the next inner axial superlayer until at least one segment is found in superlayer 1 and at least one in a higher superlayer, or one segment in superlayer 3 and all higher superlayers with at most one gap in one of these higher superlayers, when the segments are added to the track and removed from the list of segment candidates.

- If at least three vector hits, or two vector hits from the inner three superlayers can be assigned to a candidate track, then the track is accepted.

- The track radius is calculated from the centre of each segment in r-ϕ using a fast circle fit, similar to that described in Section C.1.

- The polar angle of the track at the origin, ϕ_h, and its charge are determined from the outermost vector hit.

- Finally the track vertex and polar angle are calculated from a weighted least-squares line fit in r-z.

This process is repeated until either six tracks have been found in the mask, or all seeds in all layers have been tried.

8.1.4 Event vertex determination

Because of the overlapping two-crate masks used in the track finding, it is possible for a track to be found twice. The tracks from all masks must then be merged and for each pair of tracks sharing one or more vector hits one is deleted. Up to the first 20 non-duplicate tracks are then used for the event vertex determination.

The event vertex is determined using a "binning algorithm". The CTD is split up into 21 bins, each 20 cm wide and overlapping with its neighbours by 10cm. The number of tracks originating in each bin is counted, giving a distribution with a maximum close to the event vertex. In the case of a single maximum bin the vertex is the position of the centre of this bin.

Beam gas rejection

In order to decide whether an event is beam gas background the following quantities are formed:

nr_tracks	=	the number of tracks found by the SLT.
mpv	=	the most probable vertex, in the centre of the bin with the most entries.
vtx_tracks	=	number of tracks coming from the bin next to the mpv bin.
beam_type	=	number of tracks with $\lvert\text{gradient}\rvert \geq 1.0$ and $\lvert z_{vtx}\rvert \geq 95.0$ cm.
$\overline{\text{product}}$	=	Average product of track gradient and track intercept, characterising the global event tracking topology. This quantity is close to zero for physics events and can get very large and negative (~ -500) for beam gas events.
z_bin(i)	=	number of tracks pointing to bin number i. Where the bins are numbered in increasing z.

An event is declared to be a beam gas type event if one of the following conditions is fulfilled:

- $((\text{z\_bin}(1) \geq 2).\text{OR}.(\text{z\_bin}(21) \geq 2)).\text{AND}.(\text{z\_bin}(2\ldots 20) = 0)$
- $(\text{z\_bin}(1) + \text{z\_bin}(21) - \text{z\_bin}(\text{mpv}) \geq 10).\text{AND}.(\text{vtx\_tracks} \leq 4)$
- $(\overline{\text{product}} \leq -500).\text{AND}.(\text{nr\_tracks} \geq 8).\text{AND}.(\text{vtx\_tracks} \leq 4).\text{AND}.$ $(\text{beam\_type} \geq 4).\text{AND}.(\text{beam\_type} \geq 0.5 \cdot \text{nr\_tracks})$

8.2 Motivation for a GTT

The motivation for a GTT is driven by two main factors; the desire to improve the performance of the CTD-SLT in light of the increased event rate after the upgrade; and the need to improve heavy flavour triggering in order to maximise the statistics available to heavy flavour analyses, such as those discussed in Section 7.1.

8.2.1 Improvements to the CTD-SLT

The CTD-SLT was first included in the trigger system in 1993, however its output was only used at the GSLT after the maximum latency was reduced from more than 90 ms in 1993 to below 25 ms in 1995. After the upgrade average rates of up to ≈400 Hz are expected compared to ≈150 Hz in 2000 [73]. It is thus desirable to improve the speed of the CTD-SLT even further. Since the CTD-SLT algorithm has already been extensively optimised [72], this improvement must be achieved through improvements to the computing architecture.

It is also desirable to improve the event vertex resolution since this provides a powerful way of rejecting non-physics backgrounds such as beam-gas interactions. The ≈8 cm resolution of the existing CTD-SLT allows a vertex requirement of $-60 < z_{vtx} < 60$ cm to be imposed at the GSLT. Studies have shown that an improvement in the event vertex resolution to ≈2 cm would allow the vertex requirement to be restricted to $-40 < z_{vtx} < 20$ cm, reducing the SLT output rate by a factor of 2 [74]. Such an improvement can only be achieved by using the stereo layer information, which requires significantly more processing than the z-by-timing information.

Thus an improved CTD-SLT which:

- supplements the transputer network with a farm of high performance PCs;
- runs as a single, linear, process;
- includes stereo layer information;

was proposed. The requirement that the algorithm runs as a single process has several important advantages; there is no longer any need to transfer data between processors hosting different sections of the algorithm; there will be no need to merge overlapping regions since the algorithm will have access to the complete data for each event; components of the algorithm can be easily reordered or new ones added making it much more flexible.

8.2.2 Heavy flavour tagging at the SLT

Even including the stereo layer information the resolution of the CTD-SLT would not be accurate enough to distinguish the displaced vertices left by heavy flavour decays. In order to do this data from the MVD must be used.

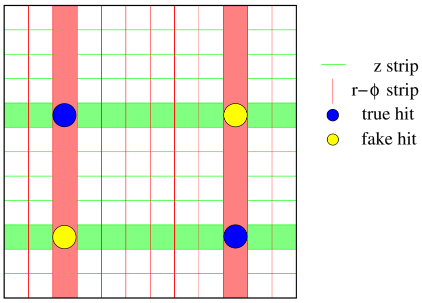

Figure 8.2: *Pattern recognition in a strip detector with two hits.*

Studies of a stand alone MVD-SLT [75] indicated that it could not provide useful input to the GSLT. The main problem was the high algorithm latency, estimated to be between 22 and 800 ms per event. This was a result of the complex pattern recognition inherent in a strip detector when more than one track passes through the same sensor, illustrated in Figure 8.2. This is further complicated by the ghost hits discussed in section 7.4.1 and by noise.

In order to solve this problem a global tracking trigger, using existing CTD-SLT information to aid the pattern recognition was first studied in [76]. The approach used in the GTT and presented here is to first improve the current CTD-SLT, as described above; then use this new algorithm to solve the pattern recognition in the MVD and finally combine the information from both detectors to give the best track reconstruction.

In addition to improving the tagging of heavy flavours in the barrel region, the new components should also extend the acceptance for well reconstructed tracks to the forward region, where much of the interesting heavy flavour physics occurs. The potential inclusion of tracking information in the forward region using both the STT and MVD forward wheels both offline *and* in the second level trigger, is very desirable.

8.3 The GTT algorithm

The design of the GTT algorithm borrows heavily from the existing CTD-SLT algorithm [72] upon which it is based. The algorithm proceeds in four logically distinct stages: segment finding, axial track finding, z track finding and vertex finding. These stages will now be described in detail.

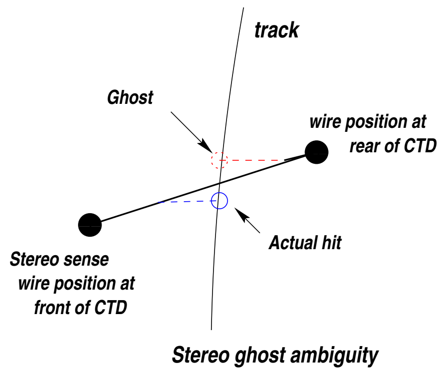

Figure 8.3: *Stereo segment ghost ambiguity.*

8.3.1 Segment finding

In contrast to the existing CTD-SLT segments are now found in both the axial and stereo superlayers, for reasons which will be discussed in Section 8.3.3. The segments are found using the same algorithm as the existing CTD-SLT, described in Section 8.1.1. Since wires in the stereo superlayers don't have a single r-ϕ position the segment gradients are dependent on the z position and the effect of ghost hits, shown in Figure 8.3, is somewhat modified. However, using the same criterion as for the axial segments still has a reasonable efficiency for correctly resolving the ghost ambiguity.

8.3.2 Axial track finding

The CTD portion of the GTT r-ϕ track finding is based upon the existing CTD-SLT algorithm, with the following modifications:

- The algorithm is no longer parallel so data from all crates are considered in a single process.
- Since the z-by-timing information is not present, all stages concerning this are omitted.
- The maximum number of segments per cell has been increased from 3 to 4.
- The track charge and ϕ are calculated from the fit, rather than the outermost segment.

Once a track has been found in the CTD, the algorithm goes on to match hits from the MVD to it. Since the r-ϕ and z wafers within an MVD half module are multiplexed together, it is not known *a priori* which hits are z hits and which are r-ϕ hits. Consequently all hits are considered as potential r-ϕ hit candidates.

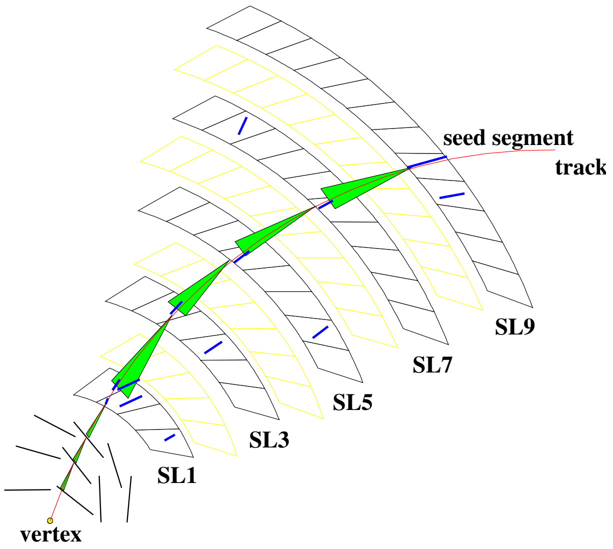

Figure 8.4: *Schematic diagram of the r-ϕ track finding.*

- Starting from the outermost MVD layer, the ϕ position of the track at the layer radius is calculated and the ladder at this ϕ position considered. If this ϕ position is close to the edge of the ladder the adjacent ladder is also considered. This is to take account of the geometry of the outer two layers in which adjacent ladders overlap in ϕ.

- For each unmatched hit in the ladder(s), the difference between the track ϕ at the hit's radius and the hit's ϕ is calculated. The closest hit on each possible ladder in this layer is then matched to the track if $\Delta\phi$, the difference between the track ϕ and the hit ϕ is smaller than the matching criterion in this layer, and the hit removed from the list of candidates. At present, the matching criterion is taken to be 0.015 rad for all layers, although these values will be reviewed when real data is available.

- Any matched hits are added to the track with a larger weight than the CTD segments (currently 1000) and the track parameters are recalculated using an unconstrained fit, described in Section C.2.

- The algorithm then proceeds in the next innermost MVD layer until the inner layer is reached, or there are no further unmatched hits.

The distribution of residuals with respect to the predicted track ϕ position is shown in Figure 8.5 for CTD superlayer 9 tracks. This clearly shows the improvement of the predicted ϕ positions once the first MVD hit has been matched to the track. Using these the ϕ windows for the MVD matching criterion and the weight to give to the MVD hits can be tuned for future running.

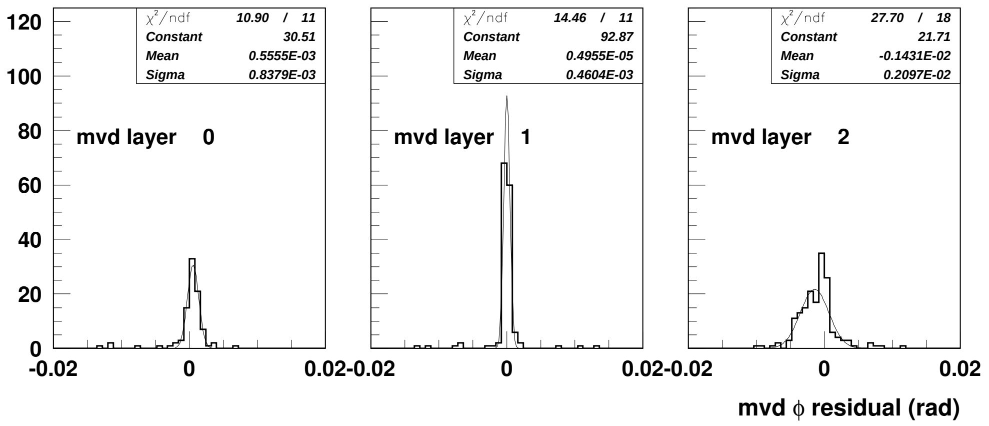

Figure 8.5: *The ϕ residuals of the closest MVD hits to extrapolated track during the MVD r-ϕ matching stage.*

8.3.3 z track finding

CTD stereo segment matching

In the existing CTD-SLT, FADC hits in the inner three axial superlayers of the CTD are matched with hits from the z-by-timing system on the same wires. This enables a fast calculation of the z position of the hits used for the axial track finding and so the fast reconstruction of the polar angle of the tracks themselves. However, for phase one of GTT running the data from the z-by-timing system will not be available since this would require a substantial reorganisation of the data flow within the CTD transputer network. This means the stereo data alone will be used.

This presents several difficulties since each stereo wire in the CTD spans a large angle (4 cells) and so does not provide very precise information on the axial position of the hit upon it. Consequently, until a stereo hit has been matched to a track, no z position is available, and each stereo hit may be assigned to any track passing through the range of ϕ spanned by the wire.

This means that the r-ϕ and z positions of each hit must be calculated for each possible track candidate within its r-ϕ range. For the inner stereo layers, this range is reasonably large (in superlayer 2 the angle corresponding to 4 cell is $\approx 36°$) which presents a significant problem since the track occupancy nearer the interaction region is high and thus the amount of ambiguity which must be resolved is large.

Because of this, solving the track intersections in r-ϕ with the stereo wires represents one of the most costly steps in terms of the processing latency. In order to keep the

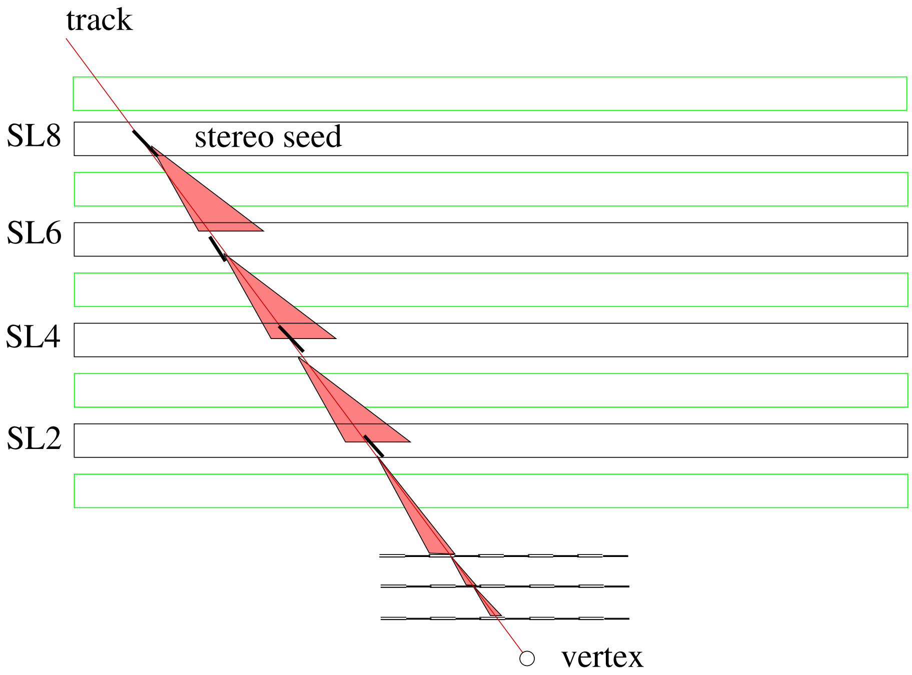

Figure 8.6: *Schematic diagram of the z-s track finding.*

processing time within acceptable limits segments are found in the stereo layers using the same algorithm as for the axial segments. Only the end points of the segments are used for calculating the intersections in z. This introduces some additional latency to the segment finding, but can reduce the stereo matching time by a factor of up to 8.

For each track found in the axial track finding, the algorithm proceeds as follows:

- Starting in the axial track's outer stereo superlayer, where the spatial separation of tracks is highest, all possible segments are considered as seed segments.
- The intersections of the segment end points with the track are calculated and used to provide a position in z and s - the path length along the track. [1]
- The z-track parameters (gradient and intercept [2]) of the track are calculated using a straight line fit and the track is extrapolated into the next stereo layer.
- The z positions of each segment in the next stereo layer are then calculated from the intersection of the segment end-points as above, and each segment meeting certain quality requirements e.g. lies both within the CTD and a

[1] s is used rather than the radius r, since the tracks in z are helical in r but straight as a function of s.

[2] the z position at the track's distance of closest approach to the origin in x and y.

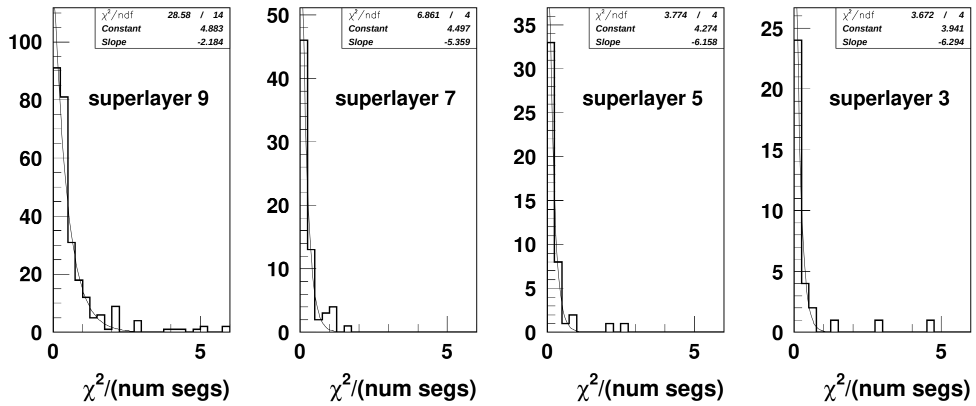

Figure 8.7: *The distribution of* χ^2/nseg *for superlayer 9, 7, 5 and 3 tracks.*

window of z of the extrapolated position and has a realistic gradient is then considered.

- This continues in each successive stereo layer, with the fit being recalculated at each stage, until a track with segments in each stereo layer is found, when the track is deemed complete and the matched segments are flagged as belonging to this track.

- If no successive segment is found, the seed finding starts again in the next outer stereo layer but one and the process is repeated until either the track is complete, or no successive segment is found in which case the track is abandoned.

This is illustrated in Figure 8.6. Early versions of the algorithm stopped as soon as a candidate track with segments in each layer was found. However, for very busy events, the high occupancy in the inner layers means that each inner cell can contain many segments belonging to several tracks. To improve the resolution and efficiency in this case, the algorithm was re-implemented to search for all track candidates and then select the candidate with the smallest χ^2, only then flagging the segments as belonging to the track. The χ^2 measure of the best fitting final z-track is shown in Figure 8.7.

In principle this can significantly increase the latency. However, since many segments are common to several z-track candidates for the track the segment book-keeping was improved so that each candidate segment calculated is stored with the track. Searching for the segments introduces about 30% additional latency for low occupancy events where the latency is an any case low, but can save as much as 30% for busy events. In this case, searching the segment list enables multiple z-track candidates to be found in busy events with slightly less than a 40% latency increase with respect to stopping after one candidate. In addition, it can increase the efficiency for finding tracks on the vertex by as much as 50% in some events, and so this additional latency is deemed acceptable.

The efficiency of the algorithm is very dependent on finding the correct segments. This is in turn very sensitive to the first stage of the algorithm, through the gradient of the seed segment in the outer superlayer. As a result of the assumptions about which hits constitute the segment at the segment finding stage, this can vary somewhat from the actual track gradient. If one or more of the hits in the segment are incorrect the extrapolated position may also be incorrect and the correct segment in the subsequent layer may lie outside the window. Using a larger window will enable the next segment to be correctly found, but will also increase the chances of matching an incorrect segment.

Consequently, if the track has any MVD hits matched at the axial finding stage then the z position of the wafer containing the hit can be used to provide an additional constraint with a resolution of the order of $\pm$3cm in z coming from the wafer size. The MVD hits are included with a weight in the fit for the first segment, and removed from the calculation of the CTD stereo track when segments in all layers have been found.

Figure 8.8 shows the z-residuals of the segment end points with respect to the intermediate fits extrapolated into the appropriate superlayers during the stereo matching for fits with and without an MVD wafer guide position. As more segments are matched the residuals become smaller, as expected. Similarly, for longer tracks (starting in the outer superlayers) the predicted position is better under control.

MVD z hit matching

Once CTD stereo segments have been matched to an axial track and the MVD wafer guide position removed, the algorithm goes on to match MVD z-hits. Only tracks with MVD r-ϕ hits are considered, since the r-ϕ MVD hit matching is very efficient, and so tracks without these are potentially badly reconstructed, and as such the z information is in any case likely to be unreliable.

The z-matching procedure is essentially the same as for the r-ϕ matching. However, since MVD r-ϕ positions are already known, the algorithm looks for unmatched hits only in the z-wafers of the half modules with matched r-ϕ hits.

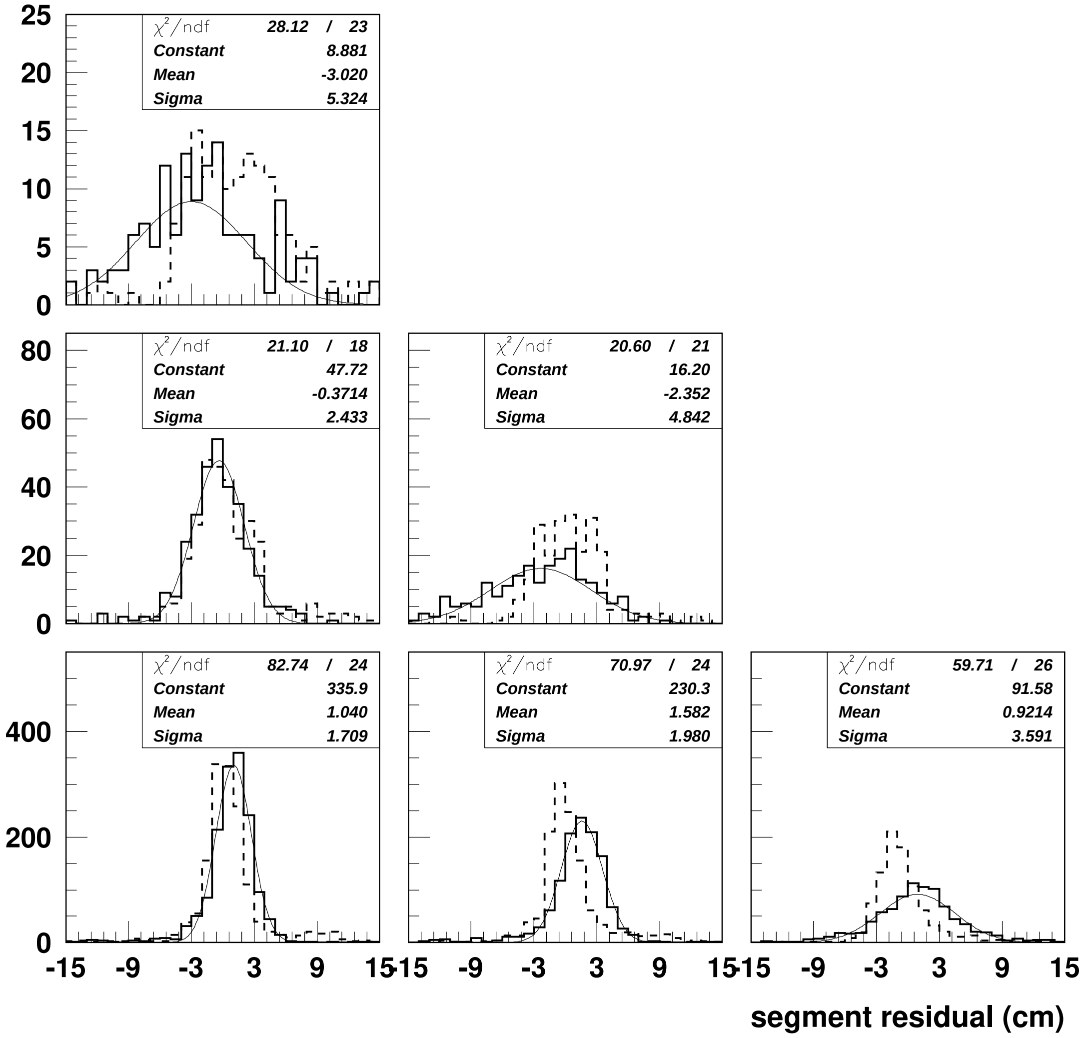

Figure 8.8: *The z-segment residuals of the segment end points with respect to the extrapolated track position during the stereo segment finding. From the top: superlayer 5, 7 and 9 tracks; from left to right: the extrapolated positions in superlayer 2, 4 and 6. The dashed (solid) histogram shows the residuals (without) using the MVD wafer guide position.*

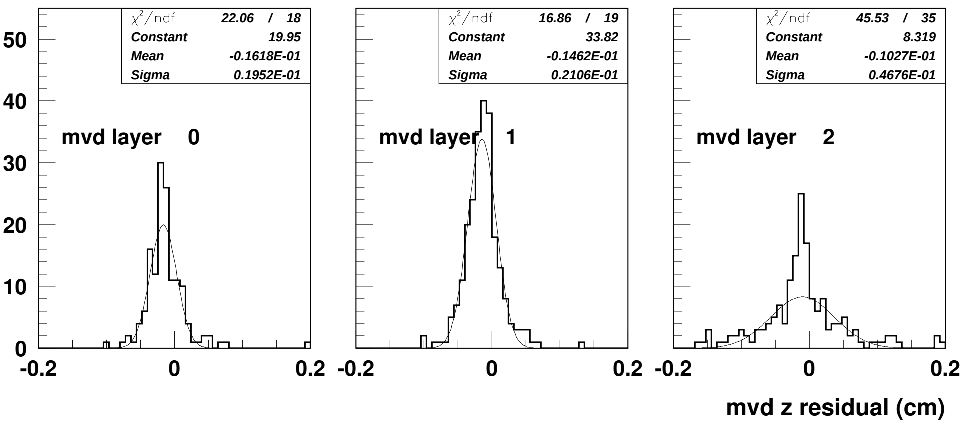

Figure 8.9: *The z residuals of the closest MVD hits to extrapolated track during the MVD z matching stage for superlayer 9 tracks.*

- Starting in the outermost MVD layer, if there are unmatched hits in the expected z-wafer, the track intersection with the wafer is calculated.

  Whereas the hits in r-ϕ have definite positions in both coordinates, the z-hits have a definite position in z only, since the MVD wafers are not cylindrical about the track origin, so the intersection of the track with the wafer must be calculated in order to obtain positions in both z and s along the track for the subsequent fit.

  This is done using essentially the same iterative algorithm as the track intersection for the stereo hits, described in Section C.3, with the simplification that the displacement with respect to the wafer (equivalent to the sense wire in the case of the stereo wires) is identically zero.

- All unmatched hits are then compared with the predicted z-position, and the closest hit matched to the track if it lies within a window of 6cm of the predicted position.

- The hit is then added to the track with a weight of 1000 and the fit in s and z recalculated.

- Hits are then sought in the next innermost layer, until either hits are found in all possible z-wafers, or there are no hits remaining.

Figure 8.9 shows the residuals of the MVD z-hit candidates during the z matching for superlayer 9 tracks. As expected, the residuals become smaller once the first

MVD hit has been included. For future versions of the algorithm the window in z will be reduced to values commensurate with the observed widths of the residual distributions.

8.3.4 Event vertex determination

Since there is likely to be a large degree of residual beam gas contamination in the event spectrum after a GFLT accept the presence of a clean ep interaction vertex cannot be guaranteed. The purpose of the primary vertex algorithm is then to make a fast estimation of the presence of a possible vertex and to ascertain its likely position in z rather than a complete detailed reconstruction.

Since the event vertex position in x and y is not known, the path length, s, with respect to the distance of closest approach to the origin in x and y for each track at the vertex is not known. In this case, the vertex is found by making the approximation that all tracks intersect at their distance of closest approach to the origin in x and y and so the track-vertices can be used immediately. This results in a degradation of the vertex resolution and the introduction of a small bias dependent on the x-y beam position but with a considerable computational saving.

The algorithm uses a binning algorithm similar in principle to the existing CTD-SLT, however, since the track vertex resolution for tracks containing CTD stereo information and MVD hits is significantly better than for the existing CTD-SLT, the size of the bins has been reduced to 13 cm. In principle this should be reduced further to the order of 4 times the vertex resolution, since taking too large a window will result in the inclusion of tracks not truly on the vertex. In addition, rather than using overlapping bins as in the case of the existing CTD-SLT, non-overlapping bins are used. This was found to be both less time consuming, and with additional modifications, to yield more stable and precise results [77].

The algorithm itself proceeds as follows.

- Looping over each track, i, with z-information, the bin corresponding to the track vertex is found. The track vertex, z_i, is then added to the running sum of all the track vertices in that bin, weighted by the sum of the number of stereo segment end points and MVD z-weights used for the track, w_i. The total number of such weights is also stored for this bin, and global counts of stereo segment end-points and MVD z-weights correspondingly increased.

  In this way, the quality of each track is automatically included, taking due consideration of the information from the MVD.

- After all tracks have been considered, the most probable bin[3] is found and a proto-vertex position calculated using

$$z_{\text{proto}} = \frac{\sum_{i\in\text{bin}} z_i w_i}{\sum_{i\in\text{bin}} w_i}. \tag{8.1}$$

- New running sums of the weights and weighted z positions are then calculated for all tracks in the most probable bin, and the two adjacent bins lying within 9cm of this proto vertex position, and an updated vertex position calculated using equation 8.1, together with the RMS width of the vertex.

This is found to be very stable against the presence of outliers, and reduces the amount of computation with respect to the overlapping bin algorithm.

For a very well reconstructed vertex the sum of weights and the RMS can then be used to estimate the quality of the vertex. In addition, the fraction of weights assigned to the vertex with respect to the total sum of weights gives a measure of the likelihood that the vertex has been misidentified. This is particularly useful in the case of beam gas events where no actual vertex may be present.

Beam gas rejection

Once the position and width of the vertex has been identified, it remains to decide whether this corresponds to an $e-p$ interaction or a beam gas event. This remains the least tested aspect of the complete algorithm, since no beam-gas Monte Carlo or data is currently available including the MVD. Thus, until such data is available, the same requirements as the existing CTD-SLT, described in Section 8.1.4, will be used.

8.4 Future work

When information on the event vertex and z-tracks are available, several additional stages might be envisaged:

- A second pass of the z-matching stage may be performed.
- The positions of the MVD hits may be recalculated if the performance of the algorithm is impaired by differences between the MVD design and actual geometry.
- Secondary vertices may be identified.

[3]The bin with the highest number of weights.

8.4.1 Second pass of z-track finding

As was discussed in Section 8.3.3, the efficiency of the algorithm is very dependent on finding the correct initial segment, in particular its gradient. In the initial z-track finding, the coarse z position of matched MVD r-ϕ hits was used as a constraint, reducing the sensitivity to mismeasured initial segments. In the same way, the event vertex can be used as a constraint for a second pass of the z-track finding. In this second pass, the vertex position is included with a weight (currently 10) in the fit for the first segment and the z-track finding is repeated, exactly as for the first pass.

8.4.2 Dealing with non-ideal wafers

In all the above it has been implicitly assumed that the barrel MVD wafers are perfectly flat and lie parallel to the beam line. The effects of this assumption and possible methods for dealing with deviations from them will now be discussed.

Wafer misalignment

This will lead to small differences in the x and y coordinates of the strip end points for an r-ϕ strip and in the z coordinates of the end points for a z strip. This has the effect of introducing a small stereo angle into the strip. Within the GTT, the geometry is encoded in look up tables for the end points (in x, y and z) of the first and last strip on each wafer.

During the r-ϕ matching, since no information on the z position is yet available, the average of the two end points can be used for the r-ϕ position.

In the case of z matching, the r-ϕ position of the track through the wafer will be approximately known, and so the position along the z strip is already available enabling a more precise calculation of the z coordinate of the hit. For end point misalignments of up to 100 μm for a z strip, knowledge of the position along the strip with a reasonably course resolution of up to 1mm will enable the z position to be calculated to within 2 μm. This is significantly smaller than the intrinsic cluster resolution, so further iteration is not required.

For the r-ϕ wafers, once the z information of the track is known, the r-ϕ positions can be recalculated and the track refitted, if required.

Further iterations through the track fitting are not envisaged.

Non-planar wafer geometry

The wafers are known to be non-planar by up to 100 microns. Knowledge of the course ($\sim$1mm) z and r-ϕ position will enable the displacement of the hit from the plane to be known to within 10 microns if the wafer geometry is sufficiently well known [77]. This can then be included in the initial matching in the case of z hits, since the z information is good enough, and the r-ϕ position is already known. For the r-ϕ hits, this information can be included when refitting for the wafer alignment as mentioned above.

In the case that the wafer geometry is not well enough known, this would simply lead to an effective degradation of the cluster resolution in some parts of the wafer. Effects of this order are only likely to be of concern for secondary vertex finding, which is not yet implemented in the algorithm.

8.4.3 Secondary vertex finding

The long lifetimes ($\approx 10^{-12}$ s) characteristic of charm and beauty decays allow hadrons containing these quarks to be identified through their displaced vertices (of the order 200 μm). Figure 8.10 shows a schematic diagram of the decay of a neutral heavy flavour hadron into two charged particles. The displaced vertex can either be identified directly, by finding the intersection point of the two daughter tracks, or indirectly through the large impact parameters of the daughter tracks, relative to the primary vertex.

The version of the GTT presented here already contains almost all the necessary functionality to calculate impact parameters and find secondary vertices (i.e. unconstrained tracks and the primary vertex position in z), only the primary vertex position in x and y remains to be found. This can be achieved through a binning algorithm, similar to that for the primary z vertex. However, a binning algorithm in x at a fixed y will only work if the correct value of y for the vertex is used, and similarly for y. In order to account for this it has been suggested [77] that the intersection[4] in the x-y plane for each track with all the remaining tracks is calculated and the x and y values of the *intersections* binned. The bin with the highest occupancy can then be used to recalculate the primary position in x and y, as with the primary z vertex.

[4]Close to the origin, to a good approximation, the tracks are linear and a linear approximation can be used, greatly reducing the computational overhead.

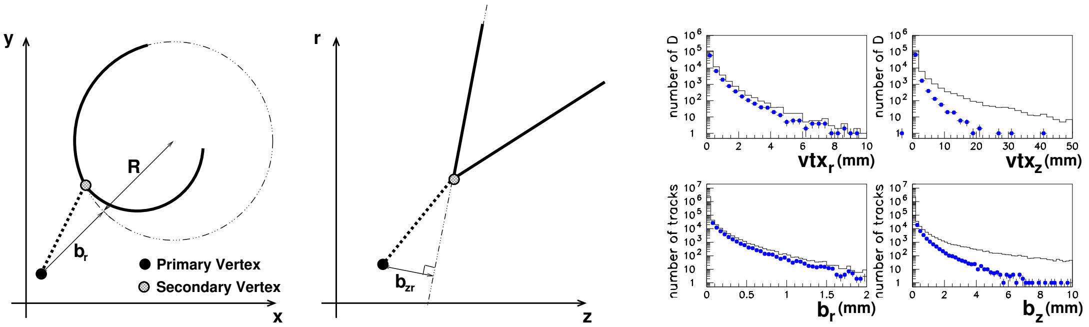

Figure 8.10: *Secondary vertex displacements and impact parameters for D mesons (histogram) and D mesons whose daughters have* $p > 0.3$ GeV *and* $|\eta| < 2.5$ *(points).*

Once the primary vertex positions are known in x, y and z, tracks with intersections where, for example, the x coordinate from the x-y and x-z intersections correspond can then be used as secondary vertex candidates, and a finer binning applied. Much work remains to fully develop this aspect of the algorithm and evaluate whether secondary vertices can be successfully identified.

Chapter 9

Performance of the GTT

9.1 MVD simulation

Early studies of the GTT algorithm performance in a multi-track environment were limited to using multiple random track events generated using GEANT. This was because the Monte Carlo detector simulation available was an early development version which contained several bugs and limitations:

- The geometry was based on very early design drawings which were significantly different from final design from which the MVD was constructed.
- The cluster encoding was partially incorrect, which is significant for realistic hit resolutions since only the MVD cluster data is available to the GTT.
- There were problems with the digitisation with respect to missing clusters and very large clusters containing nonphysical charge deposits.
- It was not possible to run the Monte Carlo detector simulation on physics events.

To solve these problems, a new version of the Monte Carlo detector simulation is being written by the MVD offline group. However, at the time of developing the algorithm this version was not yet available, so a fast simulation of the MVD was implemented using the final design geometry.

The simulation takes as input all particles in the event record (FMCKIN) that were produced inside, and decayed outside, the MVD volume. The intersection points of the particles with the MVD wafers were determined assuming a helical trajectory in a homogeneous 1.43 T B-field parallel to the z-axis. Individual strip responses were then simulated assuming a Gaussian distribution of deposited charge, centered on the intersection point, with a width between 1 and 5 strips depending the angle of incidence of the particle. This information was then used to construct the raw data data structures needed by the GTT.

This fast simulation guarantees the correct geometry and cluster encoding and can be run on any existing Monte Carlo physics events. Until the improved full Monte Carlo detector simulation is available, and later, real data from the MVD, this provides the best means to gauge the algorithm performance.

9.2 Event sample

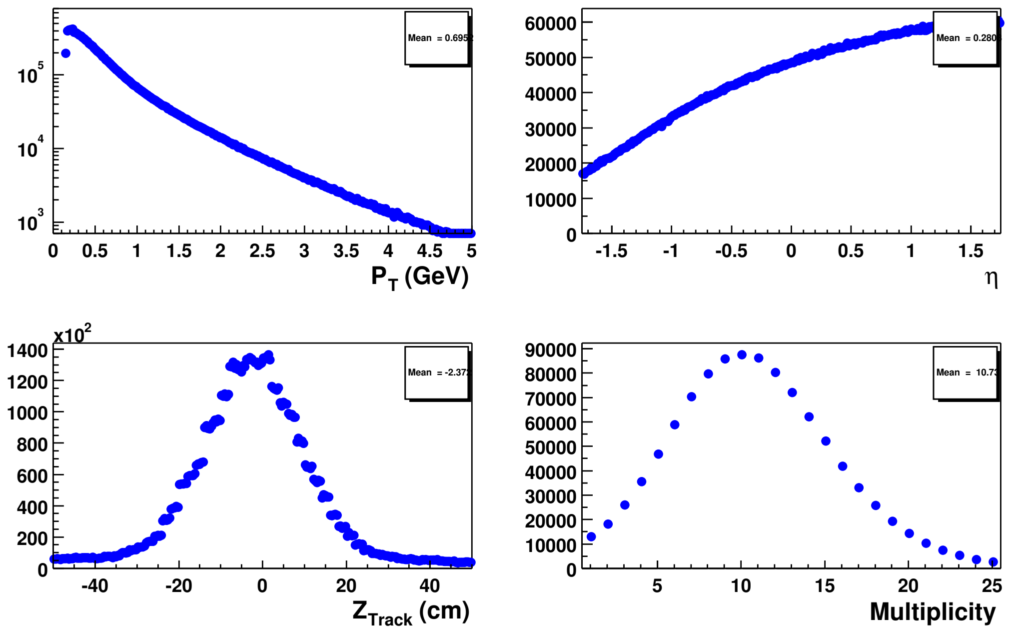

Figure 9.1: *p_T, η, z_{track} and multiplicity distributions of the Monte Carlo used to evaluate the GTT.*

A sample of 1.1M dijet photoproduction events with $E_T^{jet1,2} > 4.0$ GeV and $\eta^{jet1,2} < 3.0$ which had been passed through the full ZEUS simulation was run through the MVD simulation described in Section 9.1. All particles in FMCKIN were considered for the set of reference tracks against which all the efficiencies and resolutions were measured. A particle was accepted as a reference particle if:

- it was charged;
- it was used in the GEANT simulation (FMCKIN_ISTHEP > 10000);

- it came from physics rather than interactions with the detector (FMCKIN_DAUGHTEROF < COUTAB(FMCKIN));
- it was produced before the inner wall of the CTD ($r < 30$ cm);
- it had $p_T > 0.15$ GeV, $|\eta| < 1.75$ and $|z_{track}| < 50$ cm.

Figure 9.1 shows the p_T, η and z_{track} distributions of the reference particles together with the number of particles passing these cuts in each event.

The set of measured tracks under consideration was matched against these reference particles using the separation in η-ϕ space, $\Delta R = \sqrt{\Delta\eta^2 + \Delta\phi^2}$, as a matching criterion. All track-particle combinations were considered and a pair matched if it was the closest combination for both track and particle and

$$\Delta R \ < \ 3\sqrt{2} \cdot \sqrt{\sigma_\eta^2 + \sigma_\phi^2}.$$

Where σ_η and σ_ϕ are the widths of the Gaussians used to estimate the resolutions, presented in Table 9.1. For the evaluation of the GTT the GTT (CTD Only) resolutions are used for the matching criteria.

Event displays

Before drawing quantitative conclusions based on the reconstruction of these 1.1M events it is informative to first draw some qualitative conclusions based on individual events. In Figure 9.2 the dijet nature of the MC events used to evaluate the trigger can clearly be seen. The upper display, from the ZEUS event display LAZE, shows the offline tracks [78] together with the individual hits in the CTD. The ghost hits in both stereo and axial layers can be seen to lie in lines tangential to the radial tracks, justifying using the same criteria to reject ghost segments in both the axial and stereo segments in the GTT. The lower display, from the MVD event display GREEN shows the GTT tracks together with the matched segments. Of the 11 offline tracks, 4 can be seen to have resulted in split tracks in the GTT and one has not been reconstructed. These split tracks will degrade the performance of the GTT because the segments and MVD hits of the true track will be spread across several tracks reducing the resolution. The tracks which were not split picked up all possible segments and MVD hits. In Figure 9.3 a busy event is shown. The reconstruction of tracks is slightly less efficient, however, tracks with many segments and MVD hits are still found and the general event shape and vertex are well reconstructed.

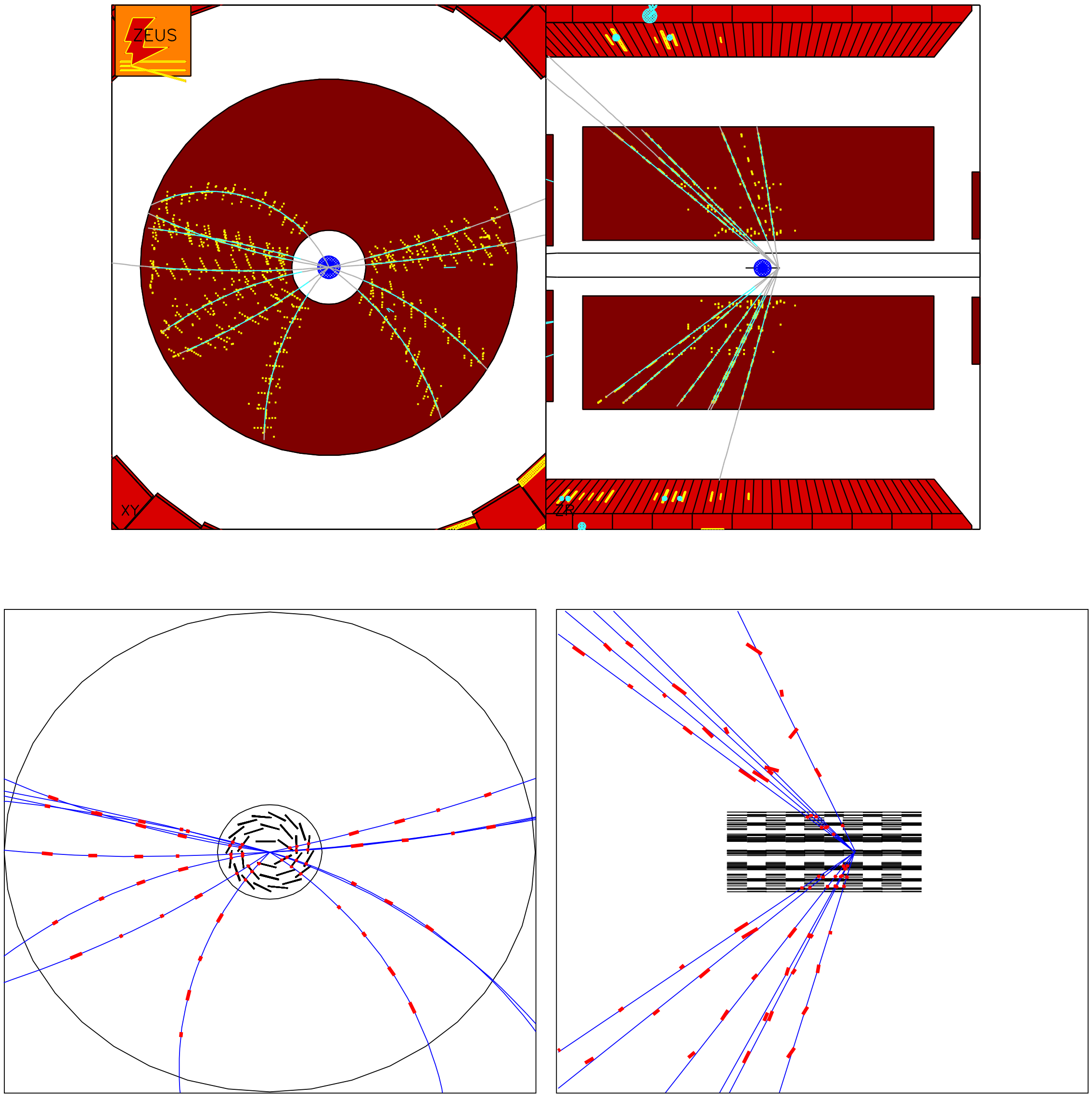

Figure 9.2: *Event displays showing the offline (upper) and GTT (lower) tracks for the same MC event.*

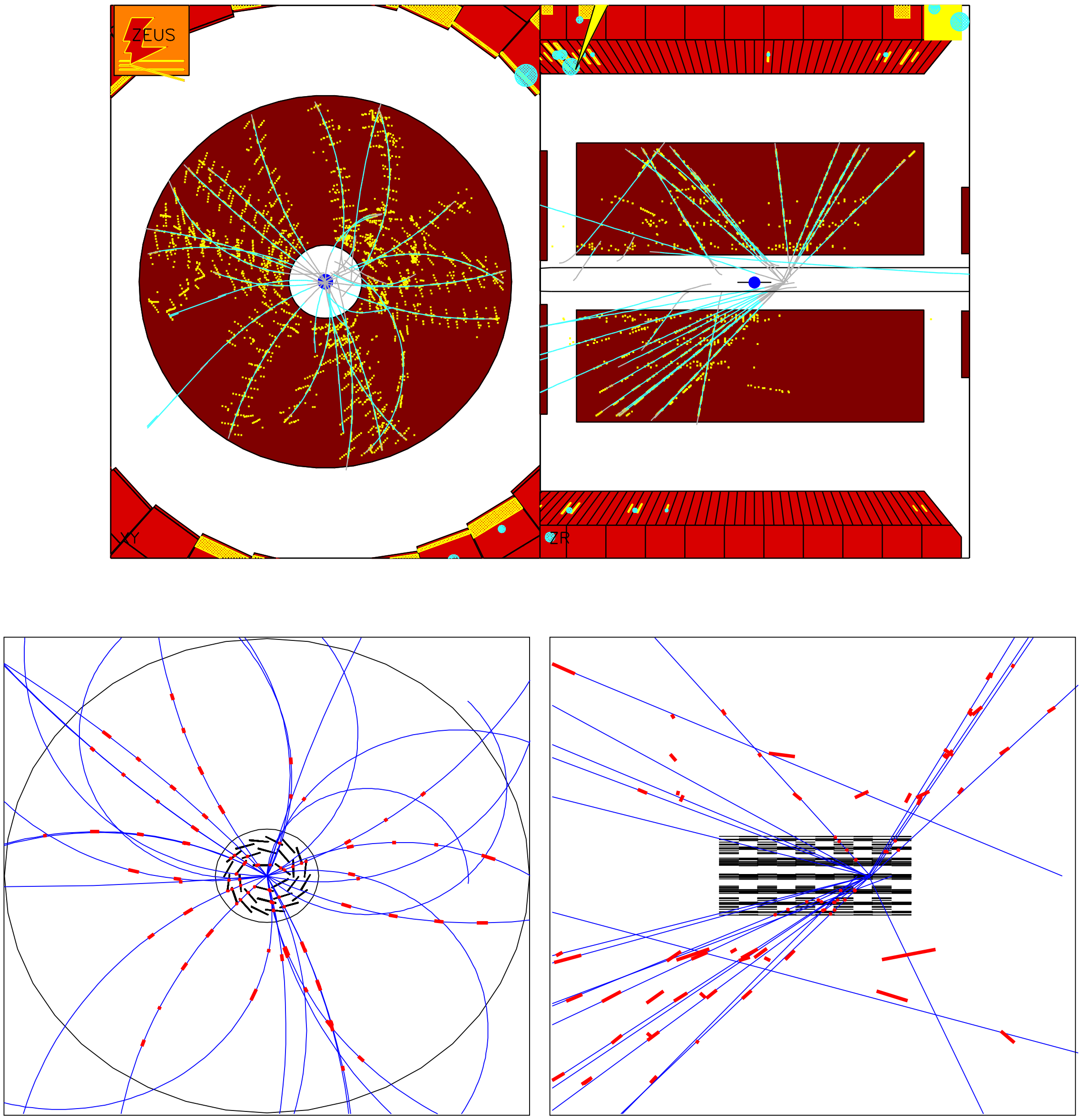

Figure 9.3: *Event displays showing the offline (upper) and GTT (lower) tracks for a busy MC event.*

9.3 Track resolutions

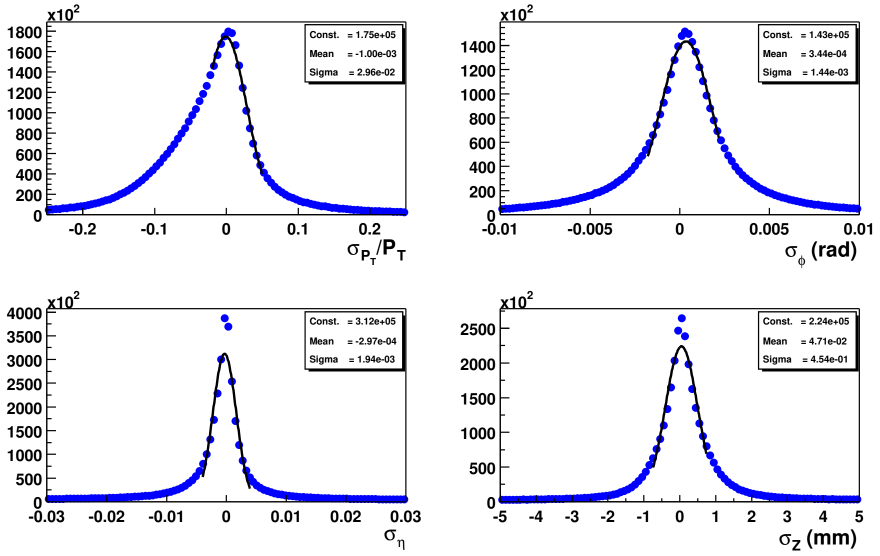

Figure 9.4: *p_T, ϕ, η, and z_{track} residuals for GTT tracks.*

The track resolutions for the reference sample defined above were determined using a Gaussian fit to the residual distributions, shown for GTT tracks in Figure 9.4, and are summarised in Table 9.1.

	σ_{p_T}/p_T	$\sigma_\phi(rad)$	σ_η	$\sigma_{z_{track}}$ (mm)
CTD-SLT	$6.64 \cdot 10^{-2}$	$3.90 \cdot 10^{-2}$	$1.83 \cdot 10^{-1}$	$1.24 \cdot 10^{2}$
GTT (CTD Only)	$3.08 \cdot 10^{-2}$	$5.67 \cdot 10^{-3}$	$2.47 \cdot 10^{-2}$	$1.40 \cdot 10^{1}$
Offline	$1.11 \cdot 10^{-2}$	$2.50 \cdot 10^{-3}$	$3.82 \cdot 10^{-3}$	$2.87 \cdot 10^{0}$
GTT	$2.96 \cdot 10^{-2}$	$1.44 \cdot 10^{-3}$	$1.94 \cdot 10^{-3}$	$4.54 \cdot 10^{-1}$

Table 9.1: *Table showing p_T, ϕ, η, and z_{track} resolutions for CTD-SLT, GTT, and offline tracks.*

By comparing the GTT (CTD Only) resolutions to those of the existing CTD-SLT improvements due to modifications of the CTD sections of the algorithm can be evaluated independently of any MVD based improvements. The GTT improves on the existing CTD-SLT in all variables. The improvement in p_T resolution is small, as would be expected since the r-ϕ portions of the algorithms are essentially identical. The difference is most likely due to the use of double precision arithmetic in the GTT and the removal of many of the data limits present in the existing CTD-SLT, resulting in approximately 25% more track candidates being found. The improvement in the ϕ resolution is a result of calculating ϕ from the fit parameters

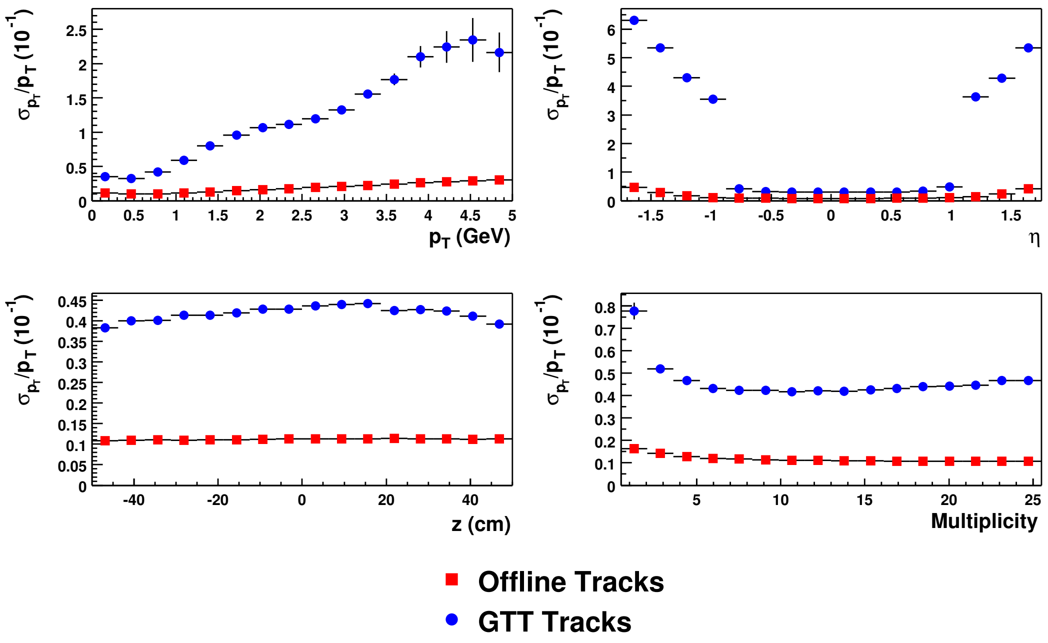

Figure 9.5: *p_T resolution as a function of p_T, η, z_{track}, and event multiplicity for GTT and offline tracks.*

rather than the outer segment, thus using all the available segment data in the calculation. The improvements in the η and z_{track} resolutions due to the use of stereo wire rather than z-by-timing data are almost an order of magnitude. This is in line with the expectations from hit resolutions of $\sigma_{z-by-timing} \approx 4$ cm and $\sigma_{z-by-stereo} \approx 2$ mm.

When MVD information is also included in the GTT there is a further improvement in resolution, with the GTT improving on the current offline values in all variables except p_T. These differences will now be studied in more detail.

9.3.1 p_T resolution

The GTT p_T resolution, shown in Figure 9.5, is largely unchanged by the inclusion of MVD hits. This can be easily understood by considering the p_T resolution of a hit at radius R. Since $\sigma_{p_T} \propto \sigma_R/R^2$ a CTD measurement with $\sigma_R \approx 180$ μm at $R \approx 80$ cm will be significantly more accurate than an MVD hit with $\sigma_R \approx 20$ μm at $R \approx 15$ cm and the p_T resolution will be dominated by the outermost CTD hits. This also explains the sharp drop in p_T resolution at $\eta = \pm 1$, outside which tracks will not pass through the outermost superlayer of the CTD, and the approximately linear increase of σ_{p_T}/p_T with p_T. At low values of p_T the resolution is limited by multiple scattering and the relation is no longer linear.

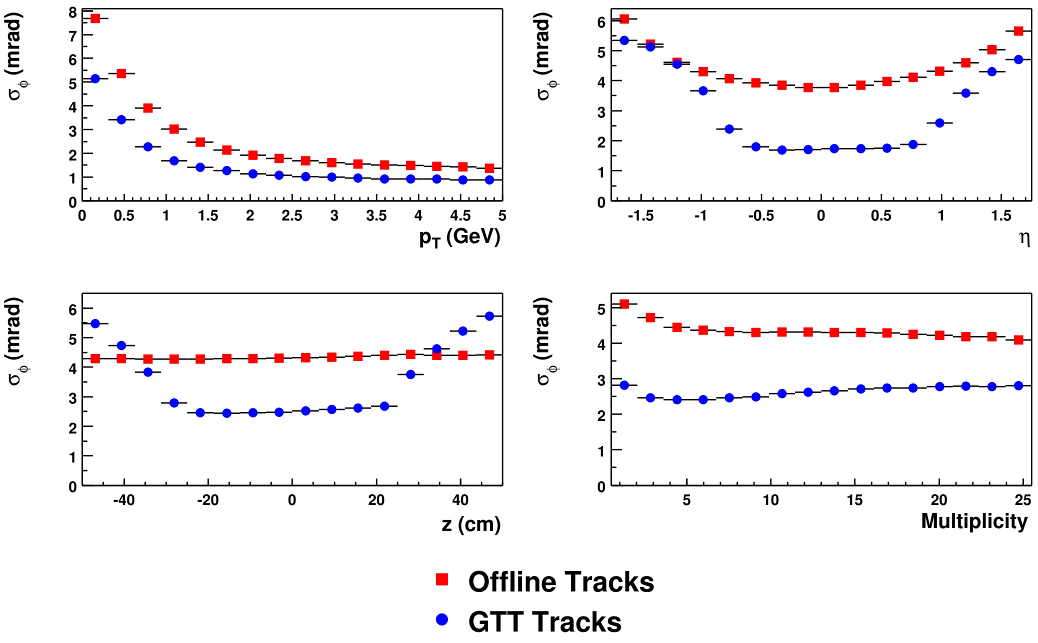

Figure 9.6: *ϕ resolution as a function of p_T, η, z_{track}, and event multiplicity for GTT and offline tracks.*

The GTT p_T resolution is significantly worse than the offline resolution as a result of the more simplistic approach used in the GTT. The two main differences are the number of hits (one per segment in the GTT and all in the offline algorithm) and the parameterisation (a circle in the GTT and a set of interlinked circles in the offline algorithm) used in the track fit. The resolution could then be improved by modifying the GTT algorithm to use more than just the central wire of a segment in the track fit, however this would require a significant rewrite of the CTD-SLT code used by the GTT.

9.3.2 ϕ resolution

The GTT ϕ resolution, shown in Figure 9.6, is significantly improved by the inclusion of MVD hits. The dependence of the GTT ϕ resolution on p_T follows the same trend as for the offline tracks. As p_T increases the tracks become straighter and ϕ varies less along the track, improving the accuracy of each measurement in determining ϕ at the origin. Like the GTT p_T resolution, the ϕ resolution also drops outside $\eta = \pm 1$, again corresponding to tracks with no hits in the outermost superlayer. The ϕ resolution also drops outside $z_{track} = \pm 30$ cm, corresponding to the physical size of the MVD. The GTT ϕ resolution is largely independent of the event multiplicity.

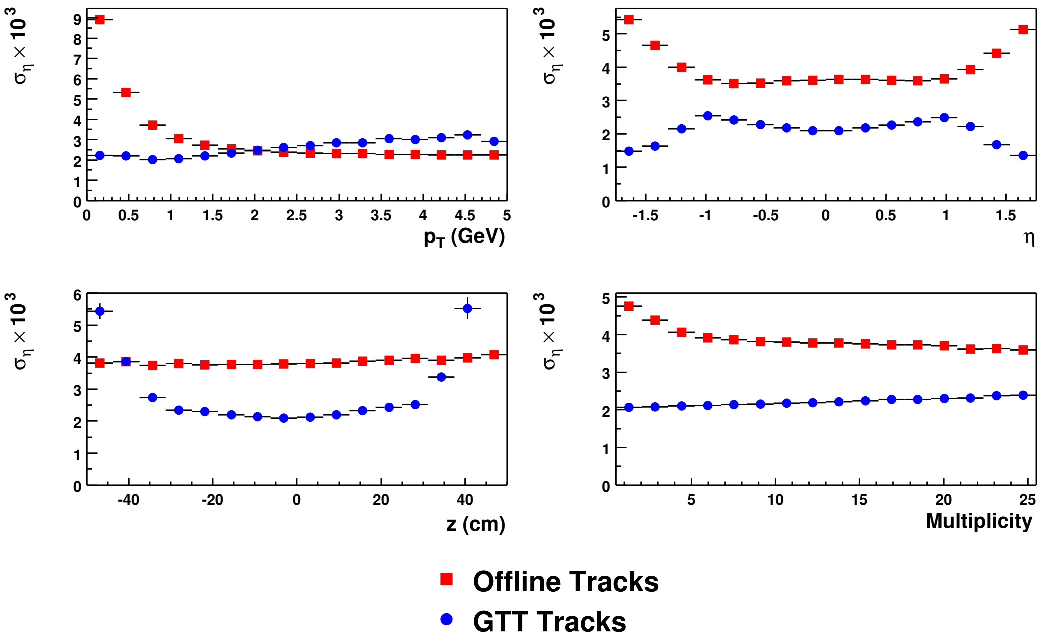

Figure 9.7: *η resolution as a function of p_T, η, z_{track}, and event multiplicity for GTT and offline tracks.*

9.3.3 η resolution

The GTT η resolution, shown in Figure 9.7, is significantly improved by the inclusion of MVD hits. The dependence of the GTT η resolution on p_T differs significantly than that for the offline tracks. This is probably a result of the significantly worse p_T resolution at higher values of p_T, degrading the performance of the stereo segment and MVD z hit matching. The dependence of the η resolution on η again changes significantly at $\eta = \pm 1$. However, in this case, the resolution *improves* when tracks have no hits in the outermost superlayer. This somewhat paradoxical behaviour occurs because a *reduction* in the CTD information will *increase* the dominance of the more accurate MVD information in the track fit. If the weight assigned to the MVD hits is increased this η dependence is reduced and the resolution improved, however the efficiency is reduced. The η resolution also drops outside $z_{track} = \pm 30$ cm, again corresponding to the physical size of the MVD. The GTT η resolution shows a slight degradation with increasing multiplicity.

9.3.4 z_{track} resolution

The GTT z_{track} resolution, shown in Figure 9.8, is significantly improved by the inclusion of MVD hits. It is approximately independent of p_T, suggesting that the MVD hits are dominating the resolution, unlike the η resolution which appears to

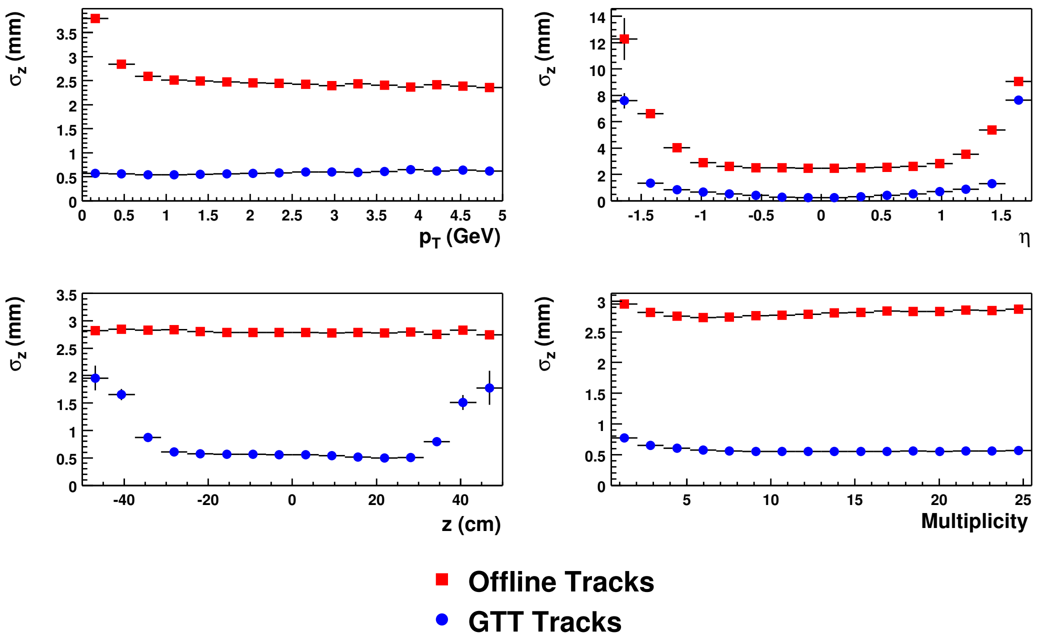

Figure 9.8: *z_{track} resolution as a function of p_T, η, z_{track}, and event multiplicity for GTT and offline tracks.*

be sensitive to both CTD and MVD effects. This is also apparent in the dependence on η and z_{track}. The z_{track} resolution drops at $\eta = \pm 1.5$ corresponding to the outer layer of the MVD. Once again, the resolution drops outside $z_{track} = \pm 30$ cm and is largely independent of the event multiplicity.

9.4 Track efficiency

The track finding efficiency for GTT and offline tracks, measured relative to the reference particles defined in Section 9.2, is shown in Figure 9.9. The difference in efficiency for positive and negative tracks at low p_T, due to the CTD cell geometry, can clearly be seen in both algorithms. The GTT has almost no efficiency below p_T =0.2 GeV, this is to be expected because the CTD-SLT was designed for high p_T tracks and is similarly inefficient at low p_T. Both algorithms reach their maximum efficiency, 60% for the GTT and 90% for the offline algorithm, at $p_T \approx 0.5$ GeV. Both algorithms decrease in efficiency with increasing values of $|\eta|$, where tracks will have hits in fewer layers. The most striking difference between the two algorithms is in the dependence of the efficiency on the event multiplicity. The offline algorithm is almost independent of the event multiplicity at values greater than 4. The GTT, however, decreases with increasing event multiplicity from 60% at low values to 40% at high

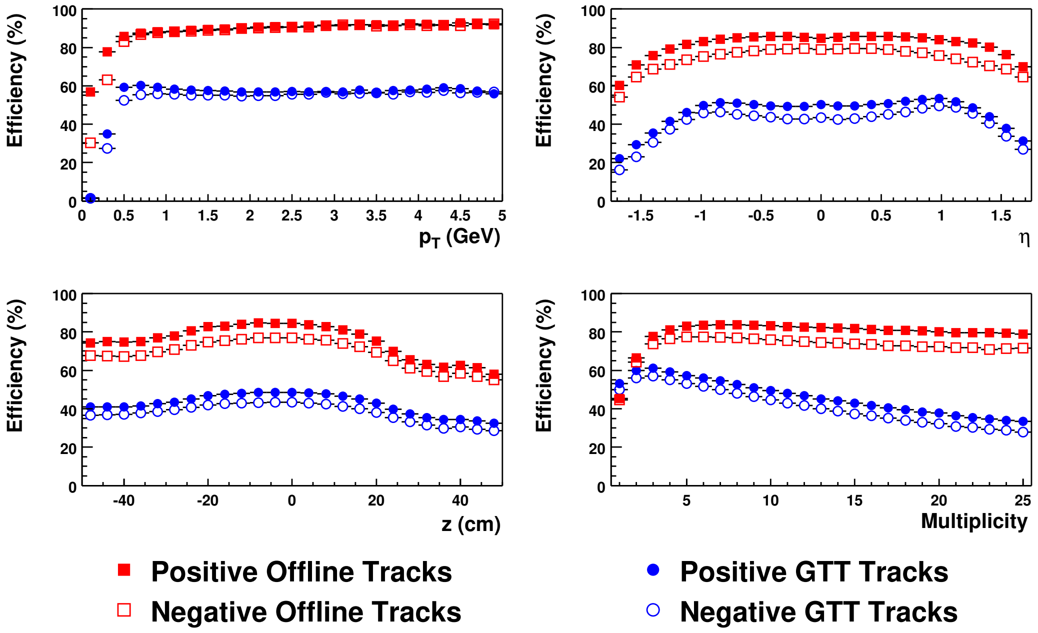

Figure 9.9: *Track finding efficiency as a function of p_T, η, z_{track}, and event multiplicity for GTT and offline tracks.*

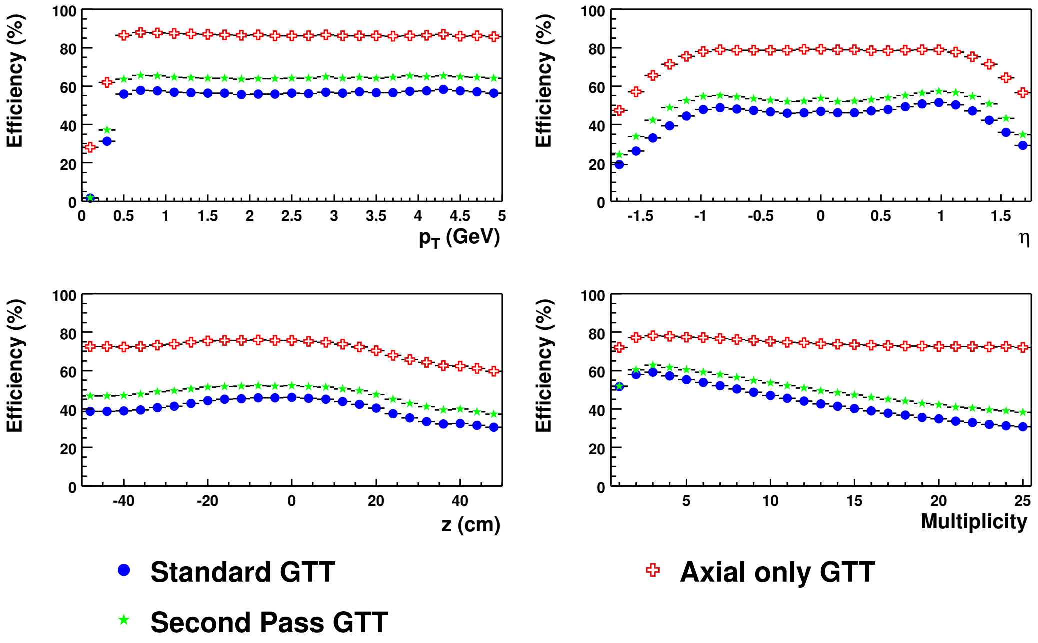

Figure 9.10: *Track finding efficiency as a function of p_T, η, z_{track}, and event multiplicity for axial GTT tracks and full GTT tracks with and without a second pass.*

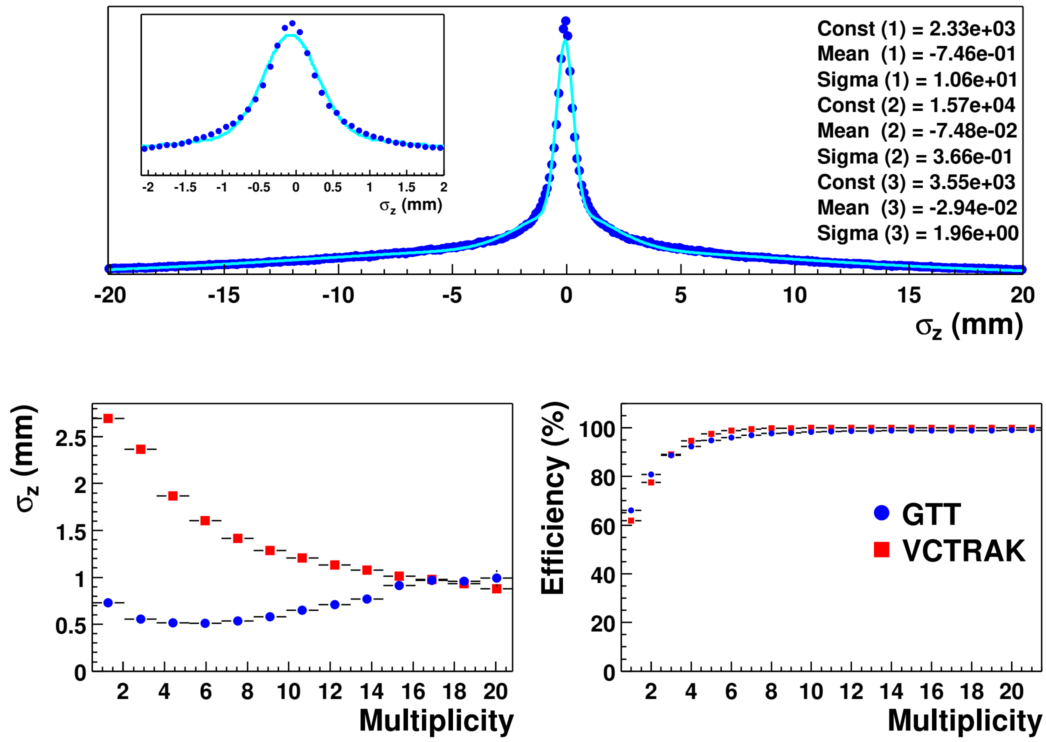

Figure 9.11: *GTT and offline event z_{vtx} resolution and efficiency.*

values. Since the individual resolutions were independent of event multiplicity, this suggests that the pattern recognition is less efficient at high multiplicities.

As can be seen from Figure 9.10, the axial track finding is very efficient, however, the efficiency for finding z-tracks is not as high as either the CTD-SLT or offline reconstruction. Both these algorithms have access to the CTD z-by-timing data which can significantly aid pattern recognition in the early stages of z-track finding. One way to improve the efficiency without access to the z-by-timing information, is to perform a second pass of the z-track finding, as discussed in Section 8.4.1. This increases the efficiency by $\approx 10\%$, as shown in Figure 9.10. This increase is independent of p_T, η, and z_{track} and is more significant for higher multiplicity events where the stereo matching is most vulnerable to mismatched segments.

9.5 Event vertex

The event vertex resolutions for the reference sample, determined from a single Gaussian fit to the residual distribution, are summarised in Table 9.2. The resolution of the GTT using only CTD information is significantly higher than that of the existing CTD-SLT reflecting the use of stereo layer rather than z-by-timing data.

	$\sigma_{z_{vtx}}$
CTD-SLT	$8.44 \cdot 10^1$
GTT (CTD Only)	$1.13 \cdot 10^1$
Offline	$1.14 \cdot 10^0$
GTT	$4.61 \cdot 10^{-1}$

Table 9.2: *Event z_{vtx} resolution for CTD-SLT, GTT, and offline algorithms.*

When MVD hits are included, the resolution can only be well described by a single Gaussian in the central region. However, it is reasonably well described across the whole range by the sum of three Gaussians, shown in Figure 9.11. The 1 cm wide Gaussian can be interpreted as being due to events whose vertex is dominated by the CTD resolution, and the 366 μm wide Gaussian to events whose vertex is dominated by the MVD resolution. Clearly, the total distribution will be some continuum between these two extremes, resulting in the non-Gaussian tails.

The variation of the resolution, again determined from a single Gaussian fit, with the event multiplicity is also shown. The offline resolution improves with increasing multiplicity, which is easily understood since each extra track adds another measurement of the event vertex to the fit. The GTT resolution, however, actually gets worse with increasing multiplicity, going from ≈0.5 mm at low multiplicities to ≈1 mm at high multiplicities, against this naive expectation. This is a result of the decrease in the pattern recognition performance with increasing multiplicity noted in the previous section. Thus, even though more tracks contribute to the event vertex fit they are, on average, less well measured, resulting in a poorer resolution.

By defining a reconstructed vertex as one which satisfies $\Delta z_{vtx} < 3 \cdot \sigma_{z_{vtx}}$ where $\sigma_{z_{vtx}}$ is taken from Table 9.2 and the GTT (CTD Only) value used to evaluate the GTT, the efficiency for reconstructing a vertex can be measured. The efficiency for both algorithms is ≈ 100% for events with 5 or more tracks.

9.6 Latency

The latency of the existing CTD-SLT has a mean of around 10 ms and a maximum of around 20 ms. If information from the GTT is to be included in the GSLT decision its latency must be no greater than these values. The latency consists of

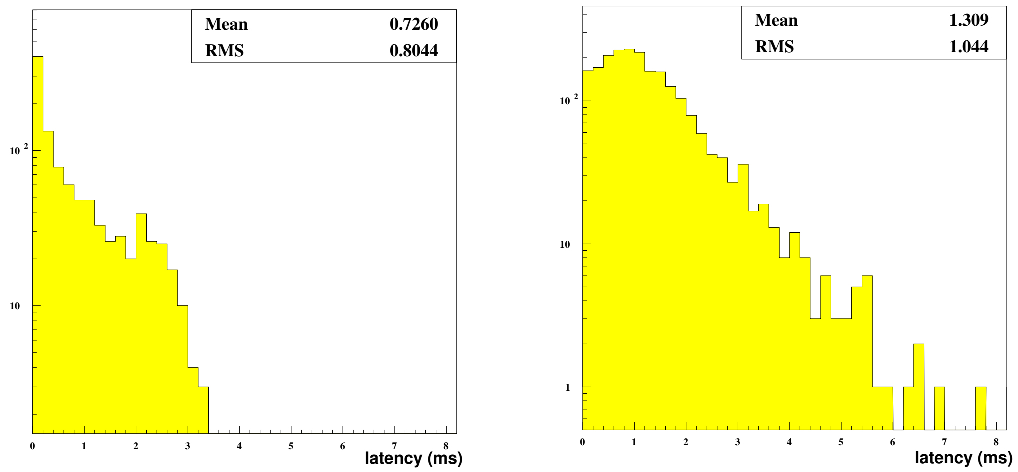

Figure 9.12: *The latency of the CTD only algorithm on data after a GFLT accept taken during the 2000 running period (left) and of the CTD+MVD algorithm on dijet Monte Carlo (right).*

two components, the processing latency (the time the algorithm takes to process the event) and the data transfer latency (the time taken to transfer the raw data from the components to the algorithm and the output from the algorithm to the GSLT). The expected data transfer latencies are around 3 ms for the CTD to GTT transfer, 1 ms for the MVD to GTT transfer, and 1 ms for the GTT to GSLT transfer [79].

A proper simulation of the event spectrum after a GFLT, including beam gas events, is difficult. As a result, the processing latency of the GTT has been estimated using one of the 1GHz GTT processors and a combination of real data taken at the end of 2000[1] and hard photoproduction Monte Carlo.

The processing latency distribution of the GTT algorithm for the real data is shown in Figure 9.12. This shows a mean processing latency of around 0.7 ms and a maximum of less than 4 ms. In order to estimate the possible latency performance for GFLT accepted events including MVD information, the latency for a sample of High E_T dijet Monte Carlo events has been measured using MVD hits from the simulation described in Section 9.1, also shown in Figure 9.12. This shows a mean processing latency of around 1.3 ms and a maximum of around 7 ms. Because this sample is biased, to larger, higher quality events where the average track multiplicity is higher the peak in the algorithm latency distribution lies at a longer latency. The total latency of the GTT is therefore expected to be well within that of the existing CTD-SLT.

[1] It should be noted that the running conditions at the end of 2000 were very favourable, and it is expected that the backgrounds at the start up of the upgraded HERA will be somewhat worse.

Part III

Summary

Charm and the virtual photon at HERA

The dependence of the virtual-photon induced production of dijets on the photon's virtuality, Q^2, has been studied for the first time in events containing a charm particle. The ratio of low to high x_γ^{obs} cross sections has been measured and is found to be consistent with being constant as a function of Q^2. In order to describe the ratio using LO pQCD it was necessary either to introduce a virtual photon structure when using DGLAP evolution or to use CCFM evolution. This is consistent with recent measurements of charm production in DIS from H1 which were best described by CCFM evolution.

The estimated $1\,\mathrm{fb}^{-1}$ which HERA is expected to deliver by 2005 will greatly increase the power of this measurement to distinguish between these two approaches. In the near future it is also expected that NLO DGLAP calculations for the ratio will become available. Since CASCADE claims that LO CCFM already includes some NLO DGLAP terms it will be interesting to see how these two approaches compare.

The ratio of the low to high x_γ^{obs} cross sections falls off much more slowly in the presence of charm than it does when charm is not required. This demonstrates for the first time that the previously observed suppressions of the low x_γ^{obs} cross section due to non-zero photon virtuality and due to charm are not independent.

A Global Tracking Trigger for ZEUS

The GTT algorithm has been described, and its performance evaluated for hard photoproduction events. The performance of the algorithm in terms of latency is promising. The resolution of tracks with MVD information has been shown to be significantly better than the current CTD-SLT and offline reconstruction. In addition, the primary vertex resolution is very good. The axial track finding is seen to be very efficient, however, because of the complexity involved in using the stereo information from the CTD, the efficiency for finding tracks in z is not as high as either the CTD-SLT or offline reconstruction, both of which have the advantage of being able to use the z-by-timing information from the CTD.

Modification to the existing CTD network to make the z-by-timing information available to the GTT should be seen as a high priority, when the algorithm has been seen to perform adequately with real data. Performing these modifications will take several weeks so could only take place during a reasonably long shutdown.

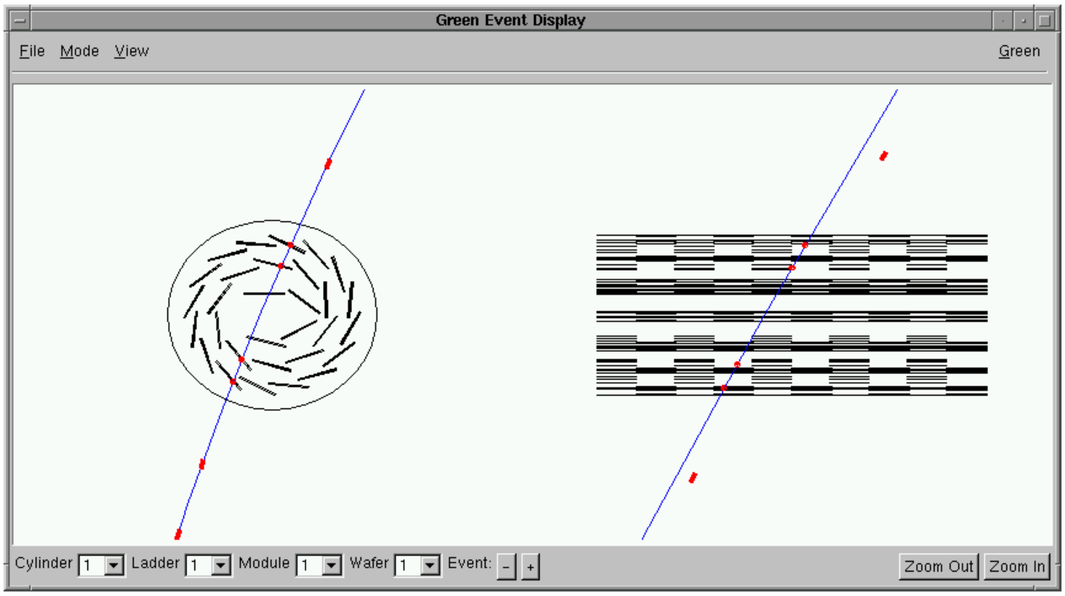

Figure 9.13: *A real cosmic event reconstructed by the GTT using CTD and MVD information in August 2001.*

The current CTD-SLT is reasonably efficient at rejecting beam gas events. It remains to be seen how the GTT algorithm will function in a beam gas environment including MVD information, although all indications are that it will function well (Figure 9.14). In this case, using the information from the GTT will prove to be a particularly useful addition to the ZEUS trigger chain.

Development of the GTT is a continuous process so it is envisaged that the algorithm eventually implemented when ZEUS starts to take data[2], will differ from that discussed here. As further studies progress and experience is gained with the latency performance further optimisation will be performed which may provide sufficient time for the additional stages of processing discussed, notably the second pass of z-track finding and secondary vertexing. In this latter case, the z-efficiency will be of particular importance, in order for the GTT to fulfill its very real potential for enhancing the efficiency of heavy flavour tagging in ZEUS.

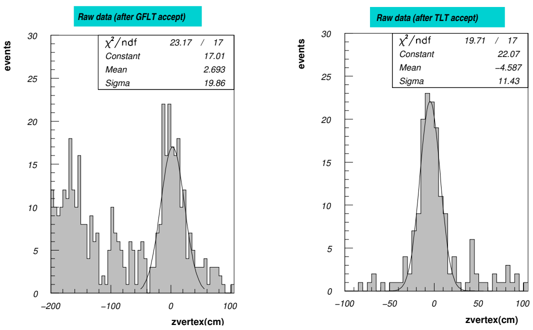

Figure 9.14: *GTT (CTD Only) event vertex distribution for real data after GFLT and TLT accepts. The beam-gas contribution can clearly be seen.*

[2]Cosmic events have already been reconstructed using the GTT, an example is shown in Figure 9.13.

Appendices

Appendix A

Monte Carlo event generators

There are numerous Monte Carlo event generators available, four of which were used in this thesis. The PYTHIA and HERWIG programs were used to generate events for use in the correction of the data for detector effects. The HERWIG, CASCADE and AROMA programs were used to generate LO pQCD predictions for the measured ratio. Since these programs have a great deal in common a brief, general, outline will be given and then the relevant differences in each program discussed.

The following, roughly time ordered description, taken from the PYTHIA manual, gives an outline of the processes that must be simulated in a typical high-energy event:

1. Initially two beam particles are coming in towards each other. Normally each particle is characterised by a set of parton distribution functions, which defines the partonic substructure in terms of flavour composition and energy sharing.
2. One shower initiator parton from each beam starts off a sequence of branchings, such as $q \rightarrow qg$, which build up an initial-state shower.
3. One incoming parton from each of the two showers enters the hard process, where then a number of outgoing partons are produced, usually two. It is the nature of this process that determines the main characteristics of the event.
4. Also the outgoing partons may branch, to build up final-state showers.
5. When a shower initiator is taken out of a beam particle, a beam remnant is left behind. This remnant may have an internal structure, and a net colour charge that relates it to the rest of the final state.
6. The QCD confinement mechanism ensures that the outgoing quarks and gluons are not observable, but instead fragment to colour neutral hadrons.

7. Many of the produced hadrons are unstable and decay further.

Within an event generator the elementary hard subprocess is generated first using exact matrix elements. In order to take account of higher order QCD effects the partons are allowed to shower through the branching processes $q \to qg$, $g \to gg$ and $g \to q\bar{q}$, described by evolution equations, until all partons are (essentially) on-shell. Finally, the partons must be combined into observable hadrons through hadronisation. This process cannot be described perturbatively and must be described by some phenomenoligical model.

A.1 HERWIG

HERWIG (Hadron Emission With Interfering Gluons) [53] is a general-purpose event generator for high-energy processes, with particular emphasis on the detailed simulation of QCD parton showers. The factorisation scale for the hard sub-process, μ^2, is given by,

$$\mu^2 = \frac{2\hat{s}\hat{t}\hat{u}}{\hat{s}^2 + \hat{t}^2 + \hat{u}^2},$$

where, $\hat{s}, \hat{t}$ and $\hat{u}$ are the Mandelstam variables. The resultant cross section is divergent in the limit of transverse momentum of the outgoing partons, $\hat{p}_T^2 \to 0$, so a minimum transverse momentum cut, $\hat{p}_T^{min}$, is introduced.

Final-state parton showering is generated by a "coherent branching algorithm". The energy fractions are distributed according to the DGLAP splitting functions and partons are ordered in terms of their opening angle. The ordering is continued until the hadronisation scale is of the order of the lightest mesons.

Initial-state parton showering is handled within the "backwards evolution" scheme. It proceeds from the elementary subprocess at a hard scale set by colour coherence, back to the hadron scale, Q_0. The showering is again generated through coherent branching however, the angular ordering now applies to the angles between the direction of the incoming hadron and the emitted parton.

The transition from partons to hadrons after the parton shower proceeds via a non-perturbative model called the "cluster" model, which groups the partons into colour neutral objects. The gluons are split into $q\bar{q}$ pairs and these are subsequently clustered into colourless objects via the colour connections generated in the parton shower. Each cluster is then fragmented into two hadrons or the lightest hadron for its flavour if the cluster is not massive enough.

HERWIG version 6.1 was used in this thesis.

A.2 PYTHIA

The PYTHIA Monte Carlo [52] is also a general purpose generator, sharing many common features with HERWIG, but also significant differences. The factorisation scale, μ^2, used is the transverse mass of the two outgoing partons, m_T^2, given by,

$$\mu^2 = m_T^2 = \frac{1}{2}\left(m_1^2 + p_{T_1}^2 + m_2^2 + p_{T_2}^2\right).$$

The parton shower is conceptually the same as in HERWIG, but in PYTHIA the evolution is ordered in the virtuality of the radiated partons.

The partons are hadronised using the Lund Symmetric String Fragmentation model [80] implemented in JETSET. In the Lund model, partons are connected by "strings", the strength of which is about 1 GeV/fm. As the partons move away from each other, the strings become more energetic, finally breaking to produce $q\bar{q}$ pairs. When the energy of a string is too small to enable further separation of the partons, hadrons are formed.

PYTHIA version 6.1 was used in this thesis.

A.3 AROMA

The AROMA Monte Carlo [81] is a heavy flavour adaptation of the deep inelastic scattering Monte Carlo LEPTO [82]. The complete matrix elements, to order $\alpha^2\alpha_s$, for the BGF process (including the masses of the produced heavy quarks and the full electroweak structure of the interaction) are used to generate the hard subprocess. The parton showers and hadronisation are effectively the same as is implemented in PYTHIA.

AROMA version 2.2 was used in this thesis.

A.4 CASCADE

The CASCADE Monte Carlo [83] is the first event generator to implement the CCFM evolution equation for the initial state cascade in a backward evolution approach (all the above generators use the DGLAP equation). The hard scattering process is generated according to the k_T factorisation theorem [18]:

$$\sigma = \int dk_T^2 dx_g \mathcal{A}(x_g, k_T^2, \bar{q}) \sigma(\gamma^* g^* \to q\bar{q}) \tag{A.1}$$

where $\mathcal{A}(x_g, k_T^2, \bar{q})$ is the unintegrated gluon density, obtained from a fit to F_2.

Initial state parton showers are generated according to the CCFM equation in a backward evolution approach. The initial state parton shower consists only of gluon branchings and is generated in an angular ordered region in the laboratory frame. All the parameters (like the scale μ in α_s, the collinear cut-off Q_0, and the cut-off for the parton shower) in the initial state parton shower are fixed by the unintegrated gluon density.

Final state parton showers are generated using the same routines as in PYTHIA and the hadronisation is performed using the Lund string fragmentation implemented in JETSET.

CASCADE version 1.0 was used in this thesis.

Appendix B

Derivation of Errors

The purity, p, efficiency, ϵ, and correction factor, C, were defined in Section 5.3 in terms of the number of events generated in a bin, t, the number of events measured in a bin, m, and the number of events both generated and measured in a bin, u. These variables make the interpretation of these quantities clear, however, they are not statistically independent. In order to calculate the errors on these quantities, correctly taking into account these correlations, the problem is recast in terms of statistically independent variables a, b and c. Where a is the number of events generated and measured in the same bin, b is the number of events generated in the bin but not detected in it, and c is the number of events not generated in the bin but detected in it. Thus:

$$t = a + b \ \ ; \ \ m = a + c \ \ ; \ \ u = a \ \ ;$$

and

$$p = \frac{a}{a+c};$$

$$\epsilon = \frac{a}{a+b};$$

$$C = \frac{a+b}{a+c}.$$

B.1 Purity

The error on the purity is then given by:

$$\begin{aligned}\delta p^2 &= \left(\frac{\delta p}{\delta a}\right)^2 \cdot V_a + \left(\frac{\delta p}{\delta c}\right)^2 \cdot V_c \\ &= \left[\frac{1}{a+c} - \frac{a}{(a+c)^2}\right]^2 \cdot V_a + \left[\frac{a}{(a+c)^2}\right]^2 \cdot V_c \\ &= \frac{c^2 \cdot V_a^2 + a^2 \cdot V_c}{(a+c)^4},\end{aligned}$$

where V_a is the variance of the mean of a. Rewriting this in terms of the original variables gives:

$$\delta p = \sqrt{\frac{m^2 \cdot V_u + u^2 \cdot V_m - 2 \cdot m \cdot u \cdot V_u}{m^4}}. \tag{B.1}$$

When the events are weighted, as in this thesis, the numbers of events in, for example, the sample m is given by the sum of the weights, $\sum w_i(m)$, and the variance, V_m, is given by $\sum w_i(m)^2$. [1] For unweighted events this reduces to the more commonly given form:

$$\delta p = \sqrt{\frac{(1-p) \cdot p}{m}}.$$

B.2 Efficiency

Similarly, the error on the efficiency is given by:

$$\delta \epsilon = \sqrt{\frac{t^2 \cdot V_u + u^2 \cdot V_t - 2 \cdot t \cdot u \cdot V_u}{t^4}}, \tag{B.2}$$

which for unweighted events again reduces to the more commonly given form:

$$\delta \epsilon = \sqrt{\frac{(1-\epsilon) \cdot \epsilon}{t}}.$$

B.3 Correction factor

Finally, the error on the correction factor is given by:

[1] The variance of a sum of weights from Poisson sources is $\sum_i w_i^2$.

$$\begin{aligned}
\delta C^2 &= \left(\frac{\delta p}{\delta a}\right)^2 \cdot V_a + \left(\frac{\delta p}{\delta b}\right)^2 \cdot V_b + \left(\frac{\delta p}{\delta c}\right)^2 \cdot V_c \\
&= \left[\frac{1}{a+c} - \frac{a+b}{(a+c)^2}\right]^2 \cdot V_a + \left[\frac{1}{a+c}\right]^2 \cdot V_b + \left[\frac{a+b}{(a+c)^2}\right]^2 \cdot V_b \\
&= \frac{(c-b)^2 \cdot V_a + (a+c)^2 \cdot V_b + (a+b)^2 \cdot V_c}{(a+c)^4}.
\end{aligned}$$

Which, in terms of the original variables, is:

$$\delta C = \sqrt{\frac{m^2 \cdot V_t + t^2 \cdot V_m - 2 \cdot m \cdot t \cdot V_u}{m^4}}. \tag{B.3}$$

For unweighted events this again reduces to the more commonly given form:

$$\delta C = \sqrt{\frac{t}{m^3}[t + m - 2 \cdot u]}.$$

Appendix C

Maths of the GTT algorithm

The mathematical details of the fits used in the GTT algorithm will now be described.

C.1 Constrained r-ϕ track fit

The fit is formally the same as for the existing CTD-SLT, however, it has been reformulated in terms of x and y (rather than r and ϕ) since these sums can then also be used for an unconstrained circle fit without recalculation.

The circle radius is calculated using

$$R_0^2 = \frac{(b^2+e^2)c^2 + (a^2+e^2)d^2 - 2cdef}{4(ab-e^2)^2} \tag{C.1}$$

where the variables a, b, c, d, e and f are calculated summing over the axial segments, i, with positions x_i, y_i, radii r_i and polar angle ϕ_i

$$\begin{aligned} a &= \sum_i x_i^2, & b &= \sum_i y_i^2, \\ c &= \sum_i r_i^2 x_i, & d &= \sum_i r_i^2 y_i, \\ e &= \sum_i x_i y_i, & f &= \sum_i r_i^2. \end{aligned} \tag{C.2}$$

The circle centre is obtained using

$$\begin{aligned} x_0 &= \frac{bc-ed}{2(ab-e^2)}, \\ y_0 &= \frac{ad-ec}{2(ab-e^2)}. \end{aligned} \tag{C.3}$$

The track charge is then obtained using the sign of the cross product of the circle centre and the position of the outermost axial segment, and the track polar angle ϕ_h at the origin obtained by the perpendicular in the x-y plane to the circle centre.

C.2 Unconstrained r-ϕ track fit

In this case the circle centre is calculated first using

$$\begin{aligned} x_0 &= \frac{C_2 B_2 - C_1 B}{B_2^2 - AB}, \\ y_0 &= \frac{C_1 B_2 - C_2 A}{B_2^2 - AB} \end{aligned} \tag{C.4}$$

where

$$\begin{aligned} A = a - \frac{g^2}{w}, &\qquad B = b - \frac{h^2}{w}, \\ B_2 &= e - \frac{gh}{w}, \\ C_1 = \frac{1}{2}\left[m + p - \frac{gf}{w}\right], &\qquad C_2 = \frac{1}{2}\left[n + q - \frac{hf}{w}\right], \end{aligned} \tag{C.5}$$

a-f are defined in equation (C.2) and g, h, m, n, p and q are defined as

$$\begin{aligned} g = \sum_i x_i, &\qquad h = \sum_i y_i, \\ m = \sum_i x_i^3, &\qquad n = \sum_i y_i^3, \\ p = \sum_i y_i^2 x_i, &\qquad q = \sum_i x_i^2 y_i \end{aligned} \tag{C.6}$$

with w being the sum of the weights

$$w = \sum_i w_i. \tag{C.7}$$

The circle radius is then calculated using

$$R_0^2 = x_0^2 + y_0^2 + \frac{a + b - 2(x_0 g + y_0 h)}{w}. \tag{C.8}$$

The track charge and polar angle ϕ_h calculated as before.

C.3 Intersection of an axial track with a stereo wire in z-s

The calculation of the intersection of an r-ϕ track with a stereo wire hit is performed using the same algorithm as VCTRAK [78]. Before the algorithm itself is explained it is first necessary to define the variables used in it.

CTD hits and coordinates

Each sense wire in a stereo layer L runs at a small angle α_L w.r.t. the z direction. In general, the location in the x-y plane of a sense wire, $\vec{r}$, is:

$$\vec{r} = \vec{r}_{SW} + (z - z_{CTD})\vec{r}\,'_{SW} \tag{C.9}$$

where z_{CTD} is the nominal centre of the CTD ($\vec{r}_{CTD} = (0, 0, 2.5)$ cm), $\vec{r}_{SW}$ is the position at $z = z_{CTD}$ and

$$\vec{r}\,'_{SW} = (-\sin\,\phi_{SW}\,\tan\,\alpha_L + \cos\,\phi_{SW}\,\tan\,\alpha_L) \tag{C.10}$$

where $\phi_{SW} = tan^{-1}\frac{y_{SW}}{x_{SW}}$.

Each CTD hit is a drift time from the raw data, t_m, which is converted into a drift distance, d_m, using the linear calibration constants v_d, the global drift velocity, and t_0, the global "time zero"[1]:

$$d_m = v_d(t_m - t_0). \tag{C.11}$$

A "planar drift approximation" in which the ionisation electrons drift parallel to $\vec{p}$ is used to determine positions in space where

$$\vec{p} = \hat{p}_{SW} + (z - z_{CTD})\vec{p}\,'_{SW}. \tag{C.12}$$

The unit vector, $\vec{p}\,'_{SW}$, is shared by all eight sense wires in the same cell, and is the nominal design value. Drift distances are then measured along the "planar drift" measurement axis, $\hat{m}$, obtained by rotating $\vec{p}$ through $+90°$:

$$\begin{aligned} m_x &= -p_y/|p| \\ m_y &= +p_x/|p| \end{aligned} \tag{C.13}$$

[1] In VCTRAK each individual sense wire is assigned its own t_0.

Each measurement d_m then yields two positions in the x-y plane, one on either side of the sense wire:

$$\vec{r}_m = \vec{r} \pm s_m \hat{m} \tag{C.14}$$

Calculation of the intersection

Iteration is used to estimate z_m. That is, starting from a current estimate $\tilde{z}_m$, an improved estimate z_m is calculated.

First the location of the hit, $\vec{r}_m$, is estimated at $\tilde{z}_m = z_{CTD}$ as follows:

$$\begin{aligned}
\vec{r} &= \vec{r}_{SW} + (\tilde{z}_m - z_{CTD})\vec{r}\,'_{SW} \\
\vec{p} &= \hat{p}_{SW} + (\tilde{z}_m - z_{CTD})\vec{p}\,'_{SW} \\
\hat{p} &= (p_x, p_y)/|\vec{p}| \\
\hat{m} &= (-p_y, p_x)/|\vec{p}| \\
\vec{r}_m &= \vec{r} + d_m \hat{m} \\
&\equiv (x_m, y_m)
\end{aligned}$$

Next the intersection of a line with a circle is solved. The line is the measurement axis through the measurement (i.e. $\hat{m}$ through $\vec{r}_m$). The circle is the axial track with radius R, charge Q, polar angle ϕ_h and centre $\vec{C} = (x_c, y_c)$. The line cuts the circle in two places given by:

$$\begin{aligned}
h &= (\vec{r}_m - \vec{C}) \cdot \hat{p} \\
l &= \pm\sqrt{R^2 - h^2} \\
\vec{P} &= \vec{C} + h\hat{p} + l\hat{m}
\end{aligned}$$

Here, h and l form a right angle triangle with hypotenuse R. The desired solution, $\vec{P}$, is chosen to be the one closest to $\vec{r}_m$.

The stereo measurement is the assumed to lie on the circle at the new estimate z_m:

$$\vec{r}_{SW} + (z_m - z_{CTD})\vec{r}\,'_{SW} + d_m\hat{m} \approx \vec{P}$$

and the solution obtained by taking the dot product on either side with $\vec{r}\,'_{SW}$:

$$z_m \approx z_{CTD} + (\vec{P} - \vec{r}_{SW} - d_m\hat{m}) \cdot \vec{r}\,'_{SW}/(\vec{r}\,'_{SW} \cdot \vec{r}\,'_{SW})$$

Iterations are performed because $\hat{m}$ and $\vec{P}$ were evaluated at $z = \tilde{z}_m$. Specifically, if $|z_m - \tilde{z}_m| > 0.05$ cm, then z_m becomes the next $\tilde{z}_m$, and another iteration is done. Convergence is quite good because the z-dependence of the sense wire ($\vec{r}\,'_{SW}$) is roughly parallel to the planar drift measurement axis ($\hat{m}$).

With (x_m, y_m, z_m) now available, the 2D path length s_m is easily obtained using

$$\begin{aligned} \phi_m &= \text{atan2}(-Q(x_m - x_c), +Q(y_m - y_c)), \\ s_m &= s(\phi_m) = -QR(\phi_m - \phi_h). \end{aligned}$$

References

[1] ZEUS Coll., U. Holm (ed.), *The ZEUS Detector.* Status Report (unpublished), DESY, 1993, available on `http://www-zeus.desy.de/bluebook/bluebook.html`.

[2] N. Harnew et al., Nucl. Inst. Meth. **A 279**, 290 (1989); B. Foster et al., Nucl. Phys. Proc. Suppl. **B 32**, 181 (1993); B. Foster et al., Nucl. Inst. Meth. **A 338**, 254 (1994).

[3] R. Hall-Wilton et al., *The CTD Tracking Resolution* (unpublished). ZEUS-99-024, 1999.

[4] M. Derrick et al., Nucl. Inst. Meth. **A 309**, 77 (1991); A. Andresen et al., Nucl. Inst. Meth. **A 309**, 101 (1991); A. Caldwell et al., Nucl. Inst. Meth. **A 321**, 356 (1992); A. Bernstein et al., Nucl. Inst. Meth. **A 336**, 23 (1993).

[5] A. Bamberger et al., Nucl. Inst. Meth. **A 382**, 419 (1996).

[6] A. Bamberger et al., Nucl. Inst. Meth. **A 401**, 63 (1997).

[7] ZEUS Coll., R. Carlin et al., Nucl. Inst. Meth. **A 379**, 542 (1996).

[8] H. Abramowicz and A. Caldwell, Rev. Mod. Phys. **71**, 1275 (1999).

[9] R.K. Ellis, W.J. Stirling and B.R. Webber, *QCD and Collider Physics*, Cambridge Monographs on Particle Physics, Nuclear Physics and Cosmology, Vol. 8. Cambridge University Press, 1996.

[10] J. Friedman et al., Phys. Rev. **D 5**, 528 (1972).

[11] R. P. Feynman, Phys. Rev. Lett. **23**, 1415 (1969).

[12] H. E. Fisk and F. Sciulli, Ann. Rev. Nucl. Part. Sci. **32**, 499 (1982).

[13] T. Eichten et al., Phys. Lett. **B 46**, 274 (1973).

[14] TASSO Coll., R. Brandelik et al., Phys. Lett. **B86**, 243 (1979).

[15] ZEUS Coll., J. Breitweg et al., *Measurement of the neutral current cross section and F_2 structure function for deep inelastic e^+p scattering at HERA*, 2001. Submitted to Eur. Phys. J. C.

[16] J. C. Collins, D. E. Soper and G. Sterman, Nucl. Phys. **B 261**, 104 (1985).

[17] V.N. Gribov and L.N. Lipatov, Sov. J. Nucl. Phys. **15**, 438 (1972);
Yu.L. Dokshitzer, Sov. Phys. JETP **46**, 641 (1977);
G. Altarelli and G. Parisi, Nucl. Phys. **B 126**, 298 (1977).

[18] S. Catani, M Ciofaloni and F. Hautmann, Nucl. Phys. **B366**, 135 (1991).

[19] I. I. Balitsky and L.N. Lipatov, Sov. J. Nucl. Phys. **28**, 822 (1978);
E.A. Kuraev, L.N. Lipatov and V.S. Fadin, Sov. Phys. JETP **44**, 443 (1976).

[20] M. Ciafaloni, Nucl. Phys. **B 296**, 49 (1988);
S. Catani, F. Fiorani and G. Marchesini, Nucl. Phys. **B 336**, 18 (1990).

[21] C. F. von Weizsacker, Z. Phys. **88**, 612 (1934);
E.J. Williams, Phys. Rev. **45**, 729 (1934).

[22] ZEUS Coll., J. Breitweg et al., Eur. Phys. J. **C 1**, 109 (1998).

[23] JADE Coll., W. Bartel et al.., Z. Phys. **C 24** (1984);
TASSO Coll., M. Althoff et al.., Z. Phys. **C 31** (1986);
TPC/Two-Gamma Coll., H. Aihara et al., Z. Phys. **C 34** (1987);
L3 Coll., M. Acciarri et al., Phys. Lett. **B 436** (1998);
ALEPH Coll., R. Barate et al., Comp. Phys. Comm. **B 458** (1999);
L3 Coll., M. Acciarri et al., Phys. Lett. **B 447** (1999);
L3 Coll., M. Acciarri et al., Phys. Lett. **B 453** (1999).

[24] R. J. De Witt, L. M. Jones, J. D. Sullivan, D. E. Willen, H. W. Wyld, Phys. Rev. **D 19**, 2046 (1979).

[25] G. A. Schuler and T. Sjöstrand, Z. Phys. **C 68**, 607 (1995).

[26] G. A. Schuler and T. Sjöstrand, Phys. Lett. **B 376**, 193 (1996).

[27] PLUTO Coll., C. Berger et al.., Nucl. Phys. **B 281**, 365 (1987).

[28] L3 Coll., M. Acciarri et al., Phys. Lett. **B 483** (2000).

[29] OPAL Coll., *Measurement of the Cross-Section of Double-Tagged Events in Two-Photon Collisions at LEP.* Abstract 48, EPS 2001, Budapest, Hungary.

[30] ZEUS Coll., J. Breitweg et al., Phys. Lett. **B 479**, 37 (2000);
ZEUS Coll., *Differential dijet cross sections in γp interactions at HERA.* Abstract 1039, ICHEP 2000, Osaka, Japan.

[31] ZEUS Coll., *The Q^2 and $\overline{E}_T^2$ dependence of dijet cross sections in $\gamma^* p$ interactions at HERA.* Abstract 636, EPS 2001, Budapest, Hungary.

[32] H1 Coll., C. Adloff et al., Phys. Lett. **B 415**, 418 (1997);
H1 Coll., C. Adloff et al., Eur. Phys. J. **C 13**, 397 (2000).

[33] H. L. Lai and W. K. Tung, Z. Phys. **C 74**, 463 (1997).

[34] S. Frixione, M.L. Mangano, P. Nason, and G. Ridolfi, Preprint hep-ph/9702287, 1997.

[35] ZEUS Coll., J. Breitweg et al., Phys. Lett. **B 407**, 402 (1997);
H1 Coll., C. Adloff et al., Z. Phys. **C 72**, 593 (1996).

[36] ZEUS Coll., J. Breitweg et al., Eur. Phys. J. **C 12**, 35 (2000).

[37] ZEUS Coll., J. Breitweg et al., Phys. Lett. **B 401**, 192 (1997).

[38] S.P. Baranov et al., in *Proc. Workshop on Physics at HERA*, eds. W. Buchmüller and G. Ingelman, Vol. 3, p. 1478. DESY, Hamburg, Germany, 1991.

[39] F. Jacquet and A. Blondel, in *Proceedings of the Study for an ep Facility for Europe*, ed. U. Amaldi, p. 391. Hamburg, Germany, 1979. Also in preprint DESY 79/48.

[40] S. Catani et al., Nucl. Phys. **B 406** (1993).

[41] J.M. Butterworth, L. Feld, M. Klasen and G. Kramer, *Matching Experimental and Theoretical Jet Definitions for Photoproduction at HERA.* Proceedings of the Workshop “Future Physics at HERA”, 554 (1996).

[42] J.E. Huth et al., in *Research Directions for the Decade. Proceedings of Summer Study on High Energy Physics, 1990*, ed. E.L. Berger, p. 134. World Scientific, 1992. Also in preprint FERMILAB-CONF-90-249-E.

[43] M. Seymour, Preprint hep-ph/9707349, 1997.

[44] S.D. Ellis and D.E. Soper, Phys. Rev. **D 48**, 3160 (1993).

[45] R. Saunders, *A Measurement of Dijet Photoproduction at HERA using the ZEUS Detector.* PhD, UCL, 1997;
L. Feld, *Messung von Zweijet-Wirkungsquerschnitten in Photoproduktion an HERA.* PhD, Bonn, 1996.

[46] M. Sutton, *Charm in Dijet Photoproduction at HERA.* PhD, UCL, 1998.

[47] A. Savin, *Study of Calorimeter Noise in the 1996 data* (unpublished). ZEUS-98-007.

[48] J. Repond, *Jet Energy Corrections* (unpublished). ZEUS-96-104.

[49] M. Wodarczyk, *Measurement of the F_2 Structure Function of the Proton at HERA from 1996 and 1997 ZEUS Data.* PhD, Wisconsin, 1999.

[50] H. Abramowicz, A. Caldwell, R. Sinkus, *Neural Network Based Electron Identification in the ZEUS Calorimeter.* DESY-95-054.

[51] Nussinov, S., Phys. Rev. Lett. **35**, 1672 (1975).

[52] T. Sjöstrand et al., Comp. Phys. Comm. **135**, 238 (2001).

[53] G. Marchesini et al., Comp. Phys. Comm. **67**, 465 (1992).

[54] R. Brun et al., GEANT3, Technical Report CERN-DD/EE/84-1, CERN, 1987.

[55] A.D. Martin, R.G. Roberts and W.J. Stirling, Phys. Rev. **D 50**, 6734 (1994).

[56] Particle Data Group, D.E. Groom et al., Eur. Phys. J. **C15**, 1 (2000).

[57] ZEUS Coll., M. Derrick et al., Phys. Lett. **B 342**, 417 (1995);
ZEUS Coll., M. Derrick et al., Phys. Lett. **B 348**, 665 (1995).

[58] N. Macdonald, *Structure of the Virtual Photon at HERA.* Ph.D. Thesis, Glasgow, 1999.

[59] H. Jung, *Heavy Quark production at HERA in k_t factorization supplemented with CCFM evolution.* Talk given to Photon 2001, Ascona, Switzerland.

[60] H. Jung, Comp. Phys. Comm. **86**, 147 (1995).

[61] H1 Coll., *Measurement of $D^{*\pm}$ Meson Production and the Charm Contribution to the Proton Structure Function F_2^c in Deep Inelastic Scattering at HERA* (unpublished). Abstract 984, ICHEP2000, Osaka, Japan.

[62] G. Wolf, *Deep Inelastic Scattering at Large Energy and Momentum Transfers: Recent Results from the HERA Collider*, DESY-01-058.

[63] ZEUS Coll., *Dijet angular distributions in D^* photoproduction at HERA*, 1999. Abstract 499, EPS 2001, Budapest, Hungary.

[64] ZEUS Coll., J. Breitweg et al., Eur. Phys. J. **c18** (2001).

[65] CDF Coll., F. Abe et al., Phys. Rev. **D 50**, 4252 (1994);
D0 Coll., S. Abachi et al., Phys. Lett. **B370**, 239 (1996).

[66] *Future Physics at HERA Volumes I and II*, ed. G. Ingelman, A. De Roeck, R. Klanner, 1996.

[67] M. Seidel, *The Upgraded Interaction Regions of HERA* (unpublished). DESY-HERA-00-01.

[68] Zeus Coll., *A Straw-Tube Tracker for ZEUS* (unpublished). ZEUS-98-046.

[69] Zeus Coll., *A Microvertex Detector for ZEUS* (unpublished). ZEUS-97-006.

[70] The ZEUS MVD Group, *Mechanical Design and Construction of the ZEUS Micro Vertex Detector* (unpublished). ZEUS-00-028.

[71] D. Daneheim, *The Silicon Strip Detectors of the ZEUS Microvertex Detector*. Diploma Thesis, DESY, 1999.

[72] A. Quadt et al., Nucl. Inst. Meth. **A 438**, 472 (1999).

[73] GFLT home page, `http://giroz.desy.de/components/gflt/`.

[74] A. Quadt, *A Parallel Processing Track Trigger for the ZEUS High Energy Electron-Proton Scattering Detector*, 1997. MSc Thesis, Oxford.

[75] A. Quadt, *Running Modes of the CTD-SLT and their impact on a Global Tracking SLT* (unpublished). ZEUS-97-067.

[76] S. Sampson, *Charm Tagging at the SLT with a Microvertex Detector* (unpublished). ZEUS-97-077.

[77] M. Sutton. Private communications.

[78] G. F. Hartner, *VCTRAK Briefing: Program and Math* (unpublished). ZEUS-98-058.

[79] M. Sutton, *The Status of the Global Tracking Trigger.* Talk given to ZEUS collaboration week, DESY, June 26^{th} 2001.

[80] B. Andersson et al., Phys. Rep. **97**, 31 (1983).

[81] G. Ingelman, J. Rathsman and G.A. Schuler, Comp. Phys. Comm. **101**, 135 (1997).

[82] G. Ingelman, A. Edin and J. Rathsman, Comp. Phys. Comm. **101**, 108 (1997).

[83] H. Jung and G. P. Salam, Eur. Phys. J. **C 19** (2001).